Patterns of Electron Flux in the Near-Earth Plasma Sheet: Statistical Learning

by

Brian Michael Swiger

A dissertation submitted in partial fulfillment
of the requirements for the degree of
Doctor of Philosophy
(Climate and Space Sciences and Engineering)
in the University of Michigan
2022

Doctoral Committee:

Dr. Natalia Ganushkina, Co-chair
Professor Michael Liemohn, Co-chair
Assistant Professor Yang Chen
Professor Tuija Pulkkinen

Brian Michael Swiger
swigerbr@umich.edu
ORCID iD: 0000-0002-1495-1398

© Brian Michael Swiger 2022

DEDICATION

for AJS
better days are coming

ACKNOWLEDGMENTS

I would not have completed this dissertation without the guidance and mentorship of my advisors, Drs. Natalia Ganushkina and Michael Liemohn. They provided me a starting point in this field and showed me a research path. Although frustrating in the moment, I am thankful for the many times that they allowed me to veer into unrewarding research directions before guiding me back toward pertinent topics. Rather than telling me, they allowed me to learn through experience the true struggles and joys of conducting scientific research. I will be forever indebted to them for sharing their knowledge, experience, guidance, and insight toward my development as a researcher. Together, they directed me toward the finish.

I am also indebted to the two other members of my committee—Drs. Tuija Pulkkinen and Yang Chen—for their thoughtful, expert advice and assessment to improve my dissertation. I am honored that they agreed to serve on my committee.

The list of fellow students and peers who have helped me along this path is too long to name—yet their friendship will not be soon forgotten. I will remember most the three who were in my closest proximity (and whom are now Drs.). Abigail Azari was a mentor and friend in the beginning as I struggled through adjusting to the complexities of graduate school and the academic world. Alex Shane was a constant reminder that practicing science and pursuing a rich life do not have to be in conflict. Agnit Mukhopadhyay will be remembered for his support, encouragement, travel companionship, and understanding throughout our graduate careers. I think without these friends, I may have decided this pursuit was not worth the effort.

Throughout the previous five years, I was financially supported by several sources. The National Aeronautics and Space Administration provided funding through the Future Investigators in NASA Earth and Space Sciences and Technology grant # 80NSSC20K1504. I thank the Michigan Space Grant Consortium for receipt of a Graduate Student Fellowship. I am grateful to be a recipient of a Rackham Merit Fellowship. Along with financial support, the Fellowship provided a welcoming community of future University of Michigan scholars, and it positively contributed to my success as a graduate student at the university. A part of my graduate studies was funded with the Post

9/11 GI Bill, and I am fortunate that I was born into a society and nation that recognizes, honors, and continues to support those who sacrifice to serve it.

Most of the work for this dissertation would not be possible without the following science teams and institutions making their data public and readily available: THEMIS, NASA GSFC SPDF, WDC Kyoto, GFZ Potsdam, SuperMAG, LASP LISIRD. I also heavily relied on open source software for data analysis and numerical model development, and I am grateful for the time and effort that many thousands of people have donated toward making scientific computing more accessible.

I thank DLE for remaining a friend from a distance throughout.

I finally want to thank my family who have always provided me a safe place to rest from and to reflect upon my chosen path. They unconditionally supported my apparent aberration of effort even if they did not fully understand why I pursued it.

TABLE OF CONTENTS

DEDICATION ii

ACKNOWLEDGMENTS iii

LIST OF FIGURES viii

LIST OF TABLES x

LIST OF APPENDICES xi

ABSTRACT xii

CHAPTER

1 Introduction 1

1.1 Overview 1
1.2 Background 2
1.3 Motivation 4
1.3.1 The Solar Wind Drives the Plasma Sheet 5
1.3.2 The Esoteric (Scientific) Perspective 5
1.3.3 The Practical (Space Weather) Perspective 6
1.4 Focus Areas 7
1.4.1 Climatic Averages 7
1.4.2 Spacecraft Charging Environments 9
1.4.3 Electron Flux Changes During Substorms 9
1.4.4 Empirical Modeling 11

2 Data Description 14

2.1 Solar and Solar Wind Data 14
2.1.1 OMNI 14
2.1.2 FISM-2 17
2.2 Magnetospheric Spacecraft Data 19
2.2.1 Particle Fluxes and Distributions 19
2.2.2 LANL MPA & SOPA 20
2.2.3 THEMIS 20
2.3 Ground Magnetometer Data 24
2.3.1 *Kp* 25

2.3.2 SYM-H . . . 26
2.3.3 AE . . . 28
2.3.4 SME . . . 29

3 Average Climatic Electron Fluxes . . . 33

3.1 Introduction . . . 33
3.2 Data & Methods . . . 35
3.2.1 THEMIS Electron Flux Survey . . . 35
3.2.2 Relational Parameters—SW, IMF, & Geomagnetic Indices . . . 36
3.2.3 Sample Subsets . . . 37
3.3 Average Fluxes by Solar Wind and Geomagnetic Activity . . . 38
3.3.1 Solar Wind, IMF, and Geomagnetic Index Subsets . . . 39
3.3.2 Distance Subsets . . . 50
3.4 Discussion & Conclusion . . . 50
3.4.1 Sub-thermal (0.3 keV) Flux Responses . . . 57
3.4.2 Thermal (2 keV) Flux Responses . . . 57
3.4.3 Near-superthermal (12 keV) Flux Responses . . . 58
3.4.4 Superthermal (52 keV) Flux Responses . . . 58
3.4.5 Conclusion . . . 58
3.4.6 Future Steps . . . 59

4 Severe Environments for Spacecraft Surface Charging . . . 60

4.1 Introduction . . . 60
4.2 Severe Environment Events from LANL Data . . . 65
4.3 Worst-Case Severe Environments for Surface Charging and Current Geomagnetic Activity . . . 67
4.3.1 Dependence on Geomagnetic Indices . . . 67
4.3.2 Dependence on IMF and Solar Wind Parameters . . . 75
4.3.3 Risks for Severe Environments for Surface Charging Dependent on Criteria Definitions . . . 79
4.4 Worst-Case Severe Environments for Surface Charging with Superimposed Epoch Analysis . . . 83
4.4.1 Geomagnetic Indices . . . 83
4.4.2 IMF and Solar Wind Parameters . . . 85
4.4.3 Time History for Severe Environments for Surface Charging Dependent on Criteria Definitions . . . 89
4.5 Discussion and Conclusions . . . 91

5 Electron Flux Changes During Substorms . . . 95

5.1 Introduction . . . 95
5.2 Methodology . . . 96
5.2.1 Data . . . 96
5.2.2 Calculating Flux Changes . . . 97
5.3 Results . . . 99
5.3.1 Bootstrap analysis . . . 103

5.3.2 Heatmaps . . . 104
5.4 Discussion . . . 109
5.5 Conclusion . . . 112

6 Empirical Modeling . . . 114

6.1 Towards a full neural network model . . . 114
6.1.1 Introduction . . . 114
6.1.2 Methods . . . 116
6.1.3 Results . . . 121
6.1.4 Discussion . . . 124
6.1.5 Conclusion . . . 126
6.2 Solar Wind — Plasma Sheet Neural Network . . . 126
6.2.1 Introduction . . . 126
6.2.2 Model Development . . . 129
6.2.3 Model Assessment . . . 138
6.2.4 Discussion . . . 152
6.2.5 Conclusions . . . 155

7 Conclusions . . . 157

7.1 Progress on Specific Focus Areas . . . 157
7.1.1 Climatic Averages . . . 157
7.1.2 Spacecraft Charging Environments . . . 158
7.1.3 Electron Flux during Substorms . . . 158
7.1.4 Empirical Modeling . . . 159
7.2 Implications . . . 160
7.3 Future Directions . . . 161
7.3.1 Climatic Averages . . . 161
7.3.2 Spacecraft Charging Environments . . . 162
7.3.3 Electron Flux during Substorms . . . 162
7.3.4 Empirical Modeling . . . 163

APPENDICES . . . 166

BIBLIOGRAPHY . . . 176

LIST OF FIGURES

FIGURE

1.1 Representation of Earth's magnetosphere externally driven by solar wind 3
1.2 Tippy pitcher model of a substorm 5
1.3 Monthly solar sunspot and F10.7 values 8
1.4 Superposed epoch of electron flux increase during substorm injections 10
1.5 Modeled electron temperature and density in the plasma sheet 12
1.6 Modeled >38 keV electrons in the central plasma sheet 13

2.1 Typical ACE and WIND orbits around L1. 15
2.2 Example OMNI data 16
2.3 Distances of the ACE and WIND spacecraft from the Sun-Earth line. 17
2.4 ACE and WIND observing different solar wind structure. 18
2.5 FISM-2 20 eV and 60 eV photon flux for solar cycle 24 19
2.6 Example of THEMIS orbits 21
2.7 THEMIS string of pearls orbit configuration 22
2.8 Example THEMIS ESA, SST, FGM data 23
2.9 THEMIS spacecraft instrument layout 24
2.10 *Kp* station locations and example data 27
2.11 SYM-H index example data 29
2.12 Example of AE indices for one day 30
2.13 SuperMAG ground station locations 31
2.14 Example of SME indices for one day 32

3.1 12 keV electron flux heatmap for V_{SW}=[500, 600) $\mathrm{km \cdot s^{-1}}$ 39
3.2 Sampling heatmap for V_{SW}=[500, 600) $\mathrm{km \cdot s^{-1}}$ 40
3.3 Solar wind–driven median levels of 0.3 keV electron flux in the GSM XY-plane 42
3.4 Solar wind–driven median levels of 2 keV electron flux in the GSM XY-plane 43
3.5 Solar wind–driven median levels of 12 keV electron flux in the GSM XY-plane 44
3.6 Solar wind–driven median levels of 52 keV electron flux in the GSM XY-plane 45
3.7 Geomag. activity and median level of 0.3 keV eflux in the GSM XY-plane 46
3.8 Geomag. activity and median level of 2 keV eflux in the GSM XY-plane 47
3.9 Geomag. activity and median level of 12 keV eflux in the GSM XY-plane 48
3.10 Geomag. activity and median level of 52 keV eflux in the GSM XY-plane 49
3.11 12 keV electron flux at 6.6–7.0 $\mathrm{R_E}$ by V_{SW} 51
3.12 Sampling heatmap for 6.6–7.0 $\mathrm{R_E}$ by V_{SW} 52
3.13 Median 0.3 keV electron flux at 7, 9, and 11$\mathrm{R_E}$ 53
3.14 Median 2 keV electron flux at 7, 9, and 11$\mathrm{R_E}$ 54

3.15 Median 12 keV electron flux at 7, 9, and 11 R_E . . . 55
3.16 Median 52 keV electron flux at 7, 9, and 11 R_E . . . 56

4.1 Severe charging environments and geomagnetic indices . . . 71
4.2 Severe charging environments and solar wind drivers . . . 76
4.3 Superposed epoch for charging env. and geomag. indices . . . 86
4.4 Superposed epoch for charging env. and solar wind driving . . . 87

5.1 Example of electron flux increase post substorm onset . . . 98
5.2 Example of electron flux stagnation post substorm onset . . . 98
5.3 Pair-plot of 2 keV electron flux changes, MLT, Rdist, dMLT, & SME . . . 100
5.4 Pair-plot of 12 keV electron flux changes, MLT, Rdist, dMLT, & SME . . . 101
5.5 Pair-plot of 52 keV electron flux changes, MLT, Rdist, dMLT, & SME . . . 102
5.7 Bootstrapped linear corr. of substorm eflux changes . . . 105
5.8 Bootstrapped linear corr. of substorm eflux changes—low radial dist. . . . 106
5.9 Bootstrapped linear corr. of substorm eflux changes—medium radial dist. . . . 107
5.10 Bootstrapped linear corr. of substorm eflux changes—high radial dist. . . . 108
5.6 Electron flux change heatmap by radial distance . . . 109
5.11 Electron flux change heatmap by max SME . . . 110

6.1 Train and test loss/skill for early NN versions . . . 121
6.3 Spatial sampling frequencies for empirical model development . . . 132
6.4 Observed versus modeled electron flux for select energies . . . 139
6.5 Observed and modeled electron energy flux spectrograms for April 2010 . . . 142
6.6 Ratio of observed to modeled electron energy flux for April 2010 . . . 143
6.7 Spatial regions considered for model assessment . . . 146
6.8 Model-model comparison between Dubyagin2016 and SWPSNN . . . 148
6.9 Feature ranking of model inputs . . . 151
6.10 Feature inter-correlations and auto-correlations . . . 152

B.1 Calculation of $B_{Z,\mathrm{ULF}}$ . . . 168

C.1 Model-Observation scatterplots for energies 0.08–1.7 keV . . . 170
C.2 Model-Observation scatterplots for energies 2.2–31 keV . . . 171
C.3 Model-Observation scatterplots for energies 41–93 keV . . . 172

LIST OF TABLES

TABLE

3.1 List of energy channels in our THEMIS survey dataset 36
3.2 SW, IMF, & Geomagnetic Index parameter bins 38

4.1 15 min avgs. of LANL observations between 20–08 MLT 68
4.2 Peaks in number of severe surf. charg. env. events 80
4.3 Highest risks to detect severe charg. env. 80
4.4 Timing of severe surf. charg. env. changes 89

6.1 Metrics for early NN versions 123
6.2 Optimized hyperparameter values 138
6.3 Metrics for full neural network assessment 140
6.4 Observed-modeled metrics for April 2010 145
6.5 Metrics for subregions 146
6.6 Metrics for Dubyagin2016 and SWPSNN comparison 148

A.1 Model-observation metric definitions 166

C.1 Additional test metrics for SWPSNN model 173
C.2 Additional metrics for SWPSNN model for period April 2010 174
C.3 Additional metrics for Dubyagin2016 model for period April 2010 175

LIST OF APPENDICES

A Metric Definitions **166**

B Calculation of IMF Wave Power **167**

C Supporting Information for Empirical Modeling **169**

ABSTRACT

The focus of this dissertation is on improving the understanding and prediction capability of thermal (1–10 keV) to superthermal (10–100 keV) electron flux in the near-Earth (6–12 R_E, 18–00–06 MLT; $R_E \approx 6370\,\mathrm{km}$, MLT = magnetic local time) plasma sheet and especially its dependence on solar wind driving.

The solar wind and interplanetary magnetic field flow past and interact with Earth's magnetic field, forming a magnetic cavity called the magnetosphere. In Earth's nightside magnetosphere, the dynamics of electrons within the near-Earth magnetotail are highly dependent on variations in the solar wind and overall solar activity. The electrons are the source population for the Earth's outer radiation belts, contribute to storm-time ring current pressure and energy, and precipitate into the ionosphere forming part of the aurora. Additionally, this population of electrons are most responsible for the spacecraft surface charging environment at geosynchronous (GEO) orbit. Some dependencies of superthermal electrons on solar wind variations have been identified through several previous investigations; however, there is much that is not known, and it has been difficult to predict their behavior.

Utilizing more than twelve years of data from THEMIS spacecraft, we have investigated the long-term and short-term dependencies of electron flux in the near-Earth plasma sheet to solar wind variations. On time scales of a solar sunspot cycle, we explore the response of energetic electron flux in the near-Earth plasma sheet to solar wind and geomagnetic activity. We show that with only slight solar wind driving (solar wind flow speed, V_{SW} = 400–500 $\mathrm{km \cdot s^{-1}}$) and weak geomagnetic activity (Auroral Electrojet index, AE = 100–300 nT), there is a substantial increase in median 12–52 keV electron flux. We also explored the role that solar wind driving has on short-term (1–2 hours) electron flux variations and found that V_{SW} is the most significant contributor to severe spacecraft surface charging environments at GEO. Furthermore, simply the presence of elevated geomagnetic activity (as indicated by the AE index) is a sufficient indicator of risk for an extreme charging environment. In examining 101 observations of the change of electron flux in the near-Earth plasma sheet during substorms, we failed to find a dependence of flux changes on substorm strength, nor spacecraft location, nor location relative to the peak of auroral activity.

Finally, we develop an empirical, machine-learned neural network model of electron flux in the near-Earth plasma sheet, dependent on inputs of solar wind parameters and their time history.

Our model overcomes limitations of previous models by including only inputs that are external to the magnetosphere and predicting differential flux at a wide range of energies. We calculate several model–observation metrics—our model predicts electron flux with a Pearson correlation coefficient between 0.55–0.77 and has a median symmetric accuracy of between 41–140% (metric ranges depend on energy); and, we rank which solar wind parameters are most relevant to predictions. We show that including short time (5-minute) resolution inputs to the model does not result in predicting small scale (1-hour) variations of plasma sheet electron flux. Overall, this dissertation advances knowledge of the dependence of superthermal electron flux in the near-Earth plasma sheet to solar wind variations.

CHAPTER 1

Introduction

Modern society daily relies on hundreds of satellites at the geosynchronous (GEO) and medium orbit (MEO) altitudes for communication, navigation, weather forecasting, entertainment, and national defenses. Meanwhile, satellites in the MEO and GEO orbits are routinely exposed to severe spacecraft charging environments that can temporarily or permanently render them inoperable. One of the main contributions to severe spacecraft charging environments is energetic electron flux in the near-Earth plasma sheet, and the focus of this dissertation is on improving the understanding and prediction capability of this flux and how it is being driven by the solar wind.

1.1 Overview

In Section 1.2, we provide the reader with the terminology and background information that is relevant to solar wind driving of electron flux in the plasma sheet. In Section 1.3, we describe motivation for further research in this area, and in Section 1.4, we highlight specific areas where we focused our efforts. Each focus area is expanded into a chapter. A brief description of the data that we used in these focus areas can be found in Chapter 2. Chapter 3 describes the climatological levels of electron flux in the near-Earth plasma sheet and their dependence on solar wind and geomagnetic conditions. In Chapter 4, we examine the role that solar wind and geomagnetic conditions have in producing extreme spacecraft charging environments at GEO. Chapter 5 seeks, yet fails, to find a relationship between the strength of a substorm and the level of electron flux enhancement in the near-Earth plasma sheet. In Chapter 6, we develop a new empirical model with a machine-learned, neural network that predicts electron flux in the near-Earth plasma sheet using inputs of solar wind driving. Finally, Chapter 7 recapitulates the main findings in each of the four focus areas (Chapters 3–6), and it explores future directions of research in each area.

1.2 Background

When the solar wind—a supersonic flow of charged particles escaping from the Sun (Snyder et al., 1963; Parker, 1965)—travels into interplanetary space, it carries with it the interplanetary magnetic field (IMF) (Parker, 1958; McCracken, 1962; Dessler, 1967). Together, the solar wind and IMF distort the Earth's intrinsic magnetic field away from a dipolar shape (e.g., Martyn, 1951; Ferraro, 1960; Spreiter & Hyett, 1963; Coroniti & Kennel, 1972; Sibeck et al., 1991), forming a magnetic cavity called the magnetosphere (e.g., Roederer, 1974) (see Figure 1.1). The shape of the magnetopause—the magnetospheric boundary between the Earth's magnetic field and the IMF—follows a surface of force balance between the flow pressure of the solar wind and the pressure of Earth's magnetic field. At the subsolar point, the solar wind flow pressure compresses Earth's magnetic field to a nominal 10 R_E (1 $R_E \approx 6370$ km); but, in the anti-sunward direction, the field is greatly stretched to hundreds of R_E, forming a magnetotail (e.g., Ness et al., 1964; Axford et al., 1965).

Within Earth's magnetotail, the magnetic field in the North is directed earthward, and the magnetic field in the South is directed anti-earthward. The oppositely directed magnetic field must, according to Ampère's Law, be separated by a sheet of electrical current. This electrical current sheet contains relatively weak magnetic field and high density plasma which is commonly known as the plasma sheet (see Figure 1.1). Separating the magnetotail into northern and southern lobes, the plasma sheet extends from the edge of the dominance of Earth's magnetic dipole field at approximately 6 R_E to hundreds of R_E downtail, and its azimuthal extent ranges several hours of magnetic local time (MLT) (Hill, 1974).

Much of the focus of this dissertation is on the electron population within the near-Earth (6–12 R_E, 06–18 MLT) plasma sheet. The average electron thermal energy ranges from 0.1–10 keV (e.g., C.-P. Wang et al., 2017), depending on upstream solar wind conditions. The behavior of electrons above this average energy range—the so-called superthermal population—is consequential to inner magnetosphere dynamics and space weather hazards to spacecraft. We further describe some of these consequences and demonstrate motivation for further study in Section 1.3.

Far from being a static structure, the Earth's magnetotail is constantly undergoing changes (e.g., Sharma et al., 2008). One such global, large scale disturbance of the magnetosphere is called a geomagnetic storm. A comprehensive description of a geomagnetic storm is provided by Gonzalez et al. (1994). We recount a few details here. When large scale, fast moving structures within the solar wind (e.g., a coronal mass ejection) impact Earth's magnetopause, large amounts of solar wind energy and particles cause large disturbances in near-Earth space, typically lasting several days. Superthermal electron flux in the near-Earth plasma sheet is the most variable during geomagnetic storm periods. There is a large build-up of 10s of keV energy particles in the inner

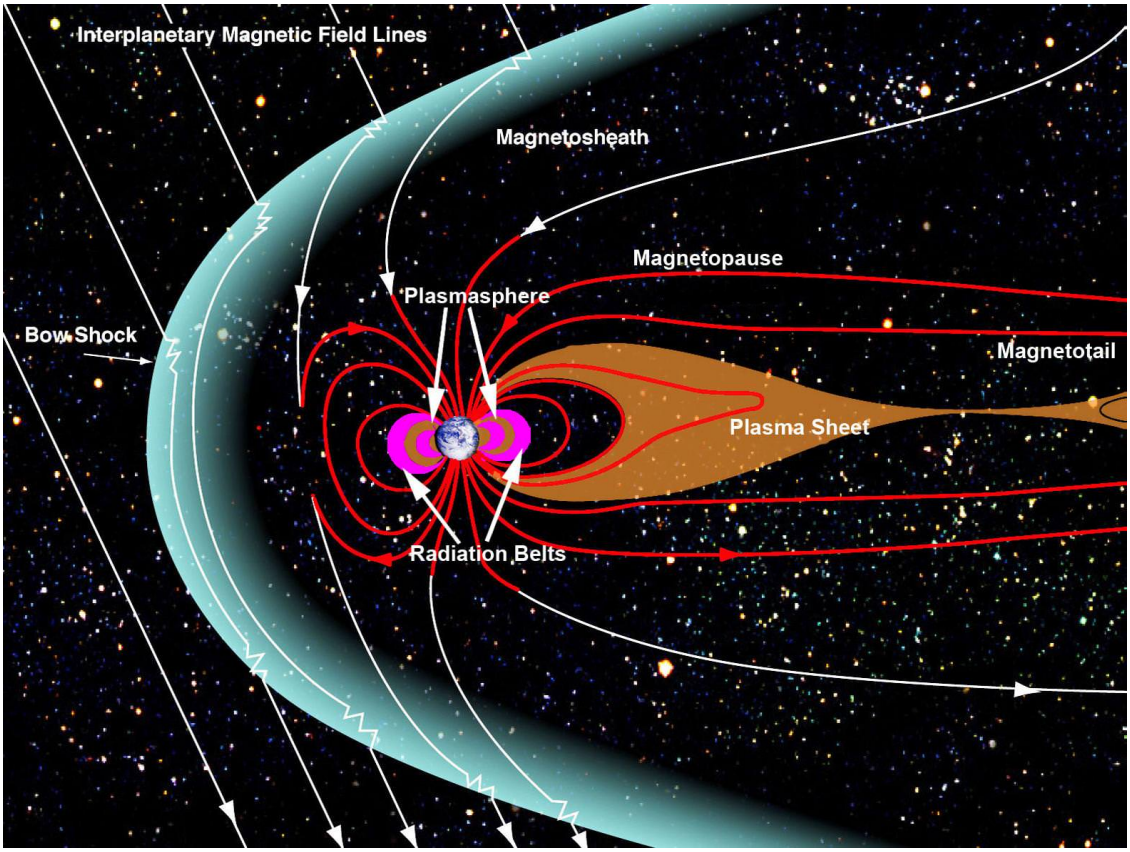

Figure 1.1: Illustrative representation of Earth and the major components of the surrounding near-Earth space environment. The view is of the North-South plane with the Sun to the left. Lines represent the magnetic field direction and strength, with lines closer together indicating stronger magnetic field. The white lines represent IMF and red lines represent magnetic field contained within the magnetopause (i.e., closed field). [Image credit: NASA]

magnetosphere, forming a ring current of plasma around the Earth. The ring current is one of the main sources of the typical signature of a geomagnetic storm in ground magnetometer observations (see e.g., Figure 2.11). The occurrence frequency of geomagnetic storms varies with the solar sunspot cycle (see Section 1.4.1 and Figure 1.3 for a brief explanation of the solar sunspot cycle). In the peak and declining years of the sunspot cycle (solar maximum and declining phase) there can be several geomagnetic storms per month; whereas, in the sunspot cycle trough years (solar minimum) there are only a few storms per year (I. G. Richardson & Cane, 2012).

Another global, recurrent change—relevant to the investigations of Chapters 4 and 5—is called a magnetospheric substorm. The substorm is a complex, nonlinear process that redistributes energy within Earth's magnetosphere from the magnetotail to the inner magnetosphere. Since the first descriptions of a substorm by Akasofu (1964), there have been thousands of subsequent studies seeking to understand the substorm process. We do not intend to recapitulate the entire history

of the study of magnetospheric substorms, but rather provide a high-level overview of the substorm processes that are relevant to our investigations. The interested reader may seek further information about substorms from comprehensive review papers (e.g., Akasofu, 1968; Rostoker, 1972b; Elphinstone et al., 1996; Kepko et al., 2014).

The canonical substorm process has a duration of approximately two hours and consists of three phases, with each phase lasting around one-half to one hour. In the growth phase, a substorm begins to develop when energy from the solar wind is stored in the magnetotail lobes, above and below the plasma sheet. The plasma sheet itself becomes thinner as the lobes increase in pressure, forcing oppositely directed magnetic field closer together. The magnetotail has a finite limit of energy that it can store, and the more energy that is stored in the tail, the more unstable it becomes. Eventually, the instability in the form of magnetic reconnection between the northern and southern magnetic lobes occurs around the beginning of the expansion phase of a substorm. The subsequent and sudden release of the energy in the magnetotail deposits into the ionosphere and GEO and MEO altitudes (e.g. Rostoker et al., 1988). In the expansion phase, the plasma sheet also suddenly expands as the magnetic field becomes more dipolar at near-Earth distances, transporting and accelerating superthermal electrons earthward. Akasofu (2019) analogizes the storing and sudden release of energy in the magnetotail as the combination of a "bucket" and "tippy pitcher" (see Figure 1.2). In the analogy, the "bucket" represents the solar wind–driven magnetosphere, which results in energy release as a result of sudden changes in the solar wind and IMF. Meanwhile, the "pitcher" accounts for instability during the loading–unloading of energy within the magnetotail. Subsequent to the expansion phase, the magnetosphere undergoes a recovery phase, where the plasma sheet returns to pre-growth phase conditions. The frequency of substorms depends largely on solar wind driving conditions. Borovsky and Yakymenko (2017) identified three conditions for substorm occurrence. Periodically driven substorms recur approximately every 2–4 hours. Random, isolated substorms have a recurrence rate of 6–15 hours. When solar wind conditions are quiet, there can be longer periods (greater than 24 hours) during which no substorms occur.

1.3 Motivation

Delving deeper into the processes of near-Earth plasma sheet electrons, we introduce motivating factors for pursuing the study of superthermal electrons and their dependence on solar wind driving. There are compelling reasons for further exploration of the the behavior of plasma sheet electrons dependent on solar wind variations. Additionally, understanding more about this population has practical implications for space weather modeling and forecasting.

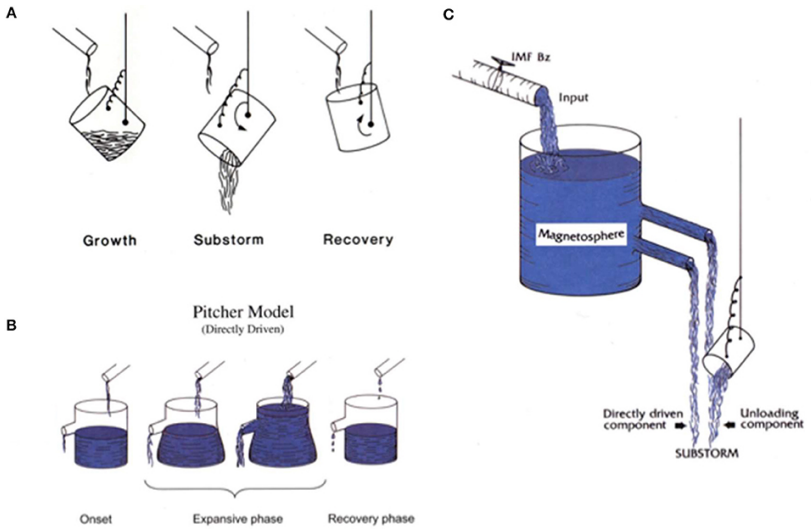

Figure 1.2: Figure 5 of Akasofu (2019). "(A) a tippy pitcher model of substorms. (B) a bucket model of substorms. (C) after much discussions among researchers, it was agreed that the magnetosphere has both components."

1.3.1 The Solar Wind Drives the Plasma Sheet

It is known that variations in the near-Earth plasma sheet are dependent on solar wind conditions upstream of Earth's bow shock. For example, during periods of several (≈9) hours of northward IMF, the plasma sheet number density increases and the temperature of the particles decreases (Terasawa et al., 1997). More directly, Borovsky et al. (1998) found that the plasma sheet number density is strongly correlated with the solar wind number density, N_{SW}, and that the plasma sheet temperature is strongly correlated with the solar wind flow speed, V_{SW}. Nagata et al. (2008) examined the plasma sheet number density during various combinations of slow/fast V_{SW} and North/South IMF. Among their findings, they determined that southward IMF during fast V_{SW} had a stronger influence than N_{SW} on the plasma sheet number density. Examining electron flux in the plasma sheet directly, Burin des Roziers, Li, Baker, Fritz, Friedel, et al. (2009) found strong correlation between superthermal electron flux in the plasma sheet with V_{SW} and found that the flux is enhanced during southward IMF. Part of this dissertation seeks to add insight to our understanding of the role that the solar wind has on driving the variations of electron flux in the plasma sheet.

1.3.2 The Esoteric (Scientific) Perspective

Superthermal plasma sheet electrons act as a link in one of the chains of transfer of energy and particles from the solar wind to the inner magnetosphere and ionosphere. From the solar wind, energetic particles are transported through the magnetotail lobes and into the tail plasma sheet and

ultimately to the near-Earth plasma sheet through $\mathbf{E} \times \mathbf{B}$ drift (e.g. Wing et al., 2014). The near-Earth plasma sheet, which contains the transition region from stretched to dipolar magnetic field, is an important driver of inner magnetosphere dynamics (e.g., Schield et al., 1969; Southwood & Wolf, 1978; Wolf et al., 2007; Ganushkina et al., 2015; Artemyev et al., 2018). The superthermal electrons originating within the plasma sheet have particular effectiveness at altering the inner magnetosphere (e.g., Garrett, 1979; Turner & Li, 2008; Yu et al., 2019). During substorms, superthermal electrons from the magnetotail plasma sheet are accelerated and transported to inside the region dominated by the Earth's magnetic dipole (e.g. Lezniak et al., 1968; Lezniak & Winckler, 1970; Williams et al., 1990). The injected electrons can be further energized and scattered through wave-particle interactions. Wave-particle interactions scatter electrons into the loss cone (e.g., Swift, 1981; Davidson, 1986; Inan et al., 1992) from which they precipitate into the ionosphere, making the plasma sheet the source of the diffuse aurora (e.g., A. T. Y. Lui et al., 1977; Meng et al., 1979; Ni et al., 2016). Chorus waves, which occur as a part of the scattering process (Kennel & Petschek, 1966; Kennel & Thorne, 1967; Li et al., 2008, 2012) are frequently generated during injections of a few keV to 10s of keV electrons from the plasma sheet into the inner magnetosphere (e.g., Tsurutani & Smith, 1974; Meredith et al., 2002). As a bonus to the scattering, the whistler mode chorus waves are one of the mechanisms that energize the seed population of electrons to relativistic energies in the outer radiation belt (e.g., Horne et al., 2005; Chen et al., 2007; Jaynes et al., 2015). Moreover, electrons with energy of 1–50 keV can contribute significant energy (estimates of 10–30%) to the ring current during geomagnetic storms (e.g., Liu, 2005; Zhao et al., 2016), and electrons contribute up to 18% of the total ring current pressure during storms (Kumar et al., 2021). The dependence of inner magnetosphere dynamics to superthermal plasma sheet electrons, which are driven by solar wind variations (i.e. Section 1.3.1), makes studying the dependence of these electrons to solar wind drivers a compelling endeavor. Furthering our understanding of the dependence of plasma sheet electrons to solar wind driving marks a substantial increase in also further understanding the transfer of energy and particles within the inner magnetosphere.

1.3.3 The Practical (Space Weather) Perspective

From a space weather perspective, superthermal electrons in the near-Earth plasma sheet are an important consideration. They impact the hazardous environment for satellites by directly contributing to spacecraft surface charging environments (e.g., Garrett, 1981; H. C. Koons et al., 1999; V. A. Davis et al., 2008), posing a space weather hazard to satellites at GEO (e.g., Choi et al., 2011; Thomsen et al., 2013; Matéo-Vélez et al., 2018; Ganushkina et al., 2021). Spacecraft inside of GEO are not exempt from the hazard, as the superthermal electrons can penetrate inside GEO to MEO (Turner et al., 2015; Motoba et al., 2021). Surface charging effects satel-

lites through the rapid build-up and discharge of charged particles that occur most frequently with exposure to larger than normal fluxes of superthermal electrons. If the charge accumulates on separate satellite surfaces, a differential charge exists. The subsequent discharge may pass through sensitive spacecraft electronics or otherwise arc to sensitive surface components, like solar cells. Over time, degradation of the spacecraft surfaces can significantly shorten the expected satellite service life. Moreover, superthermal electrons are the source population for the relativistic radiation belt electrons (e.g., Jaynes et al., 2015), which can directly penetrate spacecraft shielding and cause anomalies (e.g., W. Lohmeyer et al., 2015). More accurate specifications of the levels of electron flux, based on geomagnetic conditions and solar wind driving parameters, in the spacecraft charging environment would lead to better mission planning and more stable spacecraft operations (Green et al., 2017). Additionally, with improved models of predictions of electron flux in the plasma sheet from solar wind driving, we would be able to provide more accurate boundary conditions for physics–based inner magnetosphere models of the radiation belt electrons.

1.4 Focus Areas

There are unresolved questions regarding the behavior of superthermal electrons in the near-Earth plasma sheet and their dependence on solar wind driving. We organize some of these questions into focus areas, and introduce them in the remaining sections of this chapter. Elucidating understanding in each of these areas has collective importance toward more fully resolving the behavior of the superthermal electron population in the near-Earth plasma sheet. Moreover, a more thorough understanding of this population's behavior in response to upstream solar wind driving conditions will lead to improved space weather forecasts of the near-Earth spacecraft radiation environment.

1.4.1 Climatic Averages

Fluxes of energetic electrons in the plasma sheet are known to correlate with geomagnetic activity (e.g., Anderson, 1965) and solar wind and IMF variations (Burin des Roziers, Li, Baker, Fritz, Friedel, et al., 2009). We seek further understanding of the climatological average distribution of superthermal electrons in the near-Earth plasma sheet during various solar wind driving and geomagnetic activity conditions. There have been a few, limited studies of the dependence of average electron fluxes in the plasma sheet to solar wind variations (e.g., Burin des Roziers, Li, Baker, Fritz, Friedel, et al., 2009; Luo et al., 2011) and to geomagnetic activity (e.g., Vasyliunas, 1968; Christon et al., 1991; Åsnes, A. et al., 2008).

However, on time scales on the order of a solar sunspot cycle, the climatic, average response of electron flux to different levels of solar driving and correlation with geomagnetic activity has

yet to be explored. The relevance of the sunspot cycle to a magnetospheric climatic survey is that a full cycle encompasses a range of solar activity from low to high. In Figure 1.3 we show the progression of the monthly sunspot numbers (black diamonds, lower panel) observed on the surface of the Sun and their smoothed monthly average (purple line) for years 2008–2020. The upper panel of Figure 1.3 shows the monthly flux of 10.7 cm wavelength photons (F10.7, generally regarded as an indicator of overall solar activity) and the smoothed monthly average during the same period. As the number of sunspots change over time, overall solar activity—including solar wind and IMF—changes (e.g., Hundhausen, 1979). Consequently, the magnetosphere responds to the solar wind and IMF changes and has different average conditions during different phases of the sunspot cycle. For example, historically there has been elevated levels of geomagnetic activity in response to above average solar wind flow speeds during the declining phase (2–3 years subsequent of the sunspot number maximum year) of a sunspot cycle (e.g., Sheeley et al., 1977).

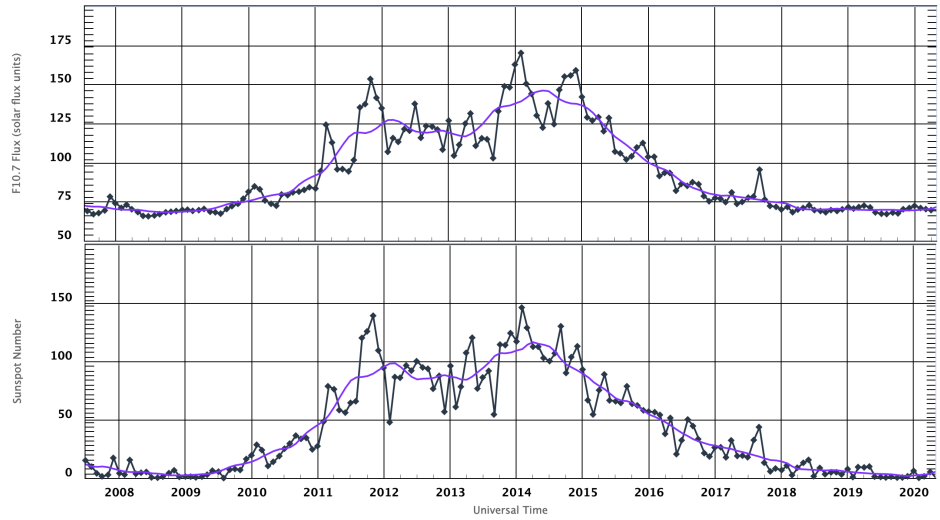

Figure 1.3: Top panel: Monthly solar F10.7 index values (black diamonds) and their smoothed values (purple curve). Bottom panel: Monthly sunspot numbers (black diamonds) and their smoothed values (purple curve). Figure modified from the Space Weather Prediction Center Solar Cycle Progression webpage: https://www.swpc.noaa.gov/products/solar-cycle-progression.

To account for the changes during all phases of the solar sunspot cycle, we use data from years 2008–2020. We perform a climatological survey of the electron flux in the near-Earth plasma sheet and its dependence on solar wind driving. The results, which are shown in Chapter 3, inform our understanding and focus of further investigation of the plasma sheet superthermal electrons.

1.4.2 Spacecraft Charging Environments

Operational anomalies due to the charging of spacecraft remains one of the worst hazards of the space radiation environment (e.g., Lam et al., 2012; Loto'aniu et al., 2015; Bodeau, 2015; Green et al., 2017), with spacecraft *surface* charging causing the most severe anomalies (e.g., Choi et al., 2011; Matéo-Vélez et al., 2018). The dangers of surface charging to operational spacecraft stem from the increased risk of a discharge or arc through or to an electrically susceptible part of the spacecraft (i.e., internal electronics or external solar panels).

It has long been observed that surface charging at GEO occurs more frequently during magnetospheric substorm activity (e.g., DeForest, 1972; Fredricks & Scarf, 1973; Rosen, 1976b, 1976a). Extensive correlation studies between surface charging anomalies and the *Kp* (Planetary K, see Section 2.3.1) index have found that most anomalies occur during low to medium geomagnetic activity ($Kp \leq 5$) (e.g., Spence et al., 1993; O'Brien, 2009). However, detailed investigations of severe spacecraft surface charging environments and their dependence on other geomagnetic indices, such as AE or SYM-H (indices described in Section 2.3), have not been performed. Furthermore, the driving of these environments by solar wind and IMF parameters has also not been well-investigated. Matéo-Vélez et al. (2018) identified 400 worst–case charging environments based on LANL spacecraft data (see Section 2.2.2 for LANL data description) and performed a limited analysis of their correlation with geomagnetic indices.

The main focus of Chapter 4 is finding relations between the solar wind / geomagnetic index parameters and worst–case severe environments for surface charging using the database of severe charging environments identified by Matéo-Vélez et al. (2018). Knowing the driving conditions and geomagnetic activity conditions that lead to surface charging environments is important in order to help provide meaningful risk assessments for spacecraft operations.

1.4.3 Electron Flux Changes During Substorms

There are many observational signatures used to determine the timing, duration, strength, and location of a substorm. These signatures include ground magnetometer perturbations (e.g., McPherron et al., 1973; Clauer & McPherron, 1974a, 1974b) and enhancements in satellite particle data at GEO (e.g. Mauk & Meng, 1983; Birn et al., 1997; Thomsen et al., 2001). In the plasma sheet, there are typical changes as well. For example, it has long been observed that during a substorm, the entire plasma sheet thins (in the north-south direction) as energy is accumulating in the magnetic field of the magnetotail. After the energy is released, the plasma sheet subsequently expands (e.g., E. W. Hones, 1980; Hill & Reiff, 1980; E. W. Hones et al., 1984; Baumjohann et al., 1992; Petrukovich et al., 2007; Artemyev et al., 2016). Post-expansion, it is often the case that the flux of electrons with energy of $\sim$10–50 keV have increased by an order of magnitude or more (e.g.,

Birn et al., 1997) (see Figure 1.4).

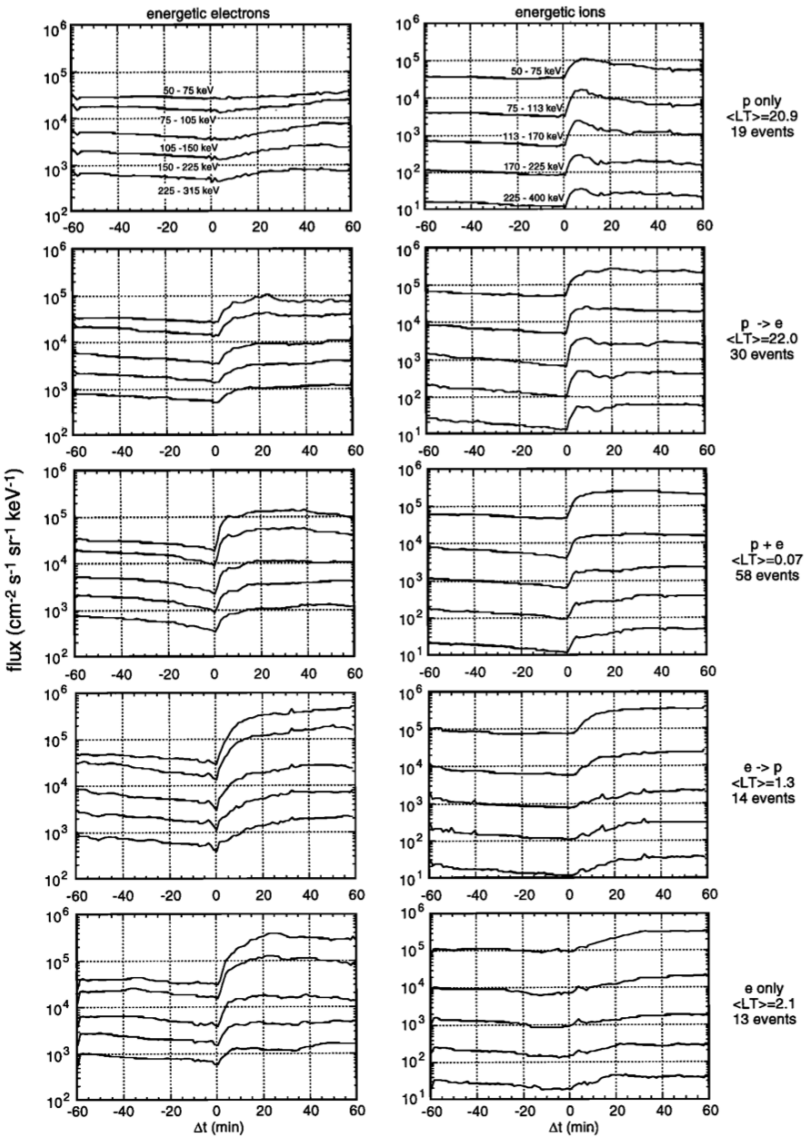

Figure 1.4: Figure 3 of (Birn et al., 1997). Superposed epoch of electron (left column of panels) flux changes during substorms observed at GEO. The labels to the right of each row are: "p only", pure ion injections without strong electron injections; "p→e", ion injection followed by electron injection with 2-min delay or more; "p+e", simultaneous ion and electron injections; "e→p", electron injections followed by ion injections with delay of 2-min or more; "e only", pure electron injections.

In Chapter 5, we better characterize the energization of superthermal plasma sheet electrons during substorms. The energization of superthermal electrons has been attributed to betatron and Fermi acceleration during the substorm dipolarization of the magnetic field in the near-Earth plasma sheet (e.g., Asano et al., 2010; Fu et al., 2011; Birn et al., 2013, 2014; Gabrielse et al.,

2016). The dipolarization itself is one consequence of a magnetospheric substorm and is characterized by the sudden increase in the northward component of magnetic field in the near-Earth magnetotail—the magnetic field rapidly becomes more "dipolar" (e.g., Baumjohann et al., 1999; Runov et al., 2009). The size of the dipolarization is related to the strength of the substorm current wedge (e.g., Hesse & Birn, 1991) that connects to the auroral ionosphere (e.g., Baumjohann, 2002; Kepko et al., 2014). As the SME index primarily responds to the auroral electrojet current (i.e., see Section 2.3.4), it can be considered as a proxy for the strength of a substorm, and by extension, the strength of the dipolarization and magnitude of electron energization. However, the magnitudes of electron flux increase during substorm dipolarizations are sometimes very strong or other times nonexistent (e.g., Runov et al., 2011), and sometimes there is a decrease in flux (e.g., Hwang et al., 2011). To investigate these discrepancies, we systematically look for correlations of the magnitude of electron flux increase with the strength of a substorm, as indicated by the SME index. We consider both the radial distance and local time of plasma sheet observations, as well as the azimuthal distance from the location of peak auroral electrojet current.

1.4.4 Empirical Modeling

Dozens of models exist for representing the many aspects of the space environment within near-Earth space (e.g., Tsagouri et al., 2013; Morley, 2020). There are global models and modeling frameworks that can encompass a completely modeled Sun-Earth space environment system. Yet, from the surface of the Sun to Earth's ionosphere and everything in between, the space environment varies considerably, and the global models lack sufficient capability in many areas. Therefore, many researchers and groups have created models tailored to a particular aspect or region of the space environment, for particular use cases and for advancing understanding of various phenomena. The near-Earth plasma sheet is one area of the space environment where specific models have been developed. Improving the specification and prediction of plasma sheet superthermal electron flux is important for both furthering our understanding and forecasting capability of the radiation environment in the inner magnetosphere and it's dependence on solar wind driving (i.e., see Section 1.3).

There are several existing, empirical models of electrons in the plasma sheet. However, not all models directly predict electron flux, such as those described by C.-P. Wang et al. (2013) and Yue et al. (2015), which both predict electron pressure. The Dubyagin et al. (2016) model uses V_{SW}, N_{SW}, and IMF to predict electron temperature and density in the plasma sheet. In Figure 1.5, we show modeled plasma sheet electron density and temperature from the Dubyagin et al. (2016) model during different solar wind conditions. When converting the predicted moments to fluxes, however, Dubyagin et al. (2019) found discrepancies of several orders of magnitude between the

predicted and observed superthermal electrons. They ultimately recommended that future models be built to predict electron fluxes directly.

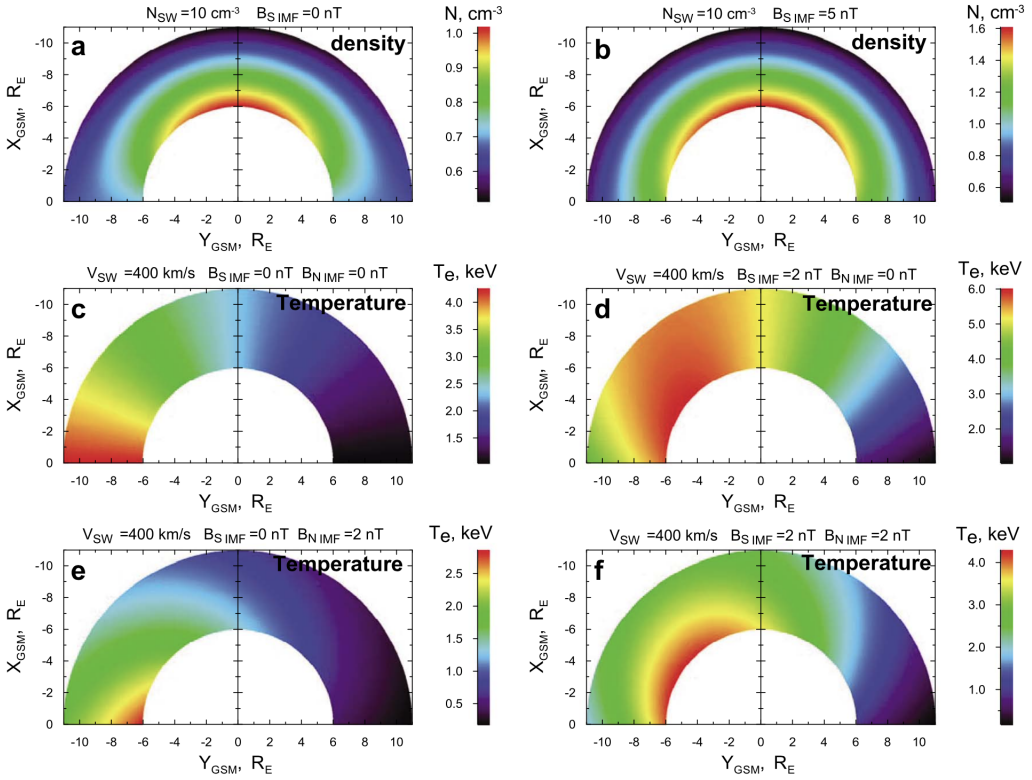

Figure 1.5: Figure 10 of Dubyagin et al. (2016). Each panel is for a different solar wind and IMF condition (labeled at the top of each panel). Panels a, b show the modeled electron density. Panels c-f show the modeled electron temperature.

Of the models that do predict electron fluxes directly, each has limitations. Luo et al. (2011) predicts electron flux from V_{SW}, N_{SW}, and IMF, but only for integrated electron flux at $>$38 keV. We include in Figure 1.6 modeled electron flux from Luo et al. (2011) in the plasma sheet for various solar wind and IMF conditions. A study by Stepanov et al. (2021) predicts electron flux in the plasma sheet using solar wind inputs, but only at three energies—10, 31, and 93 keV—and in a coarse grid of only nine regions (three azimuthal and three radial). Zou et al. (2020) created a model that outputs differential electron flux at 24 energy channels from 0.06–293 keV. However, it uses the AE and Dst indices (for descriptions of these indices, see Section 2.3), which includes information that is both internal to the magnetosphere and requires significant processing time. Therefore, the Zou et al. (2020) model cannot be used as a forecast of plasma sheet electron flux.

In Chapter 6, we describe the development and use of a machine–learned, neural network that predicts differential electron flux in the near-Earth plasma sheet from solar wind driving inputs. In so doing, we address gaps that exist in the predictions of existing empirical models of plasma sheet

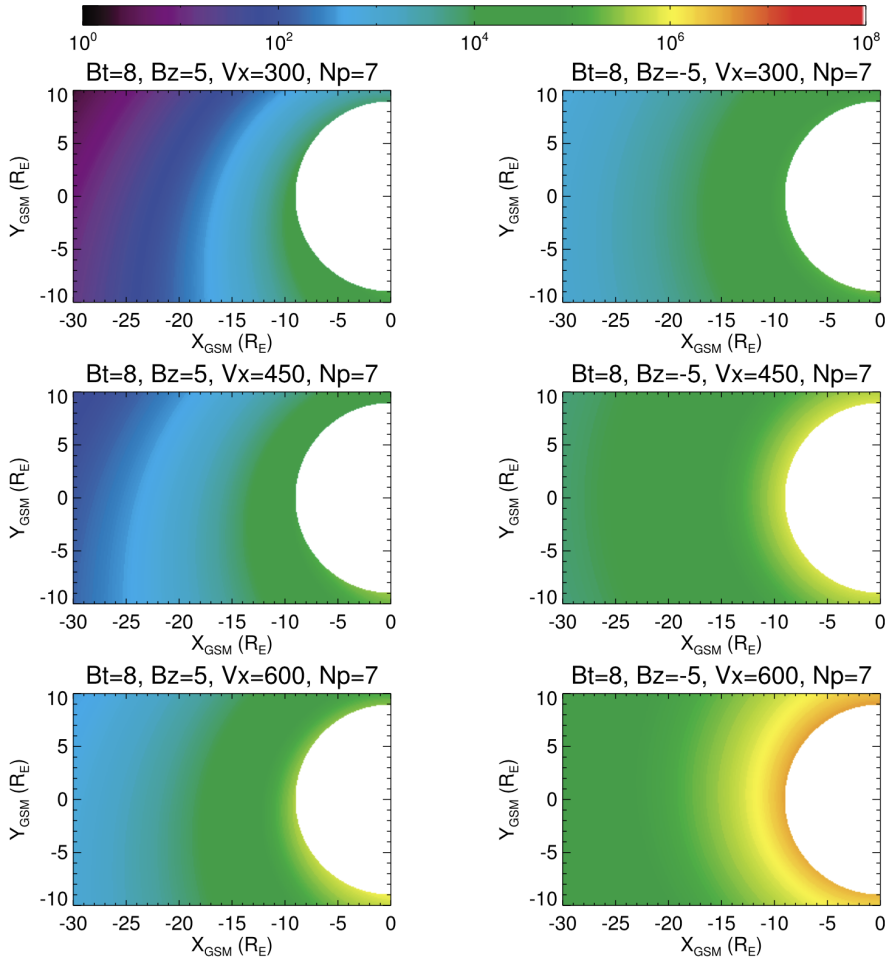

Figure 1.6: Figure 11 of Luo et al. (2011). "Colorcoded plots of the distribution of the [modeled] central plasma sheet electron flux $(\mathrm{cm}^{-2}\,\mathrm{sr}^{-1}\,\mathrm{s}^{-1})$ from the model under different solar wind speed conditions (described on top of each plot)".

electrons. Additionally, we contribute to the growing body of evidence showing utility for machine learning methods in the field of space weather modeling (e.g., Camporeale, 2019). Section 6.1 shows preliminary model development and the necessity of including physical information into the machine learning algorithm. In Section 6.2, we show the results of a more comprehensive model that closes the existing gaps in the previous plasma sheet electron flux models. The Section 6.2 model uses only inputs that are external to the magnetosphere, and it can predict the electron flux at 31 different energies (from 0.08–93 keV) at any location within the near-Earth plasma sheet. We compare this model to an existing model, and we rank the solar wind driving parameters in order of their importance to model output.

CHAPTER 2

Data Description

The majority of the work contained in this thesis relies heavily on data that has been collected and curated through various sources over several decades. We describe some details of the data that we used—why and how they were created, what they represent, and how we obtained them.

2.1 Solar and Solar Wind Data

In all focus areas, identified in Section 1.4, we utilized solar wind data that has been collected from satellites near the L1 Lagrange point in order to quantify the solar wind variations that are effecting the behavior of the near-Earth space environment. These data have been organized and curated by the OMNI (Section 2.1.1) data service. We also use "solar data" in the form of output from an empirical model (FISM-2, Section 2.1.2), in Chapter 6.

2.1.1 OMNI

Originally described by King and Papitashvili (2005), OMNI data represent the state of the solar wind plasma and magnetic field upstream of Earth's bow shock. At $\sim$235 R_E (0.01 AU) towards the Sun along the Sun-Earth line, there exists a gravitational null, or saddle point, where the gravitational forces from the Sun and from the Earth are in approximate balance, which is called the first Lagrange point, or L1. A spacecraft can orbit around this point (see Figure 2.1), and there have been and continue to be satellites that are orbiting L1 and collecting in situ data from various instruments. Spacecraft that are orbiting L1 at the time of this writing and contribute to the OMNI dataset include ACE (Stone et al., 1998) and WIND (Ogilvie & Desch, 1997). For historical records, OMNI also includes data from past spacecraft missions such as IMP 8 (Paularena & King, 1999) and ISEE 3 (Farquhar, 2001). OMNI is a processed conglomeration of data from the individual spacecraft (King & Papitashvili, 2005). The measurements taken near L1 have been time shifted to the presumed nose of Earth's bow shock (as esimated by Farris & Russell, 1994) using

a minimum variance technique for propagating solar wind parameters (Weimer, 2003; Weimer & King, 2008).

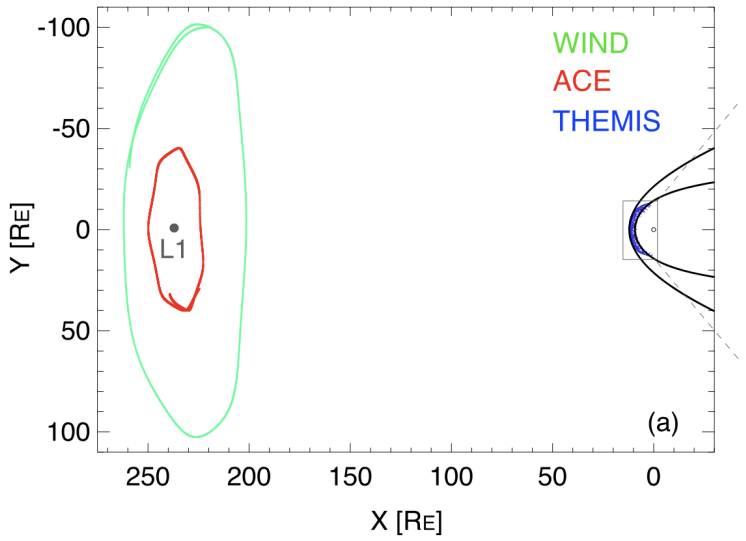

Figure 2.1: Figure 3a of Walsh et al. (2019). The WIND (green line) and ACE (red line) orbits around L1 are for the period April-October 2016. The orbits illustrate the distance to which the solar wind monitoring spacecraft around L1 are typically away from the Sun-Earth $(y = 0)$ line. In this diagram, all coordinates are in GSE. Earth is at $(x = 0,\ y = 0)$. The nominal locations of the magnetopause (closest to Earth) and bow shock (furthest from Earth) are shown as black curves.

2.1.1.1 OMNI Data Products

Available parameters of the solar wind plasma and interplanetary magnetic field include but are not limited to velocity ($\vec{V}_{\rm SW}$), proton density ($N_{\rm SW}$), and magnetic field direction and magnitude (i.e. B_i, denoting the strength of the IMF in the $i-{\rm th}$ direction of some coordinate system). From these, many other quantities can be calculated, such as solar wind dynamic pressure ($P_{\rm dyn} \propto N_{SW} V_{SW}^2$) or convectional electric field ($E_{SW} = -\vec{V}_{\rm SW} \times \vec{B}$). There exists both low resolution (LRO) and high resolution (HRO) OMNI data. The LRO is at one hour, one day, or twenty-seven day cadence. The HRO is available at either one minute or five minute cadence. In Figure 2.2, we show HRO 5-minute OMNI for the day of February 20, 2010, which was a day with typical solar wind and IMF values. We used several of these parameters and more in our investigations. The exact parameters and resolution that we used in each investigation are described in the relevant chapters. All OMNI data were downloaded from the CDAWeb archive at https://cdaweb.gsfc.nasa.gov/pub/. CDAWeb is the Coordinated Data Analysis Web hosted by the Space Physics Data Facility at NASA Goddard Spaceflight Center.

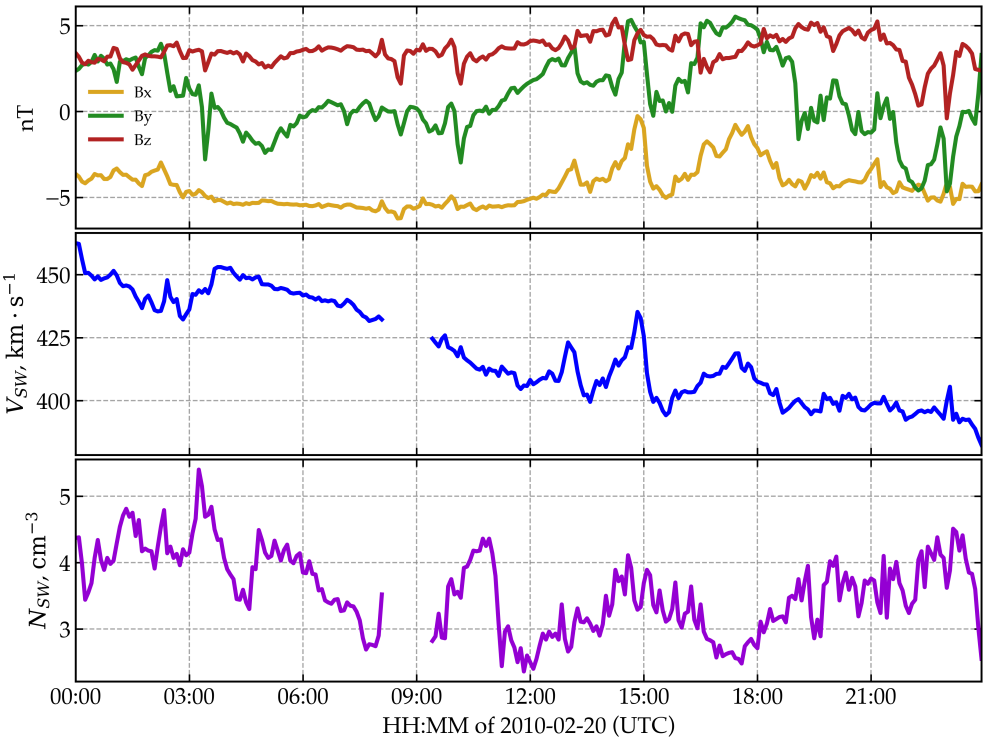

Figure 2.2: One day of typical OMNI data at five minute resolution. Top: IMF in GSM coordinates. Middle: solar wind flow speed. Bottom: solar wind proton density. Note there is missing V_{SW} and N_{SW} data around 09:00.

2.1.1.2 OMNI Uncertainties

Uncertainty of OMNI data that describes the upstream solar wind impacting Earth's magnetosphere comes from multiple aspects. In addition to the systematic uncertainties inherent within the spacecraft instrumentation, the measurements taken at L1 are only taken at one point in space and therefore cannot fully represent the entire state of the solar wind at L1. The spacecraft are anyways never exactly at L1 and at any one time are separated from the Sun-Earth line by tens to hundreds of $\mathrm{R_E}$ (see, for example, Figure 2.3). It is often the case that this separation of spacecraft results in different solar wind measurements at the same time (Figure 2.4), and which measurement OMNI uses can drastically change the data product. Moreover, the flow vector of the solar wind is not always radially outward from the Sun, which means that the solar wind that passes over an L1 orbiting spacecraft may not be the solar wind that hits the nose of Earth's bow shock (e.g., Borovsky, 2017). Additionally, the parcel of solar wind that is monitored by an L1 spacecraft may undergo changes between L1 and the bow shock (e.g., B. Wang et al., 2016). Complicating matters further, after the plasma passes through the bow shock, the plasma and magnetic field that ultimately impacts Earth's magnetosphere is shocked; and, therefore is in a different state than it

was in the pristine solar wind upstream of the bow shock. (e.g. Czaykowska et al., 2001; Shevyrev & Zastenker, 2005). Walsh et al. (2019) have estimated some of the uncertainty associated with these issues by using OMNI data from L1 observations and THEMIS data from inside the magnetosheath and found that the flow pressure between the two has a standard deviation of 0.67 nPa and an IMF clock angle standard deviation of 38°. Finally, OMNI data have missing values. Even though OMNI is sourced from multiple spacecraft, there still were times when none were collecting usable data. The problem of missing data is always something that must be addressed when using OMNI.

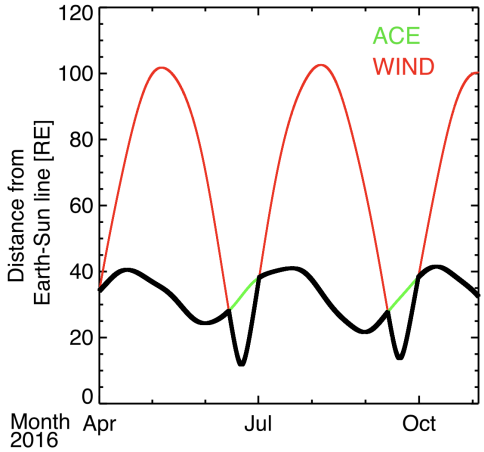

Figure 2.3: Figure 8 of Walsh et al. (2019). Distance of the WIND (red) and ACE (green) spacecraft from the Sun-Earth line during an approximately four-month period. The black trace shows the minimum distance to the Sun-Earth line amongst the two spacecraft. This diagram illustrates typical distances from the Sun-Earth line of spacecraft that contribute data to the OMNI database, introducing uncertainty.

Despite the uncertainties of the OMNI data, a major advantage of using OMNI rather than data directly from the source spacecraft is that OMNI data have been preprocessed and cross-calibrated to provide a uniform and consistent dataset. Furthermore, even if using data directly from the L1 monitors, the uncertainty problems inherent in using L1 measurements still exist. As a final point, L1 orbiting monitors are the current best solution that we have to consistently measure the solar wind and IMF upstream of Earth's bow shock.

2.1.2 FISM-2

We used solar extreme ultraviolet (EUV) photon data in Chapter 6 because EUV photons greatly alter the ionosphere, which is coupled to the near-Earth plasma sheet through field-aligned currents and magnetic field. The Flare Infrared Spectral Model—Version 2 (FISM-2) (Chamberlin et al.,

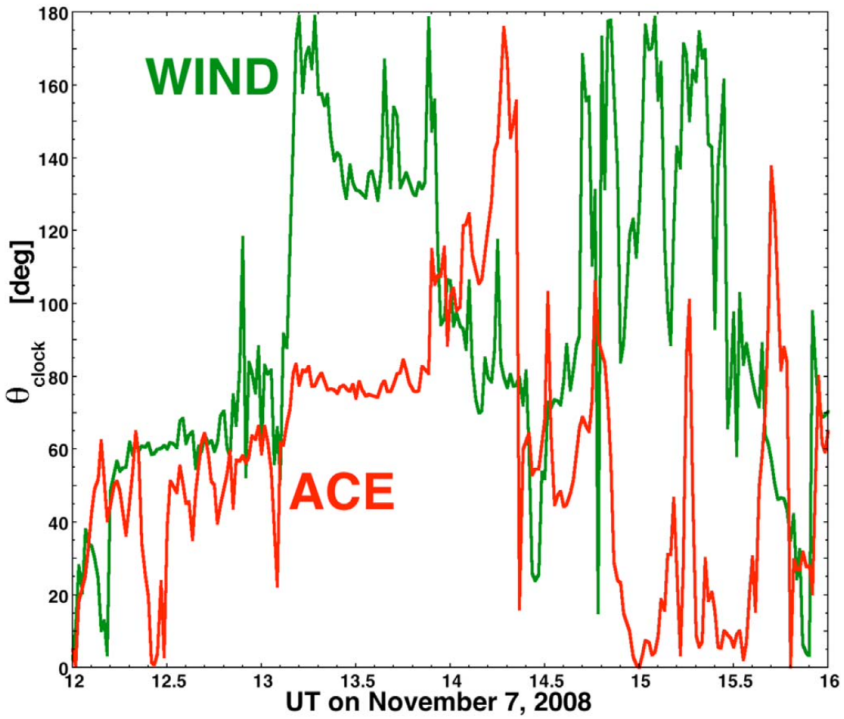

Figure 2.4: Figure 7 of Borovsky (2017). The IMF clock angle, $\theta = \arctan\left(\frac{B_Y}{B_Z}\right)$, observed by the WIND (green) and ACE (red) spacecraft for a four hour period. During this period, the two spacecraft were separated by more than $100\mathrm{R_E}$ (in GSE coordinates, WIND was located at $(X, Y, Z) \approx (235, 89, 14)$ and ACE was at $(X, Y, Z) \approx (234, -38, -12)$). This diagram highlights the fact that the two spacecraft were observing different magnetic structures in the solar wind, which is a typical situation, and is a contribution to uncertainty in OMNI data.

2020) is an empirical model that estimates the flux of solar photons in the ultraviolet spectra of solar radiation. It provides estimates due to solar cycle, solar rotations, and solar flares (see Figure 2.5). To make the estimates, the model ingests data from various solar observing instruments, which currently include the Solar Dynamics Observatory—Extreme Ultraviolet Variability Experiment, Solar Radiation and Climate Experiment (SORCE)—X-ray Photometer System, and SORCE—Solar Stellar Irradiance Comparison Experiment. The model then applies several algorithms to the observations to provide daily and 60-second solar irradiance data products. FISM-2 provides solar irradiance in 0.1 nm spectral bins in a 0–190 nm spectral range.

All FISM-2 data are available and were downloaded through the Laboratory for Atmospheric and Space Physics (LASP) Solar Irradiance Data Center (LISIRD). Specific usage of FISM-2 data in our investigations are described in further detail in Chapter 6.

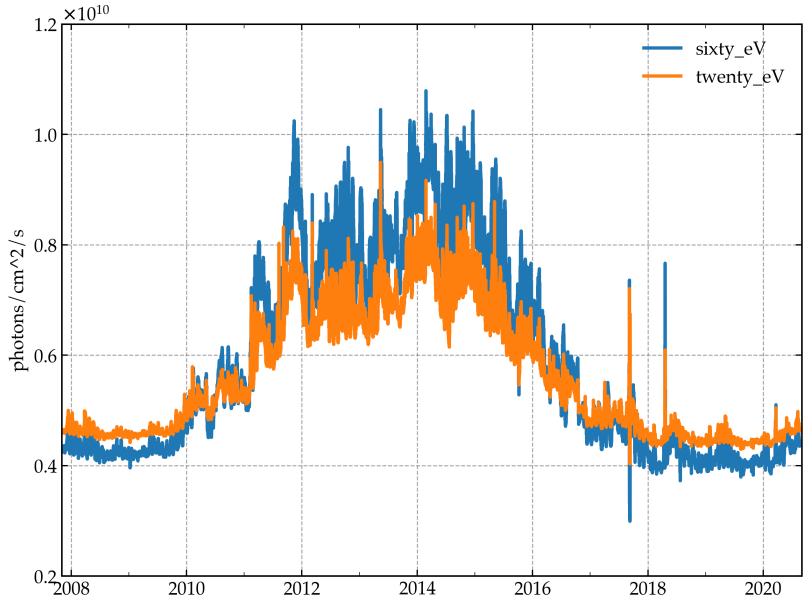

Figure 2.5: FISM-2 model output for years 2008-2020, roughly corresponding to solar cycle 24 (which was approximately December 2008 - December 2019). In these two curves, we can see variation of photon flux based on the solar sunspot cycle (e.g. peak in 2014), solar rotation ($\sim$27 day oscillation) and daily anomalies (e.g. spike from solar flare on September 6, 2017).

2.2 Magnetospheric Spacecraft Data

All of our investigations required using in situ data from spacecraft within the magnetosphere. In Chapter 4, we used data from LANL spacecraft (Section 2.2.2). In the other focused investigations—Chapters 3, 5, and 6—we relied on data from the THEMIS mission (Section 2.2.3).

2.2.1 Particle Fluxes and Distributions

In our investigations, the spacecraft data that we primarily used was either differential particle number flux or differential particle energy flux. For discrete energies, E, the number of particles in solid angle Ω, $N(E, \Omega)$, within energy range $\mathrm{d}E$ of E passing through a surface, $\mathrm{d}A$, of unit solid angle, $\mathrm{d}\Omega$, is defined as differential particle *number* flux, $J(E, \Omega)$ (Equation 2.1). The differential particle *energy* flux, $J_E(E, \Omega)$ accounts for the energy carried by the particles and is calculated by multiplying E into J (Equation 2.2).

$$J(E, \Omega) = \frac{N(E, \Omega)}{\mathrm{d}A, \mathrm{d}E, \mathrm{d}t, \Omega} \tag{2.1}$$

$$J_E(E, \Omega) = EJ(E, \Omega) = \frac{EN(E, \Omega)}{\mathrm{d}A, \mathrm{d}E, \mathrm{d}t, \Omega} \tag{2.2}$$

Spacecraft plasma instruments obtain differential particle fluxes by sweeping through electric potentials (retarding particles within specific energy ranges). The instruments often have multiple view directions and take advantage of the spacecraft spin rotation to cover all (or nearly all) 4π steradians. Then, the particle fluxes are used to estimate a velocity distribution function, $f(\vec{r}, \vec{v})$ (Equation 2.3). In the plasma sheet, these are often assumed to be Maxwellian or Kappa distributions. Bulk plasma properties, like density and temperature, are derived from the estimated distribution functions.

$$J(E, \Omega) = \frac{v^2}{m} f(\vec{r}, \vec{v}) \tag{2.3}$$

2.2.2 LANL MPA & SOPA

The Los Alamos National Laboratory (LANL) has been operating plasma particle instruments onboard a series of geosynchronous orbiting satellites since 1989. The Synchronous Orbit Particle Analyzer (SOPA) (Belian et al., 1992) measures electrons with energy between 50 keV and 1.5 MeV. The Magnetospheric Plasma Analyzers (MPA) (Bame et al., 1993) measure lower energies of electrons, between $\sim$1 eV to $\sim$40 keV. In Chapter 4, we describe in more detail how we acquired and used the particle flux data from these LANL instruments.

2.2.3 THEMIS

The Time History of Events and Macroscale Interactions during Substorms (THEMIS) mission (Angelopoulos, 2008) began science operations in the second half of 2007. For the next two years, 2008–2009, THEMIS consisted of five probes, labeled TH-A, -B, -C, -D, and -E, that orbited the Earth in near-equatorial, highly elliptical orbit planes with apogees from about 8 R_E to about 30 R_E and perigees between 1–2 R_E (see Figure 2.6). When viewed from above the equatorial plane, the orbits of all the spacecraft precess clockwise so that their apogees rotate from local midnight to local noon passing through local dusk. A full 360° precession takes approximately 12 months. The orbits of the THEMIS probes were designed so that they would repeatedly be in near-conjunction within the near-Earth plasma sheet (Figure 2.7). In 2010, two of the probes, TH-C and TH-B, were sent to orbit the Moon to become a different mission (Angelopoulos, 2010). Since 2011 the THEMIS mission has had the three probes TH-A, -D, and -E. The probes have been collecting, processing, and sending to Earth near continuous, in situ plasma and magnetic and electric field data. They have a nominal spin rate of three seconds, but have higher or lower data resolution depending on which mode the spacecraft are in (i.e., boost or slow survey modes). For our investigations, we downloaded THEMIS data at the nominal three second resolution from the NASA Goddard SPDF via the CDAWeb interface.

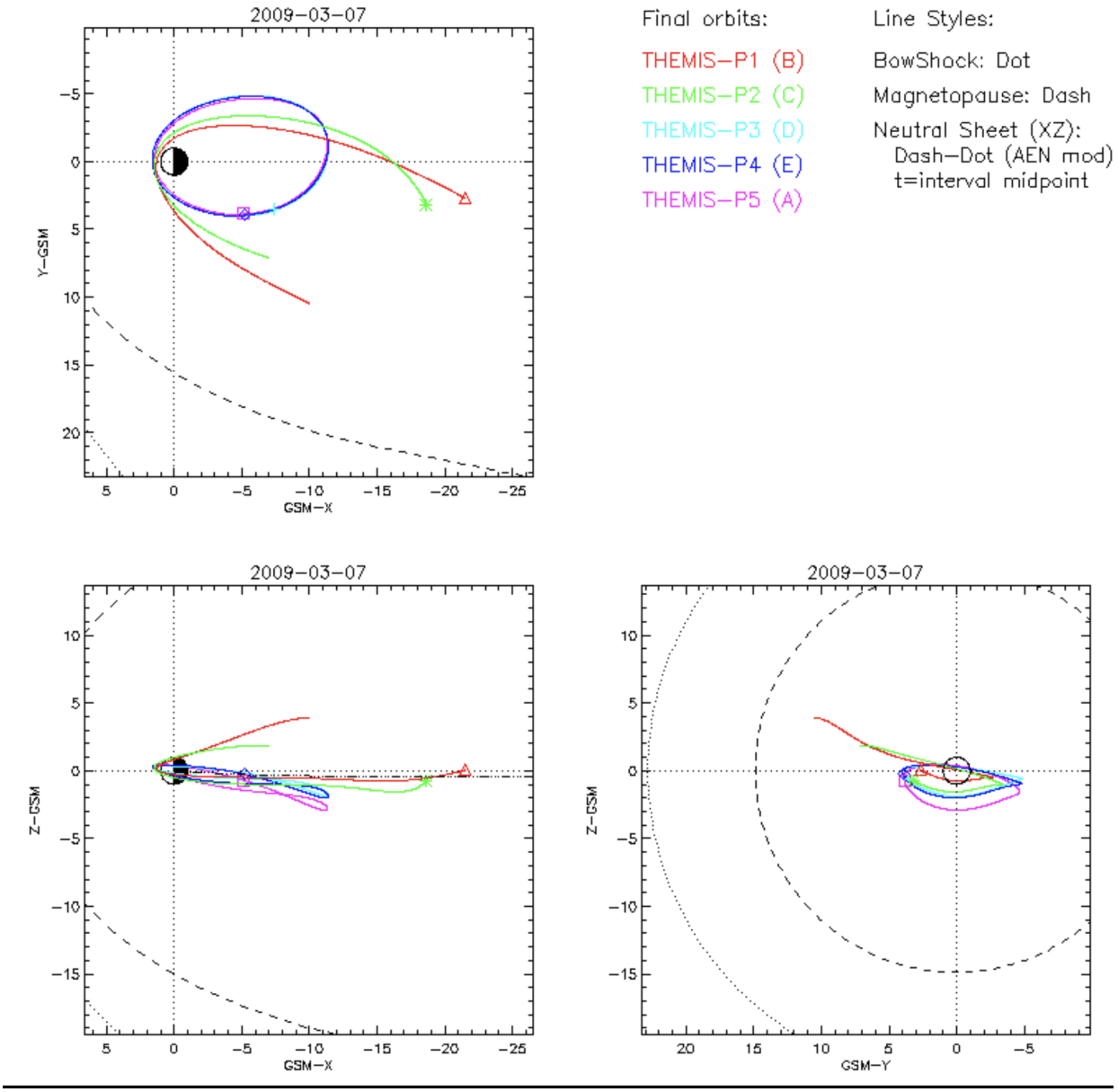

Figure 2.6: Example of typical THEMIS spacecraft orbit trajectories. Shown are the orbit paths for March 7, 2009. The orbits precession such that the apogees rotate through all local times approximately annually. (Summary orbit plot from http://themis.igpp.ucla.edu)

The THEMIS probes each have five instruments: 1) SCM—Search Coil Magnetometer; 2) FGM—Fluxgate Magnetometer; 3) EFI—Electric Field Instrument; 4) SST—Solid State Telescope; and 5) ESA—Electrostatic Analyzer. With the data from these instruments, the THEMIS science team has created several data products. We will briefly describe three of the instruments—ESA, SST, FGM—and a product derived from the combination of data from these instruments,

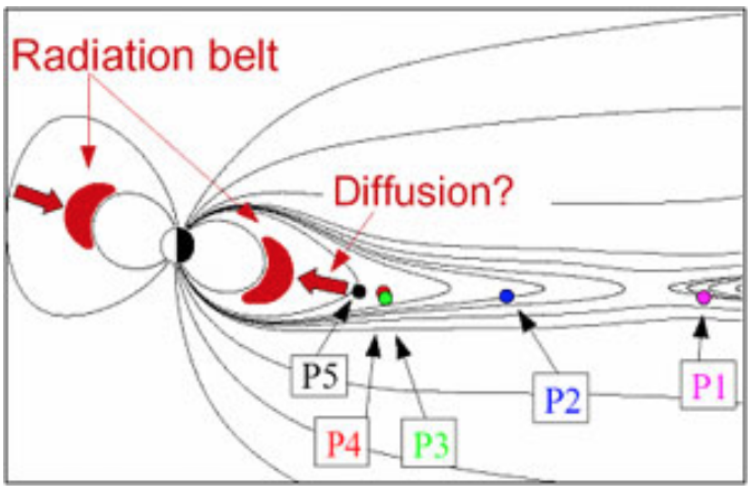

Figure 2.7: Hypothetical THEMIS orbit configuration in a string of pearls alignment along the plasma sheet. The mission was designed to allow multiple periods where the spacecraft would be in a similar configuration. (From http://themis.igpp.ucla.edu/overview.shtml)

called GMOM (Ground calculated MoMents).

2.2.3.1 THEMIS ESA, SST, FGM

The Electrostatic Analyzer (ESA) (McFadden et al., 2008) on the THEMIS spacecraft measures electrons and ions with a 4π steradian field of view for each spin. The energy range for electrons is from 2 eV to 32 keV, in 31 logarithmic steps. The Solid State Telescope (SST) (Angelopoulos et al., 2008) on the THEMIS spacecraft measures electrons and ions. It measures electrons with energy from 25 keV to 900 keV, in sixteen logarithmically spaced energy steps. The Fluxgate Magnetometer (FGM) (Auster et al., 2008) on-board each of the spacecraft measures magnetic field at a resolution of 3 pT. The FGM is deployed on a boom that extends approximately 2 m away from the main bus of the spacecraft to minimize the instrument measuring magnetic field generated by the spacecraft itself. We show an example of observations taken from one of the THEMIS probes in Figure 2.8. FGM data are shown in the top panel. The electron flux data, combining observations from ESA and SST, are in the fourth panel from the top (labeled as 'e-' in the lower-right of the panel).

2.2.3.2 THEMIS GMOM

For both the ESA and SST instruments, onboard plasma moments (i.e., temperature, density) are estimated from the observed counts of ions and electrons (e.g., see Section 2.2.1). There are also ground-calculated moments (GMOM) that have been developed by combining the observations from both the THEMIS SST and ESA instruments. The GMOM dataset contains ion and electron

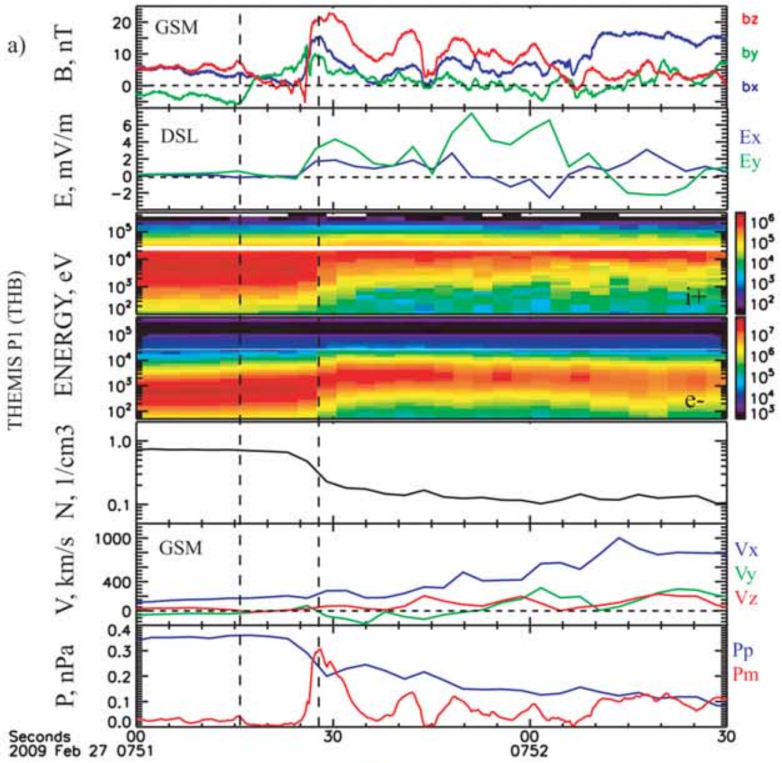

Figure 2.8: Figure 2a of Runov et al. (2009). Example of spacecraft data from one of the THEMIS probes. Panels from top to bottom are magnetic field, electric field, ion energy flux spectrogram, electron energy flux spectrogram, plasma number density, plasma velocity, and plasma pressure. (Particle fluxes are in units of $\mathrm{eV}/(\mathrm{cm}^2 \cdot \mathrm{s} \cdot \mathrm{eV})$.

flux data, magnetic field data from the FGM, and calculated plasma moments. Available plasma moments include electron and ion temperature and density. The electron flux spectrum contains 46 energy channels, in logarithmic steps, from approximately 7 eV–720 keV.

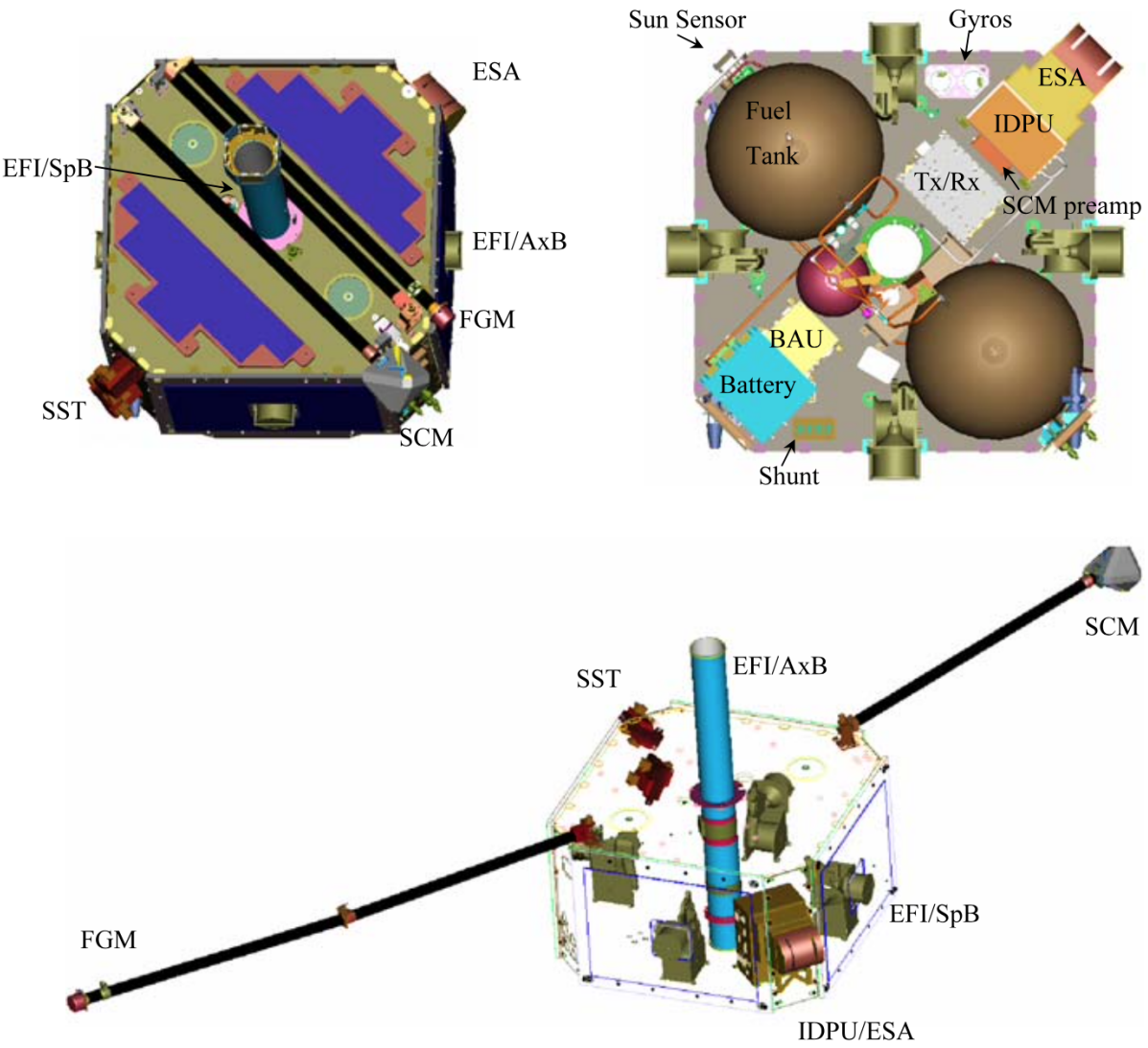

Figure 2.9: Figure 7 of Angelopoulos (2008). Schematic view of the instrument layout for each of the THEMIS probes. "(a) top left: Top view of THEMIS probe indicating locations of the instruments in a stowed configuration; AxB is Axial Boom, SpB is Spin plane Boom; (b) top right: Internal instrument accommodation (c) bottom: Side view of THEMIS probe with magnetometer booms in deployed configuration, revealing instrument locations". The length of the booms are approximately 2 m for the FGM and 1 m for the SCM.

2.3 Ground Magnetometer Data

Magnetometers on the surface of the Earth are an important tool for recording and understanding variations in the space environment. Chapman (1918) was among the first to recognize that terrestrial magnetic field variations were due to changes of electric currents in the near-Earth space

environment. Soon thereafter, researchers started to use the ground magnetometer data to create indices of geomagnetic activity (e.g., Bartels et al., 1939), which synthesize the variations into a single number. There are several geomagnetic indices currently in use, and they each are indicative of a particular aspect of geomagnetic activity, which in turn can provide useful information about geospace phenomena. For example, the Auroral Electrojet (AE; see Section 2.3.3) index is an indicator of the strength of electrical currents in the auroral region of the ionosphere, while the Symmetric-H (SYM-H; see Section 2.3.2) index indicates the strength of a near-equatorial electrical current at 3–6 R_E encircling the Earth (the so-called ring current).

It is important to note that geomagnetic indices are not perfect reflections of the near-Earth space environment. For example, despite tuning each index to a particular current system, data from magnetometers reflect changes in magnetic field associated with changes in *all* electrical currents. The magnetometers that make up each index are primarily responding to local electrical current fluctuations, yet they also are responding to global current fluctuations. Therefore, it is very often the case that strong fluctuations in the geomagnetic field are seen across several or all geomagnetic indices concomitantly. The individual magnetometer stations are also subject to influences from local geological features (i.e., conductivity of the local land mass or proximity to conducting seawater). The sparsity of ground stations also effects the accuracy and reliability of geomagnetic indices. Since the most intense magnetic fluctuations may have occurred where no ground magnetometers exist, geomagnetic indices can only tell us the lower limit of geomagnetic activity (e.g., Rostoker, 1972a). Nonetheless, geomagnetic indices remain a useful tool to help understand ionospheric and magnetospheric activity (e.g., Bergin et al., 2020). In what follows, we give short descriptions of the geomagnetic indices that we used in our investigations.

2.3.1 *Kp*

We used the *Kp* index in Chapters 3 and 4 to provide information on the overall disturbance of the geomagnetic field. The planetary *K* index, *Kp* (Matzka, Bronkalla, et al., 2021), was first described by Bartels (1949). It is the oldest continuous geomagnetic index still in use today, and it is widely used as an indicator of overall magnetospheric activity (e.g., Matzka, Stolle, et al., 2021). Although the list of contributing magnetometer stations has changed over time, there are currently thirteen individual ground stations that contribute to the *Kp* index (Matzka, Stolle, et al., 2021) (see Figure 2.10). Eleven are in the Northern Hemisphere and two are in the Southern Hemisphere. Their locations range from $|45.0|^\circ$ to $|61.2|^\circ$ in magnetic latitude. Longitudinally, seven of thirteen are clustered in Europe, four are in North America, and the remaining two are on the Australian continent. Between the nearest European and Australian *Kp* stations there is a longitudinal separation of 131.6°. We note the clustering of stations and large gap in coverage over

the Asian continent to highlight the previous discussion on the limitations of geomagnetic indices. The distribution of *Kp* stations can be found in Figure 2.10. The top panels show the geographic locations of the thirteen *Kp* ground stations and their locations relative to the geomagnetic field. (The geomagnetic field in Figure 2.10 is represented in quasi-dipole coordinates, which accounts for height differences along the Earth's surface (Laundal & Richmond, 2016).) The lower panels of Figure 2.10 shows the calculated *Kp* index for a single day—September 8, 2017—during which a geomagnetic storm was occurring. The storm resulted in *Kp* values reaching 7–8. For reference, see also Figure 2.11.

The calculation of *Kp* is done only after first calculating *Ks*, which is done after only first calculating *K* for the thirteen stations that contribute to the *Kp* index. The *K* index is a three hour range index for each individual magnetometer station. Each day, for eight three-hour intervals (00–03 UT, 03–06 UT, . . . , 21–24 UT), the range between the maximum and minimum magnetic field strength in both of the horizontal components is recorded. The maximum difference recorded of the two directions is then converted to an integer between 0 and 9 according to a table that is unique to each station and depends on its geomagnetic latitude. As recounted by Rostoker (1972a), a general limitation of the *K* index is that it is biased with respect to the local time of the station for each three-hour period. When a station is near local midnight, for example, the magnetic field tends to experience larger perturbations than at other local times. There is a seasonal dependence for each station as well. To overcome these problems, special conversion tables for each station were created to standardize the *K* values and turn them into the standardized *K*— or *Ks* —index for each station. The *Ks* index also introduced the concept of thirds to the scale, so that in addition to integers, there are also values on the thirds (i.e., $\ldots 1, 1^1/_3, 1^2/_3, 2, 2^1/_3, \ldots$). Finally, *Kp* is calculated as the mean of the *Ks* values of the thirteen contributing magnetometer stations. Further descriptions of the derivations and uses of the *Kp* index can be found in a comprehensive review article by Matzka, Stolle, et al. (2021).

2.3.2 SYM-H

The Symmetric-H (SYM-H) index (Iyemori et al., 2010) is similar to the Disturbance storm time (Dst) index (Sugiura, 1964). Both were designed to indicate the strength of the terrestrial ring current that is especially impactful to equatorial geomagnetic perturbations during geomagnetic storms (e.g., Dessler & Parker, 1959; Sckopke, 1966). We used the SYM-H index to provide information about the strength and duration of geomagnetic storms in our investigations. The main differences between the Dst and the SYM-H indices are that the SYM-H index uses a different set of stations (six instead of four), a slightly different coordinate system, and one-minute cadence instead of the Dst cadence of one hour (Iyemori et al., 2010). There are actually eleven magne-

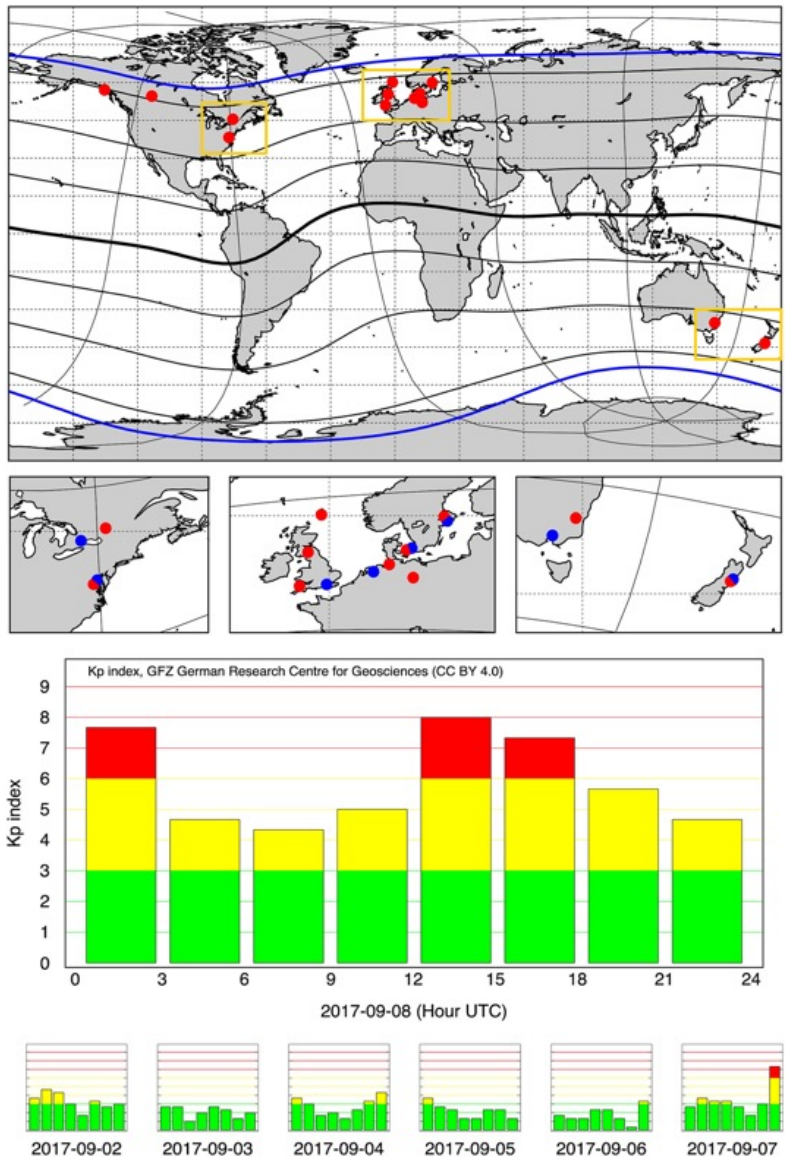

Figure 2.10: Figure 2 of Matzka, Stolle, et al. (2021): "Upper panels: World map of the 13 current Kp-stations (red dots) with geographic coordinates (dotted lines), QD coordinates (solid lines), geomagnetic equator (thick line at 0° QD latitude) and auroral zones (blue lines at +67° and 67° QD latitude). Yellow rectangles indicate the area of the three enlarged regional maps with current (red) and all previous (blue) Kp-stations. Lower panels: Kp index for September 8, 2017 (top) and the preceding six days (bottom row). Plots of this type are provided for all days since 1932. QD, quasi-dipole."

tometers that contribute to the SYM-H index; however, only six each month are chosen (based on data availability and condition of their data) to calculate the index. The stations are located at off-equator magnetic latitudes ($|10|^\circ$ to $|50|^\circ$) such that they can measure magnetic perturbation due to the ring current while minimizing the contribution from the electrojet of the equatorial ionosphere.

SYM-H is a quantity of the magnetic disturbance in the H component (horizontal, dipole direction) of the surface magnetic field. There are also related indices of the symmetric D component (orthogonal to dipole) and asymmetric H and D components. The collection of indices are derived in four steps (recapitulated from Iyemori et al. (2010)):

1. Subtract the main geomagnetic field and the solar quiet daily variation (Sq field, (see e.g., Schunk & Nagy, 2009, Chapter 11.3)) to find the disturbed component. The main field, including the Sq contribution, is defined as the average during the five quietest days for each month.

2. Transform the coordinates into a dipole coordinate system. We expect the effect of the ring current to the H component to be parallel to the dipole axis, since the ring current is generally symmetric about the geomagnetic equator. However, the dipole direction at each observatory is different due to local non-dipole components and anomalies.

3. Calculate the longitudinally symmetric H component by averaging the disturbance component at each minute across the six stations. A latitudinal correction is made to the averaged value: divide the average disturbance value by the six-station average of $\cos(\theta_m)$, where θ_m is the magnetic latitude of each station. The result is the SYM-H index. (At this step, the symmetric D component (SYM-D) is also computed; however, we did not use the SYM-D index in our investigations.)

4. Calculate the asymmetric components by subtracting the symmetric components from the total disturbance field. We did not use the asymmetric components (ASY-D and ASY-H indices) in our analysis, but include them here for completeness.

As previously stated, the SYM-H and Dst have similar calculations. Wanliss and Showalter (2006) performed a detailed comparison between SYM-H and Dst and conclude by recommending that "the SYM-H index be used as a de facto high-resolution Dst index". Essentially, this is what we have done when quantifying the strength of geomagnetic storm periods in Chapters 3 and 4. In Figure 2.11 we show the SYM-H index during a geomagnetic storm in September 2017 where the SYM-H peaks at < -140 nT. Note that this period overlaps that shown in Figure 2.10. The large drop in SYM-H occurs during the same period when *Kp* is reaching values of 7–8.

2.3.3 AE

The Auroral Electrojet (AE) indices (T. N. Davis & Sugiura, 1966; Nosé et al., 2012) provide a measure of global maximum amplitude of the auroral electrojet currents. They represent the ionospheric and coupled magnetospheric activity in the polar and auroral regions, and they are

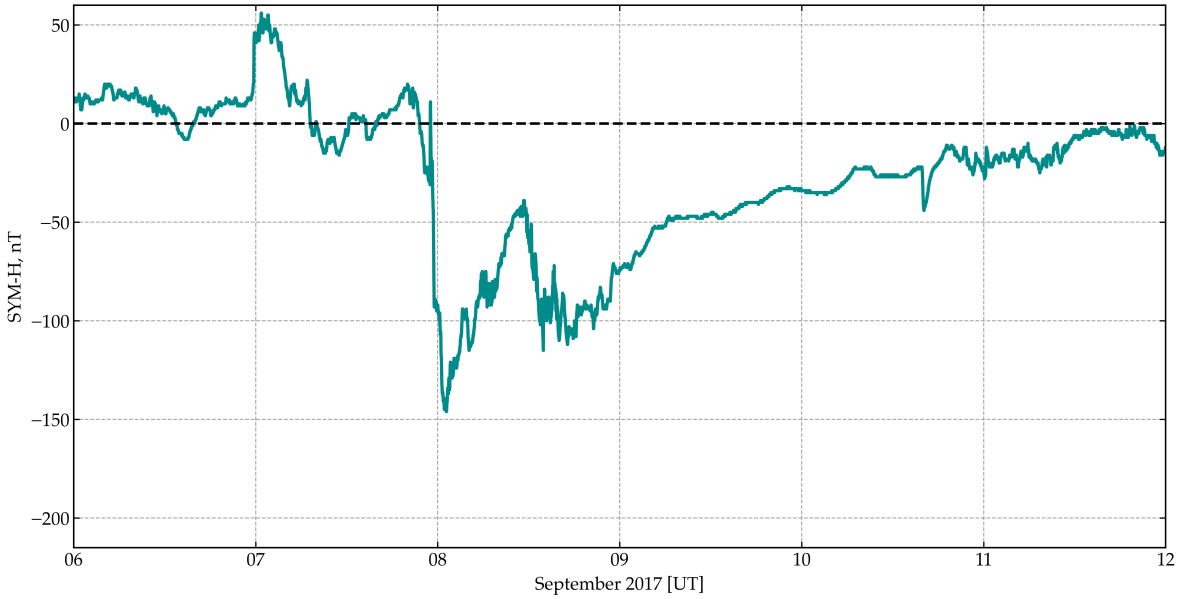

Figure 2.11: SYM-H index from September 6–11, 2017, showing a geomagnetic storm period.

used as an indicator of substorm activity. We used the AE indices as indicators of substorm activity in Chapters 3 and 4.

The AE indices include four individual indices: AL [Auroral Electrojet Lower], AU [Auroral Electrojet Upper], AE [(AU−AL)], and AO [(AU+AL)/2]. The AE index is calculated with data from twelve ground magnetometers that are located in the Northern hemisphere near the auroral latitudes between 65° and 70° North in geomagnetic coordinates. They are spread longitudinally around the globe to provide coverage of magnetic perturbations at a wide range of local times. For each month, the data from each station is first normalized by subtracting a baseline magnetic field. The baseline is the average of the five geomagnetically quietest days of that month. Then, at each minute, the largest and smallest deviations of the 12 stations are recorded. These create an envelope of upper (AU) and lower (AL) extents, from which AE and AO are calculated. Figure 2.12 shows and example of the AE indices for one day. AE enhancements and AL decreases are used as indicators of substorm onset (e.g. Nosé et al., 2012). However, as T. N. Davis and Sugiura (1966) pointed out when they introduced the AE index, a limited number of stations may not provide sufficient coverage to capture the maximum amplitude of the auroral electrojet. This is especially problematic if data from one or more of the stations are missing, as is the case in Figure 2.12.

2.3.4 SME

The SuperMAG network (Gjerloev, 2012) extends the coverage of ground magnetic measurements beyond those used in *Kp*, SYM-H, and AE. The SuperMAG database has uniform data from a

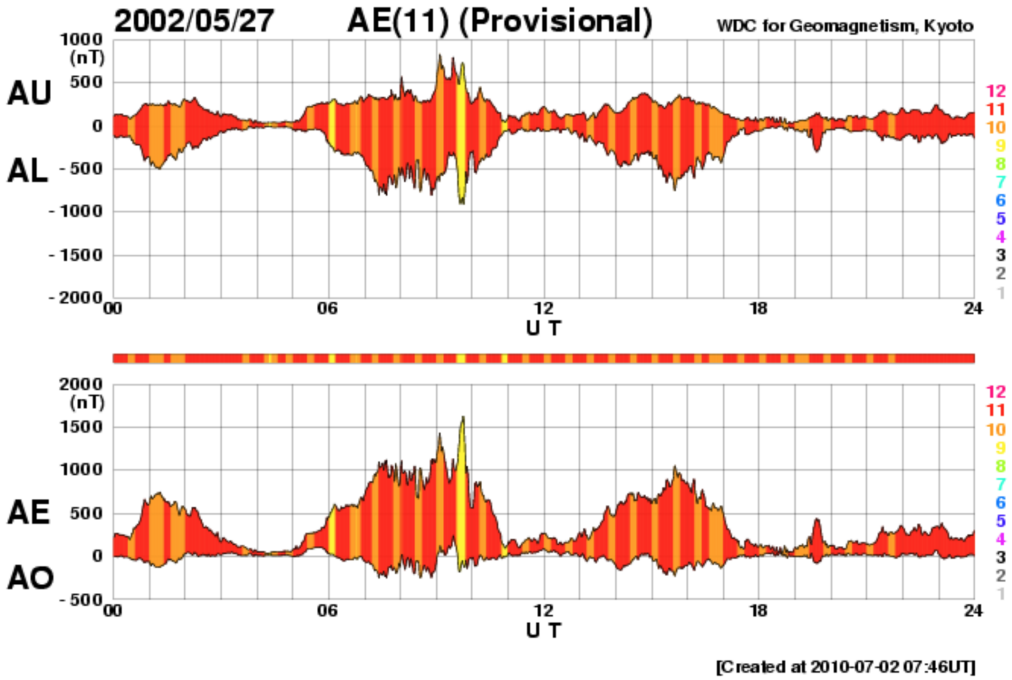

Figure 2.12: The four AE indices (AU, AL, AE, AO) plotted at each minute for one day. The color indicates the number of stations that had available data at that time. (Chart copied from https://wdc.kugi.kyoto-u.ac.jp/.)

collection of over 300 ground magnetometers. The ground station locations are shown in Figure 2.13. Using the expanded set of magnetometers, the SME indices, which are analogous to the AE indices, are calculated. The calculation of SME uses the same method as the calculation of AE, except instead of using only twelve magnetometers (as in the case of AE), the number of magnetometers in SME increases over time (as data from more magnetometers are added to the database), using, for example, over 110 stations during the previous solar maximum (Bergin et al., 2020). The greater number of magnetometers used in the calculation of SME allows for a more comprehensive picture of the state of the magnetosphere at any one time. It also helps to alleviate a limitation of ground magnetic indices that arises from the lack of coverage. The SME indices include SML, SMU, SME, and SMO, which are completely analogous to AL, AU, AE, and AO, respectively. See Figure 2.14 for a single day—May 27, 2002—of SMU, SML, and SME index data. Figure 2.14 covers the same period shown in Figure 2.12, and thus the curves for the analogous indices (AU↔SMU and AL↔SML) are similar. The top panel of Figure 2.14 shows the much greater number of ground stations compared to the AE indices used in the calculation of the SME indices during this period. In addition to index values, the SuperMAG data contains information of the magnetic latitude and longitude of the ground station that contributed to the index at each minute. We used SME data, including the station location information, in Chapter 5.

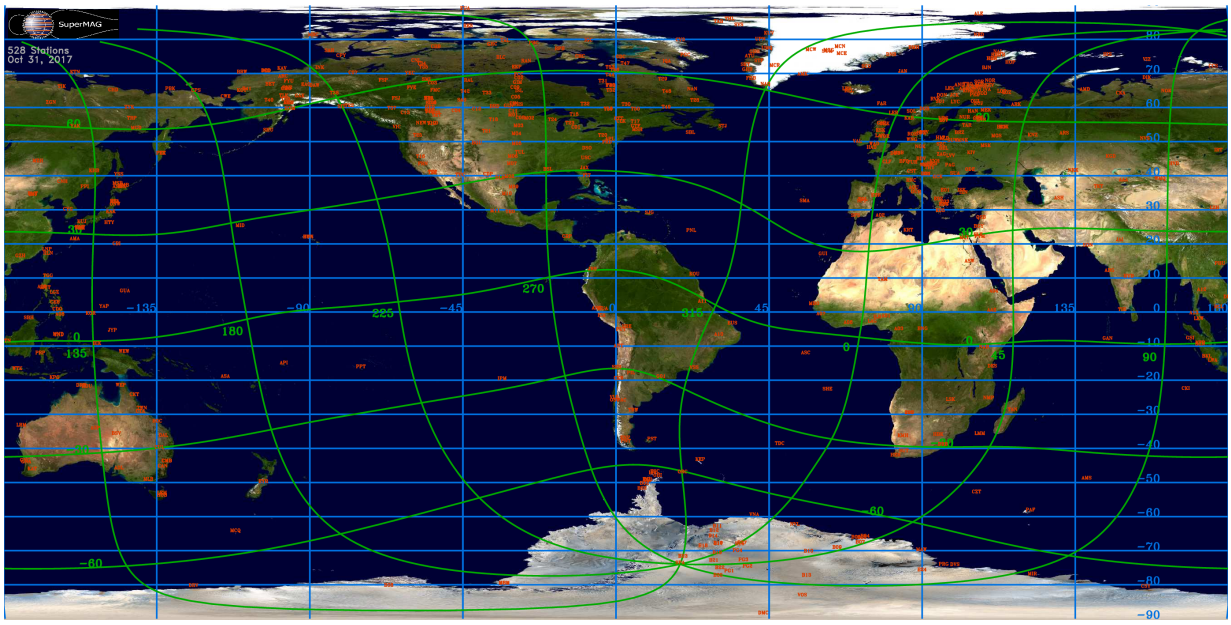

Figure 2.13: The locations of the SuperMAG ground stations (as of October 31, 2017) are labeled in red (with their International Association of Geomagnetism and Aeronomy codes.) Blue lines are geomagnetic coordinates. Green lines are geographic coordinates. Image taken from SuperMAG website: https://supermag.jhuapl.edu/.

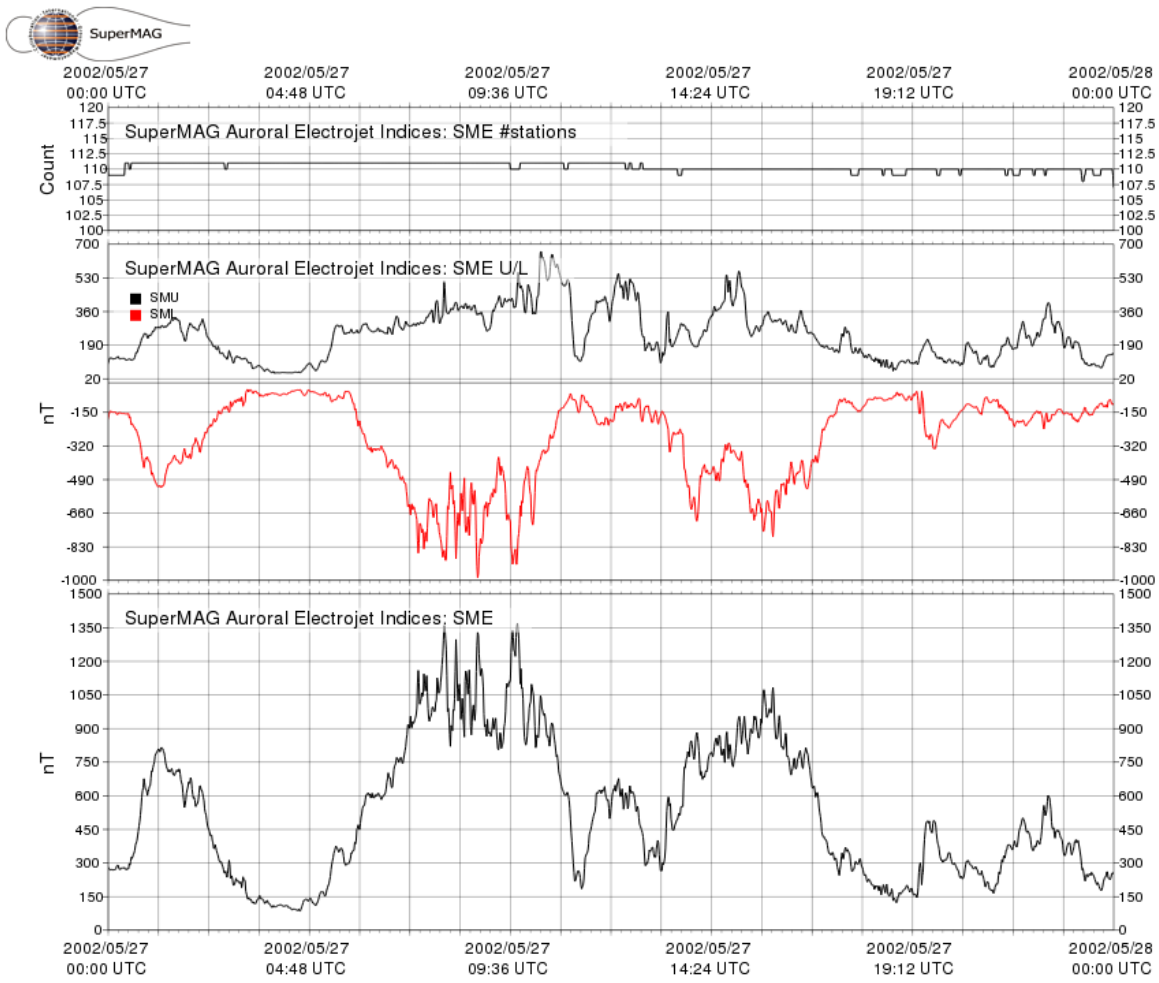

Figure 2.14: The SuperMAG SME indices during May 27, 2002. Top panel: number of ground stations used at each time step. Middle panel: the SMU and SML indices. Bottom panel: The SME index. Chart downloaded from https://supermag.jhuapl.edu/.

CHAPTER 3

Average Climatic Electron Fluxes

3.1 Introduction

It has long been observed that fluxes of superthermal electrons in the near-Earth magnetotail and plasma sheet increase with higher geomagnetic activity (e.g., Anderson, 1965; Montgomery, 1968; Vasyliunas, 1968). Following these early studies, a few others examined the correlation between plasma sheet electron fluxes with geomagnetic indices. Using data from ISEE 1 (Ogilvie et al., 1977) at radial distances >12 R_E, Christon et al. (1989) found that during periods with AE <100 nT, the spectral shape of electrons between tens of eV and several hundred keV was best described by a kappa distribution, with κ typically in the range 4–8. However, for times when AE >100 nT, Christon et al. (1991) reported that the plasma sheet electron population could no longer be represented with a kappa-like distribution. Especially for the superthermal electrons >24 keV there was a significant increase in flux for periods when AE >100 nT than during AE <100 nT periods. Later, Åsnes, A. et al. (2008) described results from a survey of plasma sheet superthermal (40–400 keV) electrons observed by the Cluster spacecraft (Escoubet et al., 2001) during 2001–2004. They note that there was an increase in superthermal electron flux with increasing geomagnetic activity as indicated by the *Kp* index; however, this correlation was also strongly connected to the increase in plasma temperature that occurred during higher *Kp* levels.

Data from the Cluster mission was also used by Burin des Roziers, Li, Baker, Fritz, Friedel, et al. (2009) to correlate superthermal electron fluxes in the plasma sheet with solar wind and IMF parameters. In addition to Cluster (this study using data from 2001–2005), Burin des Roziers, Li, Baker, Fritz, Friedel, et al. (2009) also used Geotail (Nishida, 1994) data for the plasma sheet electrons and they used ACE (Stone et al., 1998) data for solar wind and IMF measurements. Among their findings, they note that there is a strong, positive correlation between solar wind flow speed, V_{SW}, and >38 keV electron flux in the plasma sheet; and, evidence of a weak, negative correlation between solar wind density and plasma sheet electron flux (of the same energies). Moreover, during periods of southward IMF, the fluxes of energetic electrons in the plasma sheet

were found to be enhanced. Burin des Roziers, Li, Baker, Fritz, Friedel, et al. (2009) also examined timing delays between solar wind observations and plasma sheet electron flux correlations. They determined that the highest correlation between plasma sheet electron flux and $V_{\rm SW}$ occurred after a time delay of three hours, regardless of radial distance. A subsequent study of relating solar wind and IMF parameters to energetic plasma sheet electron flux was undertaken by Luo et al. (2011). In the Luo et al. (2011) study, ACE data was again used for interplanetary parameters; however, only Geotail data (not Cluster) was used for the plasma sheet electron observations. Similar to Burin des Roziers, Li, Baker, Fritz, Friedel, et al. (2009), Luo et al. (2011) showed that there are higher fluxes of >38 keV electrons during periods of high $V_{\rm SW}$ and southward IMF. They report that the best correlations between $V_{\rm SW}$ and >38 keV electron flux in the plasma sheet occurred after a time delay of one hour.

A few studies statistically examined the plasma sheet spatial distributions of electron moments of density and temperature. Using 11 years of Geotail data, C.-P. Wang et al. (2007) binned electron densities (at $-30\,{\rm R_E} < {\rm X_{GSM}} < -8\,{\rm R_E}$, $|{\rm Y_{GSM}}| \leq 25\,{\rm R_E}$) by solar wind density ($N_{\rm SW}$), $V_{\rm SW}$, and the magnitude of the IMF B_Z. Amongst their findings, they determined that during northward IMF and with increasing $|{\rm IMF}\ B_Z|$, the electron density increases as the temperature decreases in the central plasma sheet, indicating a larger increase in the lower, thermal energy than in the higher, superthermal energy. Later, C.-P. Wang et al. (2011) used THEMIS data from 2007–2010 to examine the flux of electrons in the near-Earth plasma sheet. They binned the data into two periods—high magnetospheric convection (indicated by the polar cap index) and low magnetospheric convection. It was noticed that there was on average an order of magnitude greater flux for electrons in the post-midnight region of the near-Earth plasma sheet than for electrons in the afternoon region.

In this chapter, similar to the aforementioned studies, we examine the relationships between solar wind, IMF, and geomagnetic activity with energetic electron flux in near-Earth space. Novel to our study is the use of more than 12 years of data sampled at a much higher frequency than past studies, resulting in hundreds of times more samples. For example, the Burin des Roziers, Li, Baker, Fritz, Friedel, et al. (2009) and Luo et al. (2011) studies used 3929 and 4611 plasma sheet samples of electron flux, respectively—in our study, we use close to 2 million plasma sheet samples.

Climatic averages and correlations taken on the order of a solar sunspot cycle have not been performed. Until recently, there has not been a spacecraft mission with duration long enough to cover all of near-Earth space, including the full width of the near-Earth plasma sheet, during a full sunspot cycle. We survey 12 years of electron flux data during the most recent sunspot cycle (solar cycle 24) from the Time History of Events and Macroscale Interactions during Substorms (THEMIS) mission. We correlate the flux data with solar wind driving parameters, taken from

OMNI, and with geomagnetic activity levels as indicated by geomagnetic indices. We describe our data selection process and subsets by driving parameters in Section 3.2. In Section 3.3, we present the climatic, average (median) electron flux values during several ranges of solar wind driving parameters and at several radial distances. We synthesize our findings and explore methods of future research directions in Section 3.4.

3.2 Data & Methods

We use multiple data sources in order to obtain long-term averages of superthermal electron fluxes in near-Earth space and their relationship to solar wind parameters and geomagnetic conditions. The electron flux data that we used comes from the THEMIS mission. For solar wind and IMF parameters, we used the OMNI dataset. Geomagnetic activity is distilled by the geomagnetic indices *Kp*, AE, and SYM-H. These data are described in more detail in Chapter 2.

3.2.1 THEMIS Electron Flux Survey

The THEMIS mission has been operating in near-Earth space since 2007 (Angelopoulos, 2008). Originally, there were five identical probes—but in 2010 two were sent to orbit the Moon as a spin-off mission (Angelopoulos, 2010). The three probes remaining in Earth orbit, labeled Th-A, -D, and -E, have highly elliptical orbits with perigees $\sim$1.5 R_E and apogees $\sim$12 R_E. Each of the probes carry electrostatic analyzer (ESA) (McFadden et al., 2008) and solid state telescope (SST) (Angelopoulos et al., 2008) instruments, which together observe electrons in the energy range of a few eV to several hundred keV. The flux of electrons in several energy channels have been combined into a single data product called GMOM (ground-calculated moments, level 2). For this study, we used data from the pterf (ESA Reduced, SST Full) electron flux product. The GMOM pterf data are available at 3-second resolution, and the electron fluxes are provided as differential energy flux in units of $\mathrm{eV}/[\mathrm{s\ sr\ cm^2\ eV}]$. Data from times when the ESA instrument was saturated were removed; however, if only the SST instrument was saturated, we retained the data, in accordance with the discussions by Dubyagin et al. (2019) and Stepanov et al. (2021). For easier comparison with OMNI HRO 1-minute and geomagnetic index data, we down-sampled the GMOM data to one minute by taking the mean at each minute. Then, we converted the flux units to differential number flux ($1/[\mathrm{s\ sr\ cm^2\ keV}]$).

The one-minute averaged data from all three probes—Th-A, -D, and -E—were combined into a single dataset for the period from December 2007 to September 2020. Our dataset contains the electron differential number flux in 31 energy channels from 83 eV to 93 keV. The full list of energy channels used are in Table 3.1. Observation locations in Geocentric Solar Magnetic (GSM)

coordinates were determined by the orbit data files from the THEMIS mission and their timestamps were matched with those from the GMOM data. The location of each sample is specified by radial distance, $\mathrm{R_{dist}} = \sqrt{X^2_{\mathrm{GSM}} + Y^2_{\mathrm{GSM}}}$ and MLT. We used observations from all magnetic local times and all radial distances from 2–12 $\mathrm{R_E}$ for this study. Since the orbits of the THEMIS spacecraft are close to the equatorial plane, we declined to differentiate by the Z_{GSM} direction. Included in the GMOM data set are calculated values for electron and ion temperature, and magnetic field. We used these data to calculate plasma beta, defined as the ratio between the thermal pressure, P_k, and the magnetic pressure, P_B. We calculated the thermal pressure assuming isotropic distributions for both the ions and electrons, as in Equation 3.1.

$$\beta = \frac{P_k}{P_B} = \frac{2\mu_0 k_B (N_i T_i + N_e T_e)}{B^2} \tag{3.1}$$

In Equation 3.1, B is the magnetic field magnitude, μ_0 is the permeability of free space, k_B is Boltzmann's constant, N_i and N_e are the ion and electron number densities, and T_i and T_e are the ion and electron temperatures, respectively. For the spatial region $\mathrm{R_E} > 8$ and magnetic local time (MLT) 18–00–06 (18 to 06 through local midnight), we only include THEMIS data where the calculated plasma β is greater than unity. This spatial region is of particular interest as the approximate location of the near-Earth plasma sheet, and by restricting observations to $\beta > 1$ we impose a higher likelihood that observations in this region were taken within the plasma sheet (e.g., Baumjohann et al., 1989).

Table 3.1: The full list of energy channels used in our THEMIS electron flux survey. This channel listing is also used in Section 6.2 for development and output of a neural network model.

Energy channels (in keV)			
0.08	0.74	6.68	29.0
0.11	0.98	8.79	30.0
0.14	1.28	11.6	31.0
0.19	1.69	15.2	41.0
0.25	2.22	20.0	52.0
0.32	2.93	26.4	65.5
0.43	3.86	27.0	93.0
0.56	5.07	28.0	

3.2.2 Relational Parameters—SW, IMF, & Geomagnetic Indices

We related the electron flux obtained by THEMIS to solar wind, IMF, and geomagnetic index parameters. From OMNI, we used solar wind parameters of flow speed (V_{SW}) and dynamic pressure

(P_{dyn}). We used IMF data of B_Y, B_Z, and $|B|$ in Geocentric Solar Magnetic coordinates, where $|B|$ is the IMF magnitude. With these base parameters, we calculated the Kan & Lee solar wind electric field, E_{kl} (Kan & Lee, 1979). Defined in Equation 3.2, E_{kl} is a proxy for the dayside reconnection rate between the IMF and the magnetopause based on V_{SW}, $|B|$, and the IMF clock angle, $\theta = \tan^{-1}\left(\frac{B_Y}{B_Z}\right)$.

$$E_{kl} = V_{\mathrm{SW}}|B| \sin\left(\frac{\theta}{2}\right) \tag{3.2}$$

Geomagnetic activity levels are determined using geomagnetic indices of AE, SYM-H, and *Kp* (see e.g., Section 2.3). The AE and SYM-H data are provided by the World Data Center for Geomagnetism at Kyoto, Japan (Iyemori et al., 2010). The *Kp* (Planetarische Kennziffer) index data are maintained and provided by the GFZ Helmholtz Center for Geosciences at Potsdam, Germany (Matzka, Bronkalla, et al., 2021). For SYM-H and *Kp* indices, we used data from 2007–2020, matching the period of our THEMIS data survey. Provisional AE index data past mid-2018 were not yet available at the time of this study; consequently, we used AE data from years 2007–2017 only.

3.2.3 Sample Subsets

Binning the electron flux observations by solar wind, IMF, and geomagnetic activity across all twelve years of the THEMIS survey provides a clearer picture of what the average, climatic flux levels are based on solar wind driving and geomagnetic activity. For various ranges of the solar wind, IMF, and geomagnetic index parameters, we created subsets of the THEMIS survey data. For example, for all years 2007–2020 we subset the THEMIS data for when *Kp* values were between 0–1. Then, we calculated sample summary statistics like mean, standard deviation, and median values for all energy channels. There are also subsets using the previous 60 minute averages of some of these parameters. The listing of ranges by solar wind, IMF, and geomagnetic index parameters are in Table 3.2. Subsets that use the parameter values at the same time as the THEMIS observations, we labeled as 'instantaneous'. Subsets that use the mean of the previous 60 minute period relative to the THEMIS observations are labeled as '60-min mean'. The subsets by parameter are applicable to the radial style plot type, as in Figure 3.1, and they are listed in the middle columns of Table 3.2. Note that we did not create radial plots for all parameters and the parameters without radial plots are labeled with 'n/a' in Table 3.2).

We also created subsets based on the THEMIS observing distance from Earth. The distance subsets provide information about the climatic electron flux for each parameter for all local times at a particular, narrow band of distance from Earth. For each parameter, if we show plots using the distance subsets (e.g., Figure 3.11), we indicate in Table 3.2 with a *yes*; otherwise, with a *no*.

There are 20 distance subsets, ranging from 2–12 R_E in 0.5 R_E bins. The binned subsets for the AE index only contain data from 2008–2017 due to the previously noted lack of available provisional AE data past mid-2018.

Table 3.2: The listing of subset ranges by parameter type. Note that not all parameters have radial plots. The third column shows whether distance plot types are available for each parameter. See text for descriptions of radial and distance plot types.

SW & IMF Parameters	Radial Plot Ranges	Distance Plots?	Geomagnetic Indices	Radial Plot Ranges	Distance Plots?
V_{SW} instantaneous	$<$400 km $\cdot$ s^{-1} [400, 500) km $\cdot$ s^{-1} [500, 600) km $\cdot$ s^{-1} [600, 700) km $\cdot$ s^{-1} $>$700 km $\cdot$ s^{-1}	*yes*	AE instantaneous	n/a	*yes*
E_{kl} instantaneous	[0, .25) mV $\cdot$ m^{-1} [.25, .5) mV $\cdot$ m^{-1} [.5, 1) mV $\cdot$ m^{-1} [1, 2) mV $\cdot$ m^{-1} $>$2 mV $\cdot$ m^{-1}	*no*	AE 60-min mean	$<$100 nT [100, 300) nT [300, 600) nT [600, 1600) nT $>$1600 nT	*no*
P_{dyn} instantaneous	[0, 1) nPa [1, 5) nPa [5, 10) nPa $>$10 nPa	*no*	SYM-H instantaneous	$<$-160 nT [-160, -60) nT [-60, -20) nT [-20, 20) nT $>$20 nT	*yes*
IMF B_Z 60-min mean	$<$-10 nT [-10, -5) nT [-5, 0) nT $>$0 nT	*yes*	*Kp* instantaneous	[0, 1) [1, 2) [2, 3) [3, 4) [4, 5) [5, 9)	*no*

3.3 Average Fluxes by Solar Wind and Geomagnetic Activity

We examined the long-term trends that solar wind driving and IMF parameters have on superthermal electron flux in near-Earth space; and, we examined the relationship of electron flux to varying levels of geomagnetic activity. The solar wind, IMF, and geomagnetic index parameters that we used are listed in Table 3.2. For most parameters, we used the THEMIS survey subsets (as defined in Section 3.2.3) to create two types of plots—radial and distance. The radial plots have the form of Figure 3.1 and the distance plots have the form of Figure 3.11. We do not show radial and distance plots for every parameter listed in Table 3.2.

3.3.1 Solar Wind, IMF, and Geomagnetic Index Subsets

Parameter subsets of the THEMIS survey are shown with radial plots. For all radial type figures (i.e., Figure 3.1), the two dimensional plane defined by R_{dist} and MLT is segregated into bins of size 0.5 R_E by 0.5 MLT. In each bin, there are a number of one-minute THEMIS observations that occurred during the specified range of parameter values. The value shown in each bin is the median $\log_{10}$ flux value (in $\log_{10}(1/[\mathrm{cm}^2\ \mathrm{s\ sr\ keV}])$ units) of all these observations. For example, Figure 3.1 shows the median electron flux for approximate energy of 12 keV when V_{SW} is between 500 and 600 $\mathrm{km \cdot s^{-1}}$. For this criterion—V_{SW} between 500 and 600 $\mathrm{km \cdot s^{-1}}$—the number of observations in each bin is shown in Figure 3.2. We show only three ranges of the number of samples to highlight that there are sufficient samples in each bin to obtain meaningful statistics. There are more than 100 samples per bin, and often more than 1000 samples per bin for this criterion. However, subsets for parameter ranges of rare periods have many less samples—when V_{SW} >700 $\mathrm{km \cdot s^{-1}}$ (not shown), for example, most bins have fewer than 100 samples and many have fewer than 10, or none at all.

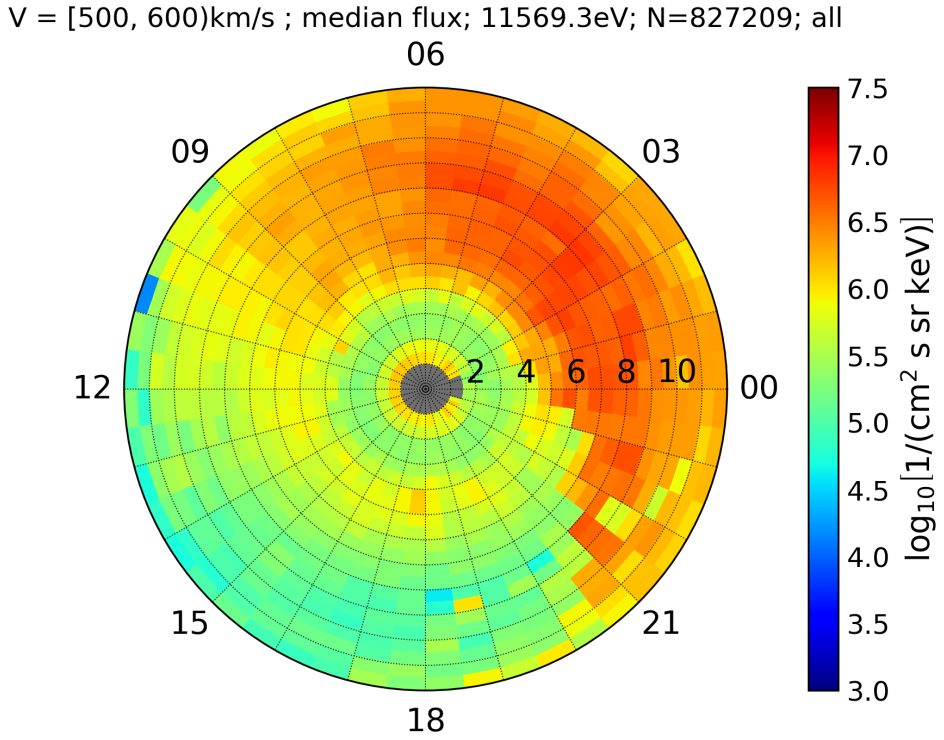

Figure 3.1: Median ~11.6 keV electron flux during solar wind speed values of [500, 600) $\mathrm{km \cdot s^{-1}}$. The color in each spatial bin is the median flux value at this energy for all observations when the solar wind speed was between 500 and 600 $\mathrm{km \cdot s^{-1}}$. Grey color indicates that there were no observations in that spatial bin.

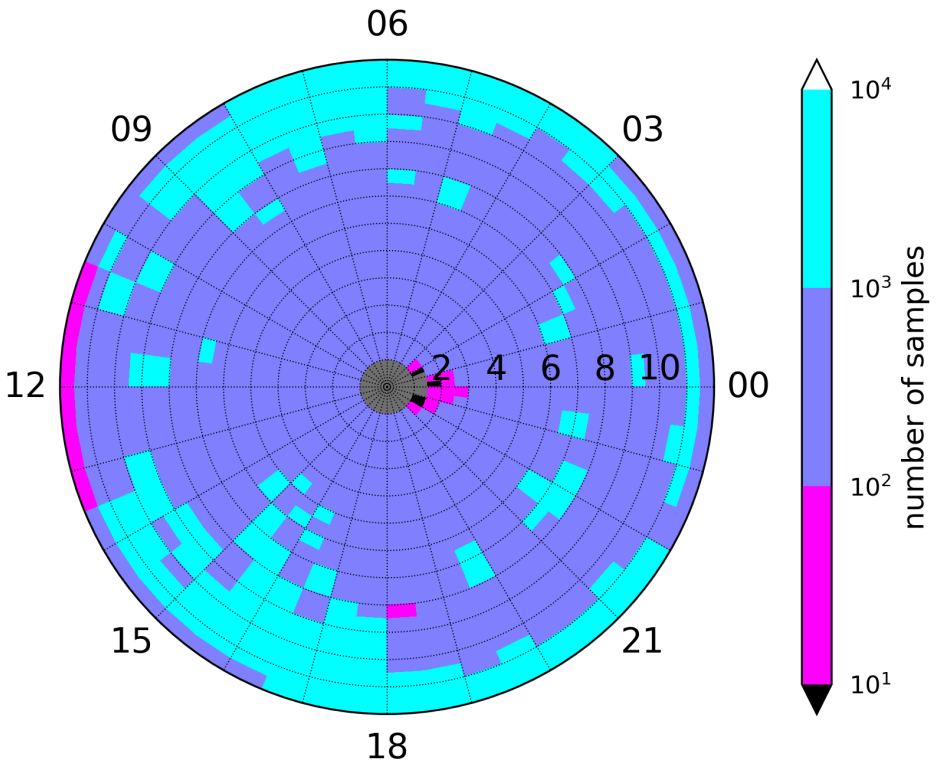

Figure 3.2: Number of observations during $V_{\rm SW}$=[500, 600) $\rm km \cdot s^{-1}$. The color in each spatial bin represents the number range of observations. If black, then less than 10; white, greater than 10^4; grey, no observations.

We organized the radial plots into groups by energy for selected solar wind, IMF, and geomagnetic index parameters at four different energy channels. The 0.3 keV energy channel represents the sub-thermal to thermal electron population and will be where the bulk of the electrons are most of the time. The 2 keV energy channel is in the range of thermal electrons for typical near-Earth plasma sheet material. The 12 keV energy channel is just above the typical thermal energy range and is in the transition into the superthermal electrons. The 52 keV energy channel is well into the superthermal energy population and, as will be evident in the following figures, is the low end of the trapped population from ∼4-6 $\rm R_E$.

In Figure 3.3, we show the median values of 0.3 keV electron flux for three categories of solar wind and IMF driving—weakest, slight, and strong. The four parameters that we show are the instantaneous $V_{\rm SW}$, E_{kl}, and $P_{\rm dyn}$, and the 60-minute averaged IMF B_Z. For all driving parameters shown in Figure 3.3, there is a substantial increase in the 0.3 keV median electron flux between the weakest driving and the strong driving criteria. The increase is predominately in the region from 22–09 MLT and at all radial distances >4 $\rm R_E$. Deviations from this trend are for $V_{\rm SW}$, where the flux *decreases* for $V_{\rm SW}$ >400$\rm km \cdot s^{-1}$ at >8 $\rm R_E$ on the nightside. Recall that this region is where we

imposed our plasma $\beta > 1$ criterion, so that we are seeing a general decrease in near-Earth plasma sheet electron flux at the 0.3 keV energy during elevated $V_{\rm SW}$ ($> 400\,{\rm km}\cdot{\rm s}^{-1}$). Only slight driving by $V_{\rm SW}$, IMF B_Z, and $P_{\rm dyn}$ are required to substantially change the median flux values of 0.3 keV electron flux. However, the flux does not substantially change for a slight increase in E_{kl}.

Figure 3.4 has the same format as Figure 3.3, except we are showing the median values for 2 keV electron flux. The 2 keV electron flux also shows a decrease in the near-Earth plasma sheet for increasing $V_{\rm SW}$. For the other driving parameters—E_{kl}, IMF B_Z, and $P_{\rm dyn}$—substantial median flux increases are only seen during strong driving, compared to weak driving.

Similar to the 0.3 and 2 keV energies, the 12 keV median electron flux (Figure 3.5) shows substantial increases with stronger driving conditions for 18–09 MLT and at radial distances >4 R_E. Even for slightly elevated driving levels (middle column), there are noticeably higher levels of median flux for $V_{\rm SW}$, IMF B_Z, and $P_{\rm dyn}$. Like with 0.3 keV and 2 keV electrons, there is little response in 12 keV electrons from slightly increasing E_{kl}. Still, for all driving parameters (including E_{kl}), the strongest driving (right column) compels a large increase in the median values of 12 keV electron flux.

Solar wind and IMF driving of the fourth energy, 52 keV, is shown in Figure 3.6. Noticeable in all panels in Figure 3.6 are the higher flux levels between 2–3 R_E and between 4–6 R_E at all MLT, which coincide with the locations in the GSM XY-plane of the inner and outer radiation belts, respectively. Although we do see elevated 52 keV median fluxes for strong driving, the increases in flux are mainly restricted to the outer radiation belt region. This is especially noticeable for driving by $V_{\rm SW}$, where even slightly elevated $V_{\rm SW}$ shows an increase in 52 keV electron flux in the outer radiation belt. Yet, for all driving parameters, there is no substantial increase of 52 keV electron flux in the plasma sheet region with increasing driving.

In addition to solar wind and IMF driving, we show the median electron flux during three categories of geomagnetic activity. Although solar wind driving and geomagnetic activity are not mutually exclusive—i.e, with stronger driving, we see elevated levels of geomagnetic activity—it is useful to relate the average flux of electrons with geomagnetic activity in order to correlate flux levels with space weather events. In Figures 3.7–3.10, we show the median values of electron flux for low, slightly elevated, and high geomagnetic activity for the four energies of 0.3, 2, 12, and 52 keV. Similar to the weak, slight, and strong solar wind driving conditions, there are elevated flux levels for increasing geomagnetic activity. Noticeably, the electron flux at 12 keV in the plasma sheet region shows higher increases with increasing geomagnetic activity than does 0.3 keV, 2 keV, or 52 keV electrons.

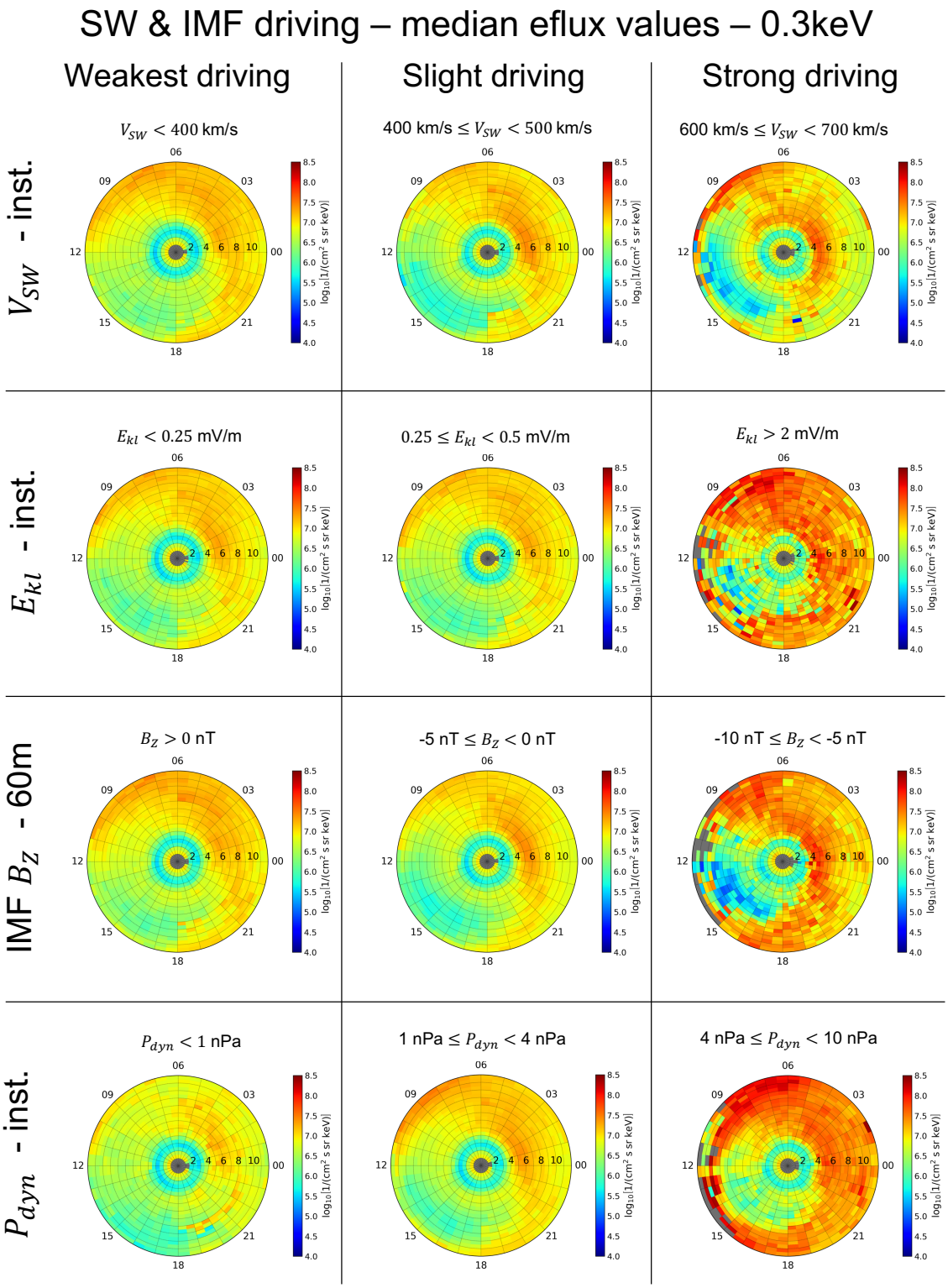

Figure 3.3: The median electron flux at 0.3 keV for weakest, slight, and strong solar wind and IMF driving parameter ranges.

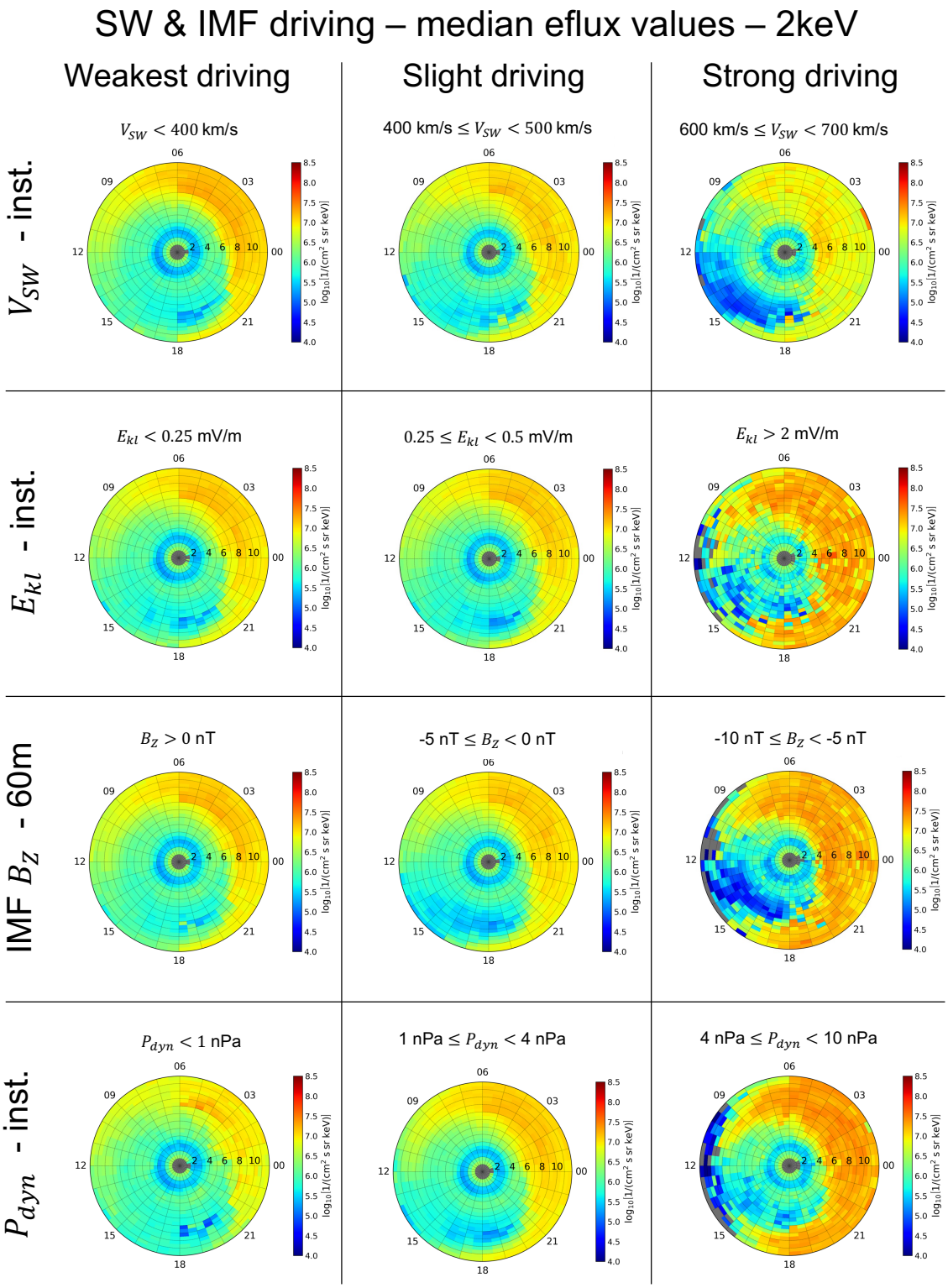

Figure 3.4: The median electron flux at 2 keV for weakest, slight, and strong solar wind and IMF driving parameter ranges.

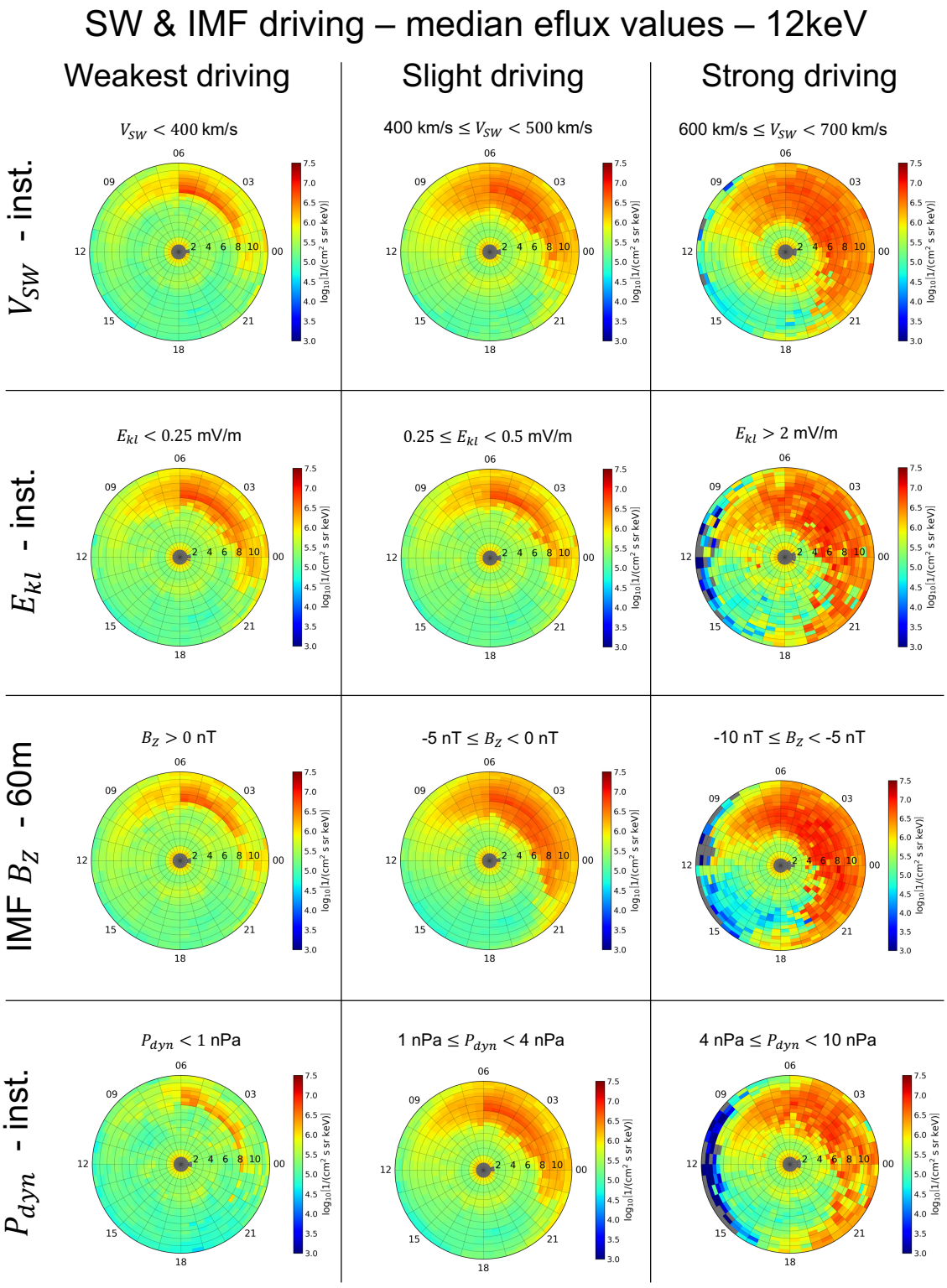

Figure 3.5: The median electron flux at 12 keV for weakest, slight, and strong solar wind and IMF driving parameter ranges.

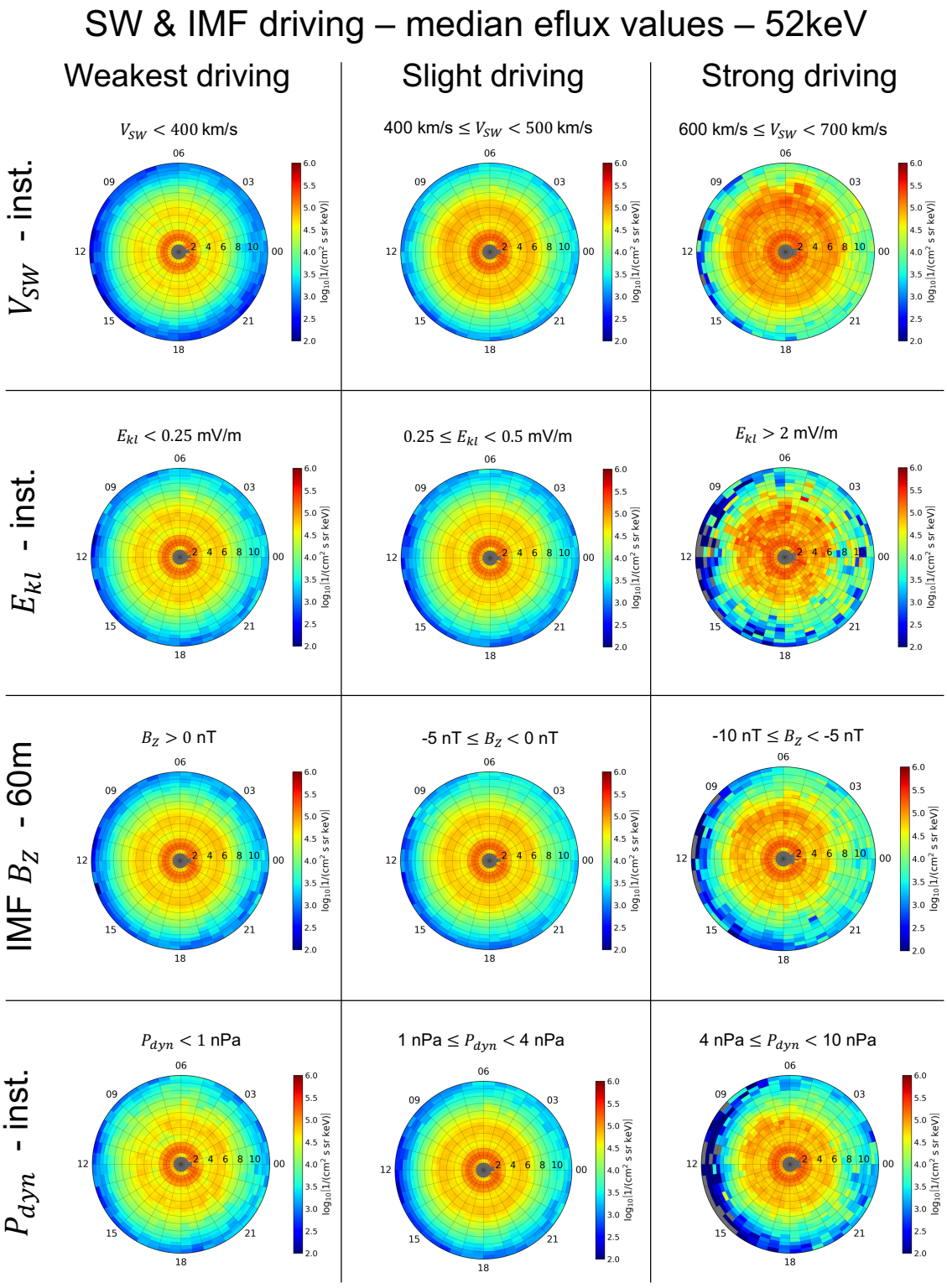

Figure 3.6: The median electron flux at 52 keV for weakest, slight, and strong solar wind and IMF driving parameter ranges.

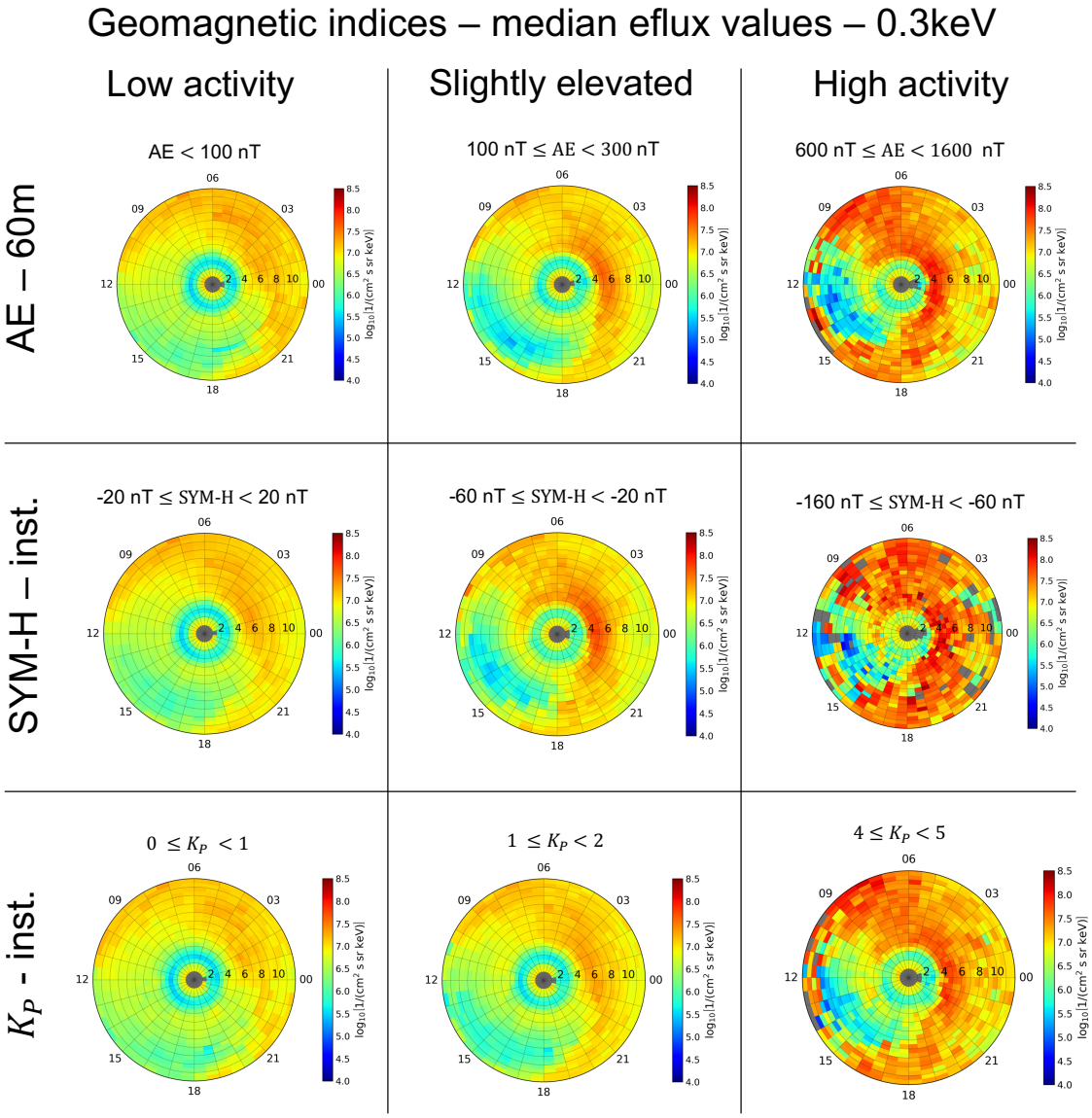

Figure 3.7: The median electron flux at 0.3 keV for low, slightly elevated, and high geomagnetic activity, as indicated by geomagnetic indices.

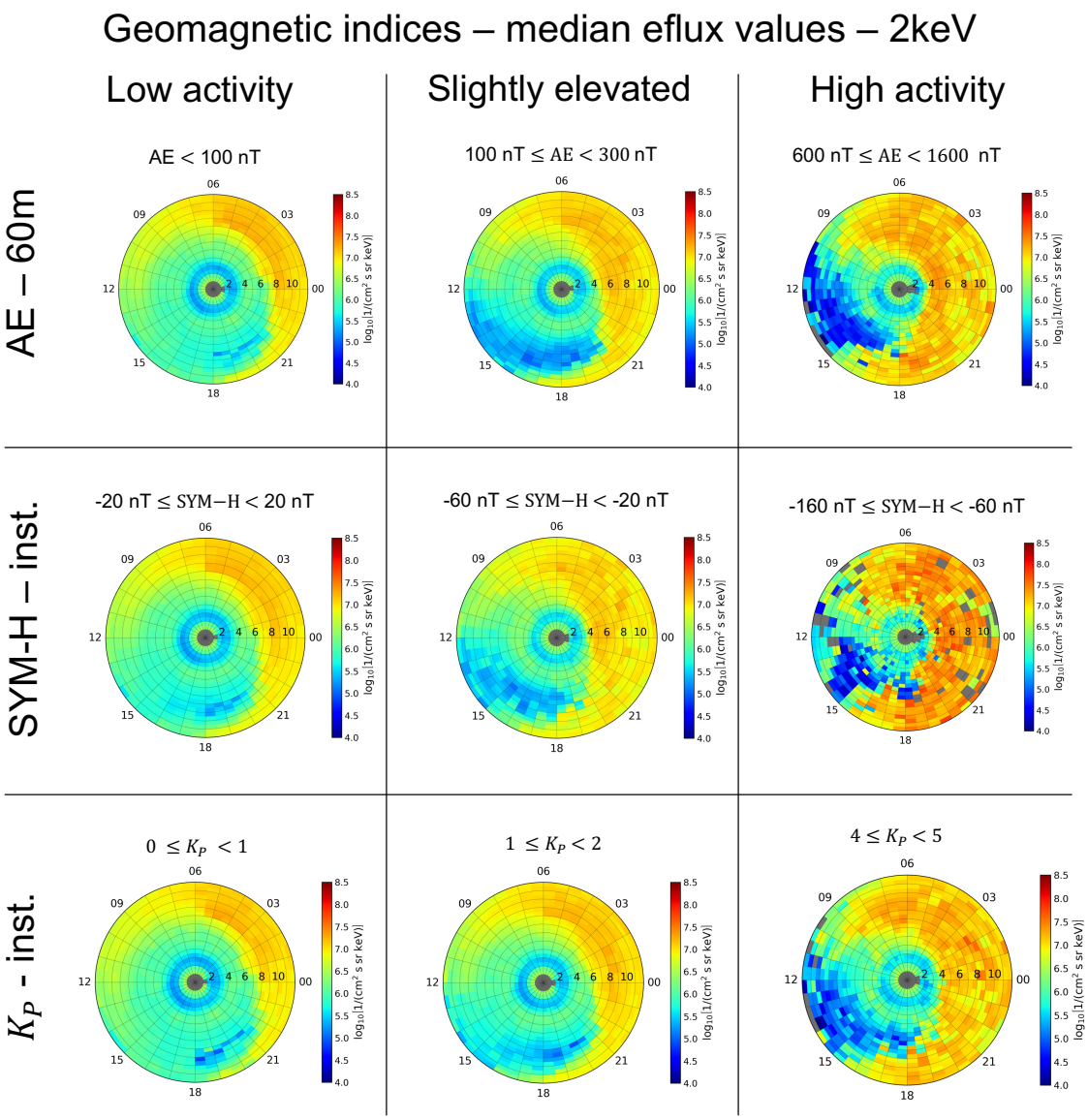

Figure 3.8: The median electron flux at 2 keV for low, slightly elevated, and high geomagnetic activity, as indicated by geomagnetic indices.

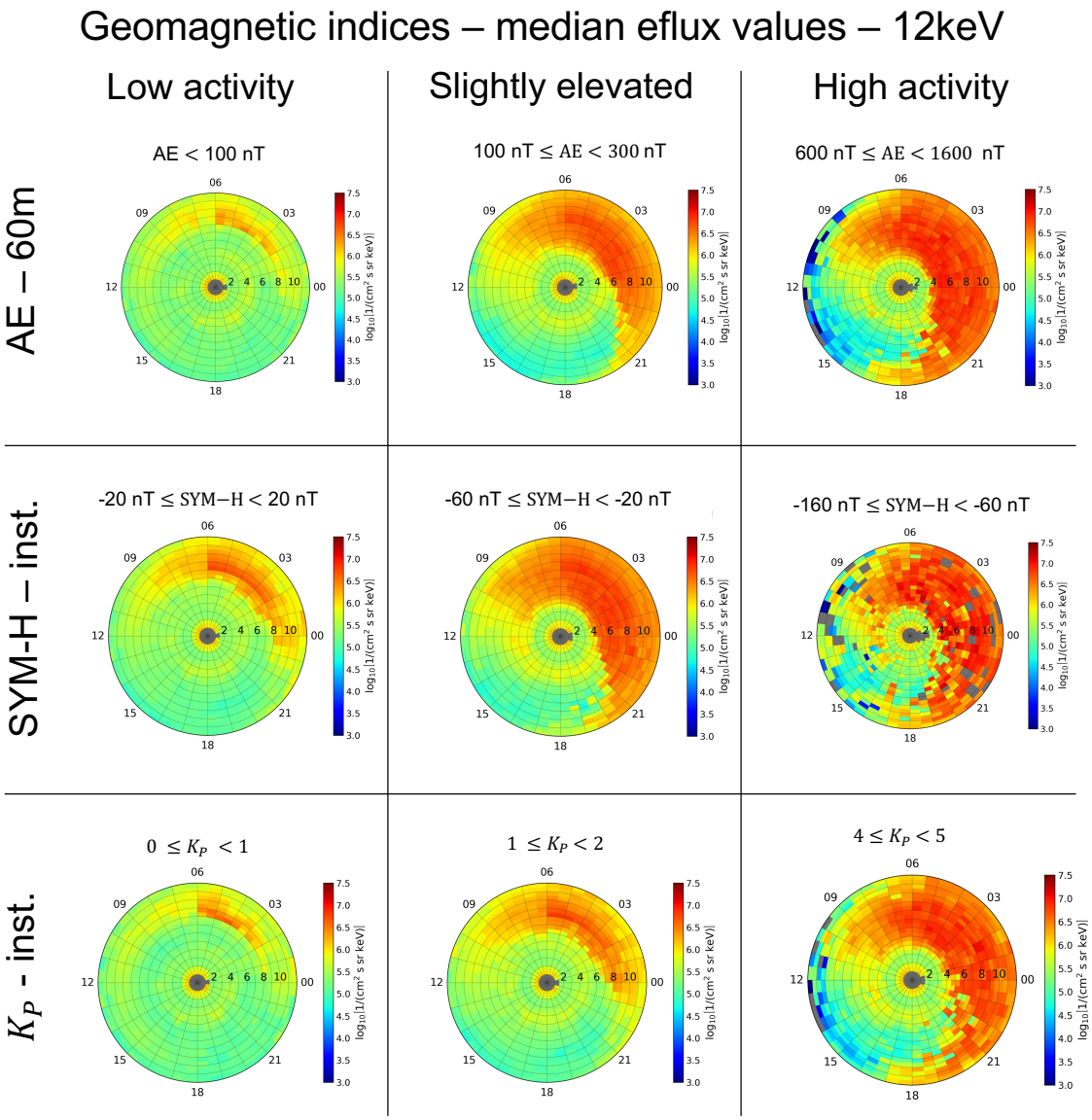

Figure 3.9: The median electron flux at 12 keV for low, slightly elevated, and high geomagnetic activity, as indicated by geomagnetic indices.

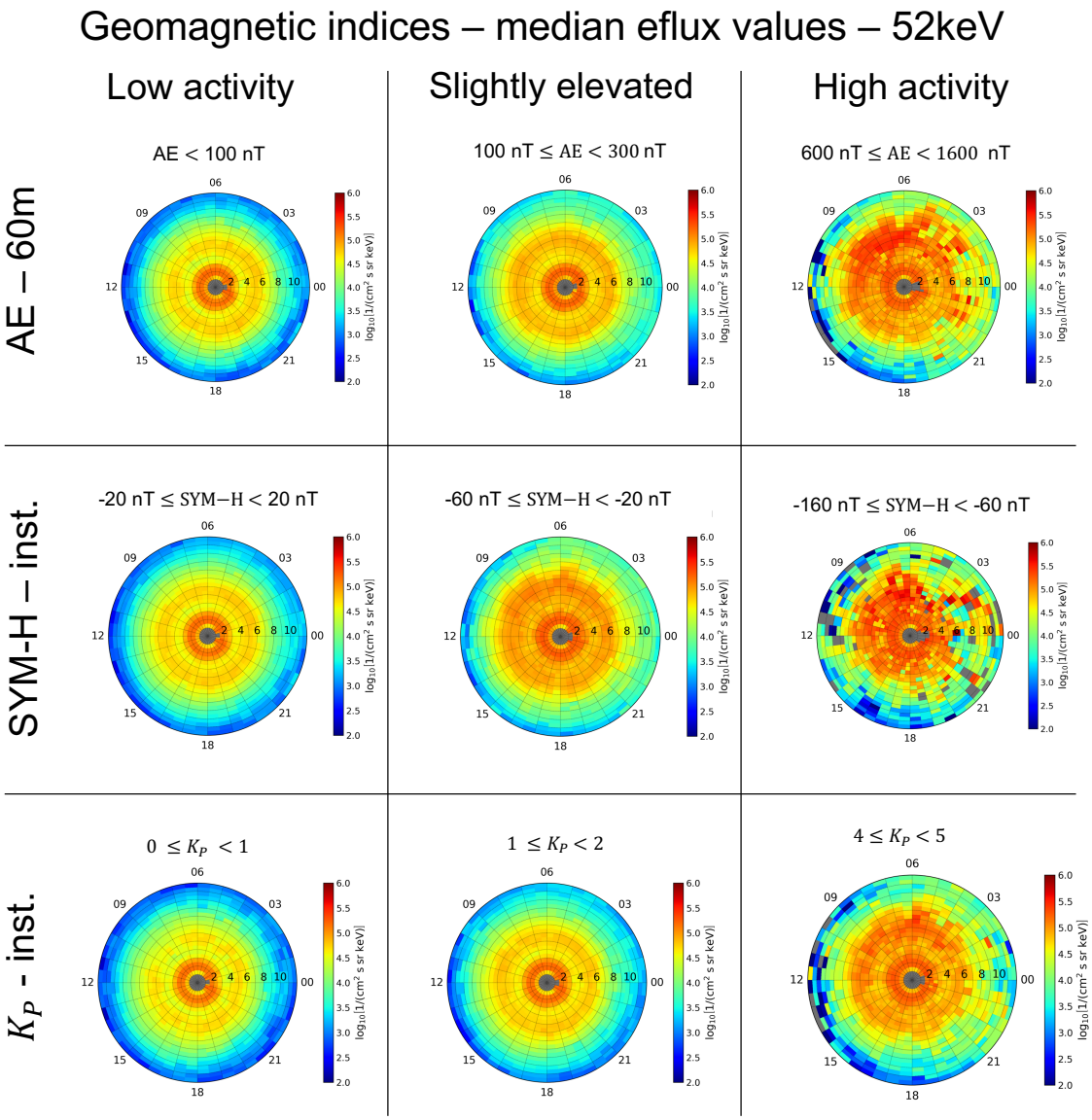

Figure 3.10: The median electron flux at 52 keV for low, slightly elevated, and high geomagnetic activity, as indicated by geomagnetic indices.

3.3.2 Distance Subsets

We create distance subsets by taking all the THEMIS survey data for a fixed radial distance range. Then, we also bin the flux data by MLT and solar wind, IMF, or geomagnetic index parameter. Shown in Figure 3.11 is an example of a distance subset, from 6.5–7.0 R_E using the solar wind flow speed as the binning parameter. The vertical bins are 25 $\mathrm{km \cdot s^{-1}}$ and the horizontal bins are 0.5 MLT. The color in each bin represents the median flux value (in $\log_{10}(1/[\mathrm{cm^2\ s\ sr\ keV}])$) for that bin for energy $\sim$12 keV from whenever the THEMIS observations were between 6.5 and 7.0 R_E. Figure 3.12 shows the number of observations in each bin from Figure 3.11. Grey color indicates that there were no observations in that bin. Like with the radial plots, the number of observations decreases with decreasing occurrence rate of the parameter. For example, there are few times when V_{SW} >700 $\mathrm{km \cdot s^{-1}}$ *and* the THEMIS spacecraft happened to be between 6.5–7 R_E. Consequently, even over 12 years, we have very few (on the order of ten) samples for this combination of criteria. Nevertheless, there are generally sufficient numbers (100 to $\geq$1000) of samples in each bin for most parameter and distance subset combinations.

We show the changes by radial distance of the MLT, solar wind/IMF driving, and geomagnetic activity relationships with the electron flux at four representative energies—0.3, 2, 12, and 52 keV—in Figures 3.13–3.16. In each figure, there are three radial distance ranges at 6.5–7 R_E, 8.5–9 R_E, and 10.5–11 R_E shown along the columns. Along each row is a solar wind, IMF, or geomagnetic index parameter. Parameters appended with '-inst.' indicate we are showing the parameter value at the instantaneous time as the flux observations. In these figures, the IMF B_Z values are the averaged values of the 60-minutes preceding the flux observations.

3.4 Discussion & Conclusion

We have shown the climatic, median flux of electrons in near-Earth space (from 2–12 R_E at all MLT) for four representative energies during various solar wind driving and geomagnetic activity levels. The four energies that we have chosen to highlight—0.3, 2, 12, and 52 kev—represent typical plasma sheet electrons that are in the near-subthermal, thermal, near-superthermal, and superthermal populations, respectively. They all have some similar, and some dissimilar, responses to solar wind driving; and, they have similar and dissimilar relationships with geomagnetic indices.

Recall that in Figures 3.3–3.6 the spatial region between 8–12 R_E and 18–24–06 MLT includes only data when the plasma $\beta > 1$, which indicates a higher likelihood that the data were taken from within the plasma sheet (e.g., Baumjohann et al., 1989). Noticeably, there are increased levels of median electron flux during periods of strong solar wind and IMF driving. This is seen clearly, for example, with all four energies during strong driving by the Kan and Lee reconnection electric

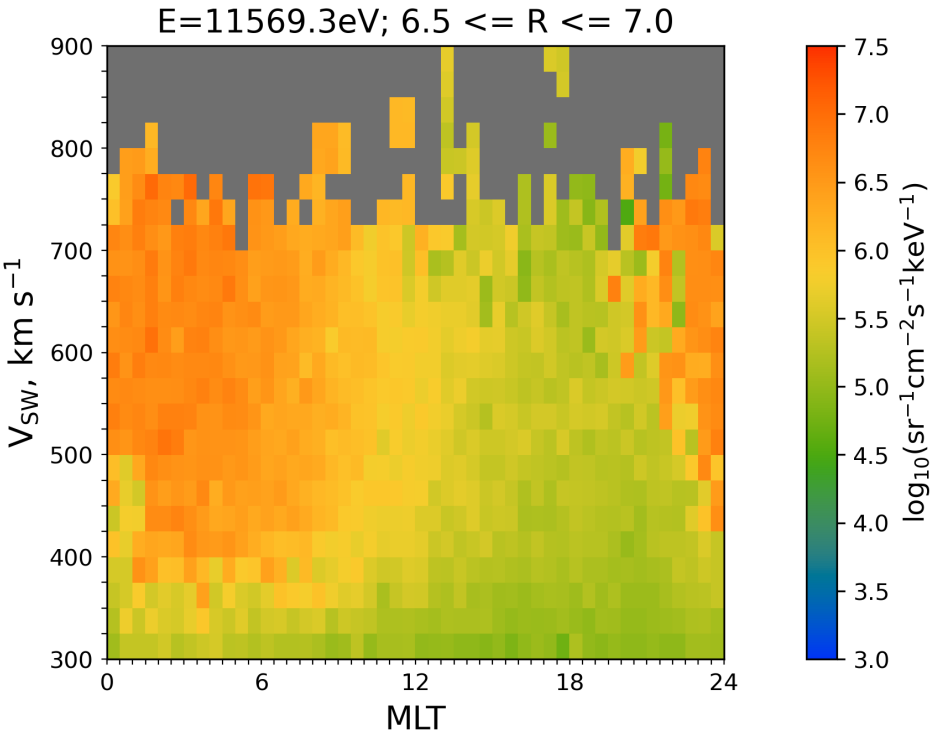

Figure 3.11: Median electron flux values binned by MLT and solar wind flow speed at a radial distance of 6.5 $R_E \leq R \leq 7$ R_E. The color represents the median flux value at $\sim$12 keV energy observed in each bin; grey indicates no observations.

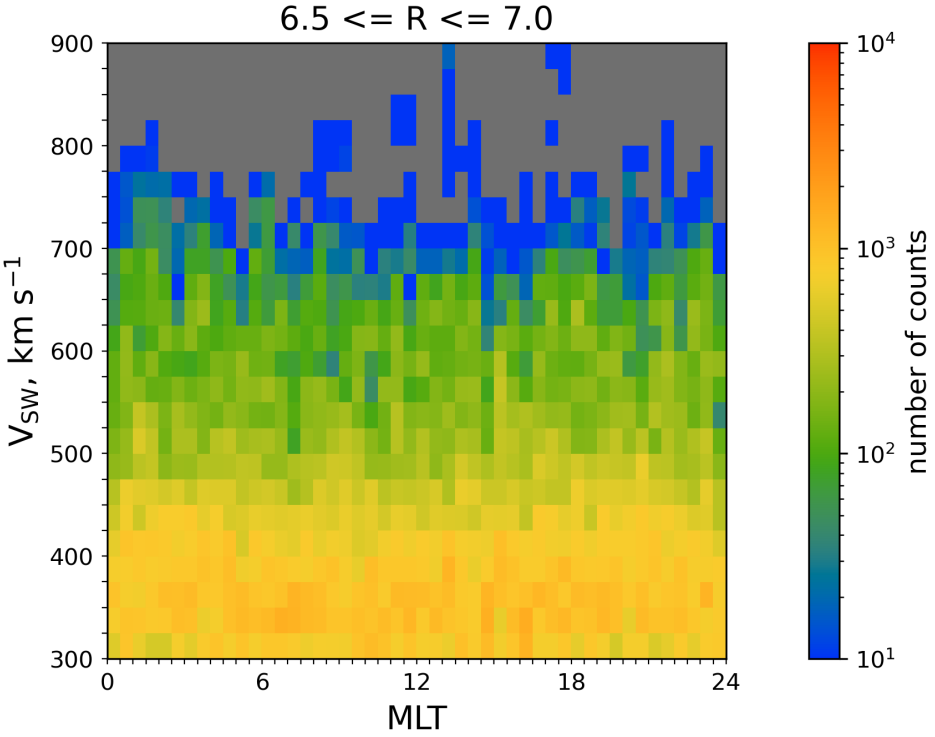

Figure 3.12: The number of observations in each bin of Figure 3.11. Grey color indicates there were no observations.

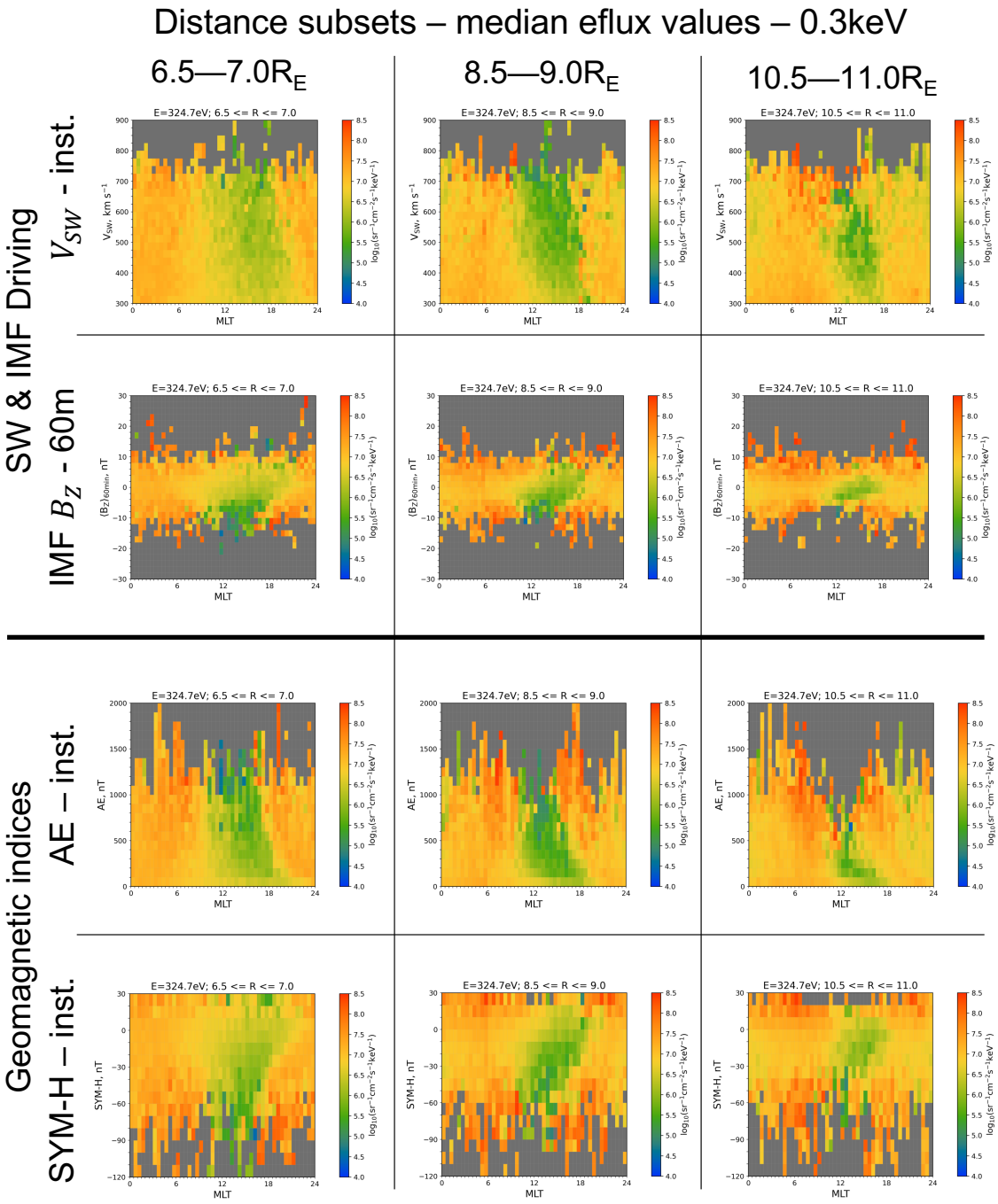

Figure 3.13: The median electron flux for 0.3 keV at three distance ranges for solar wind and IMF driving levels and during different geomagnetic activity levels.

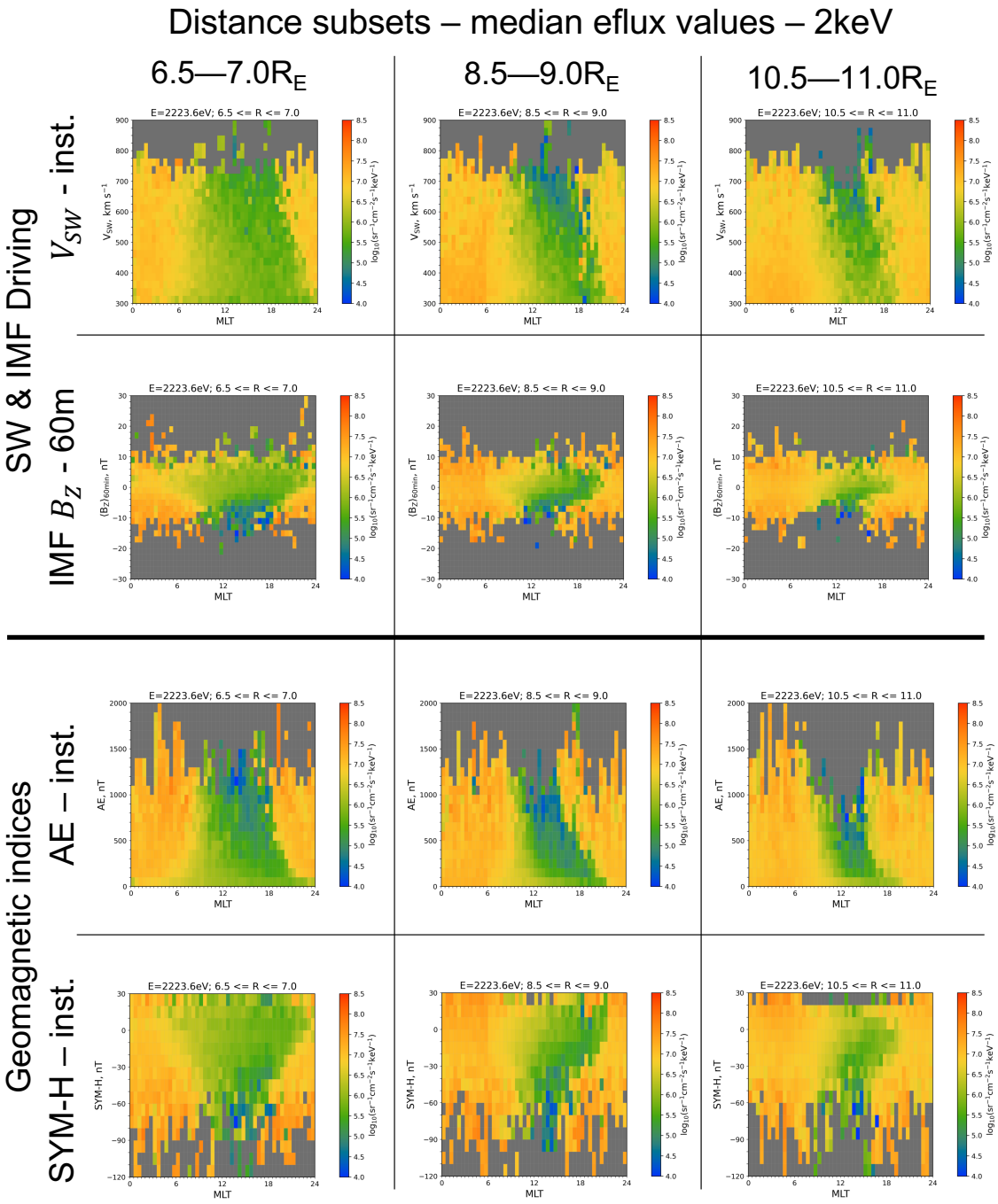

Figure 3.14: The median electron flux for 2 keV at three distance ranges for solar wind and IMF driving levels and during different geomagnetic activity levels.

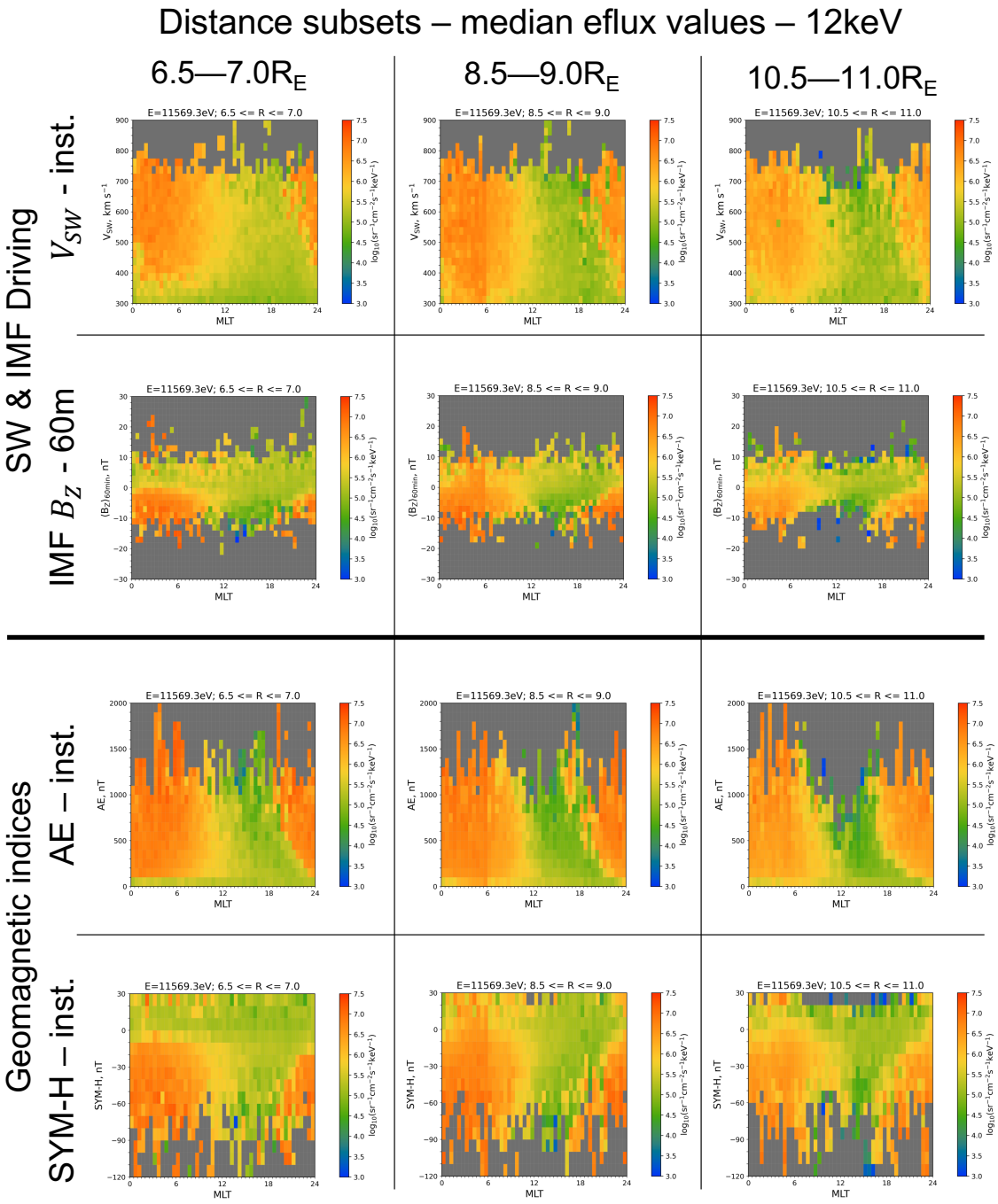

Figure 3.15: The median electron flux for 12 keV at three distance ranges for solar wind and IMF driving levels and during different geomagnetic activity levels.

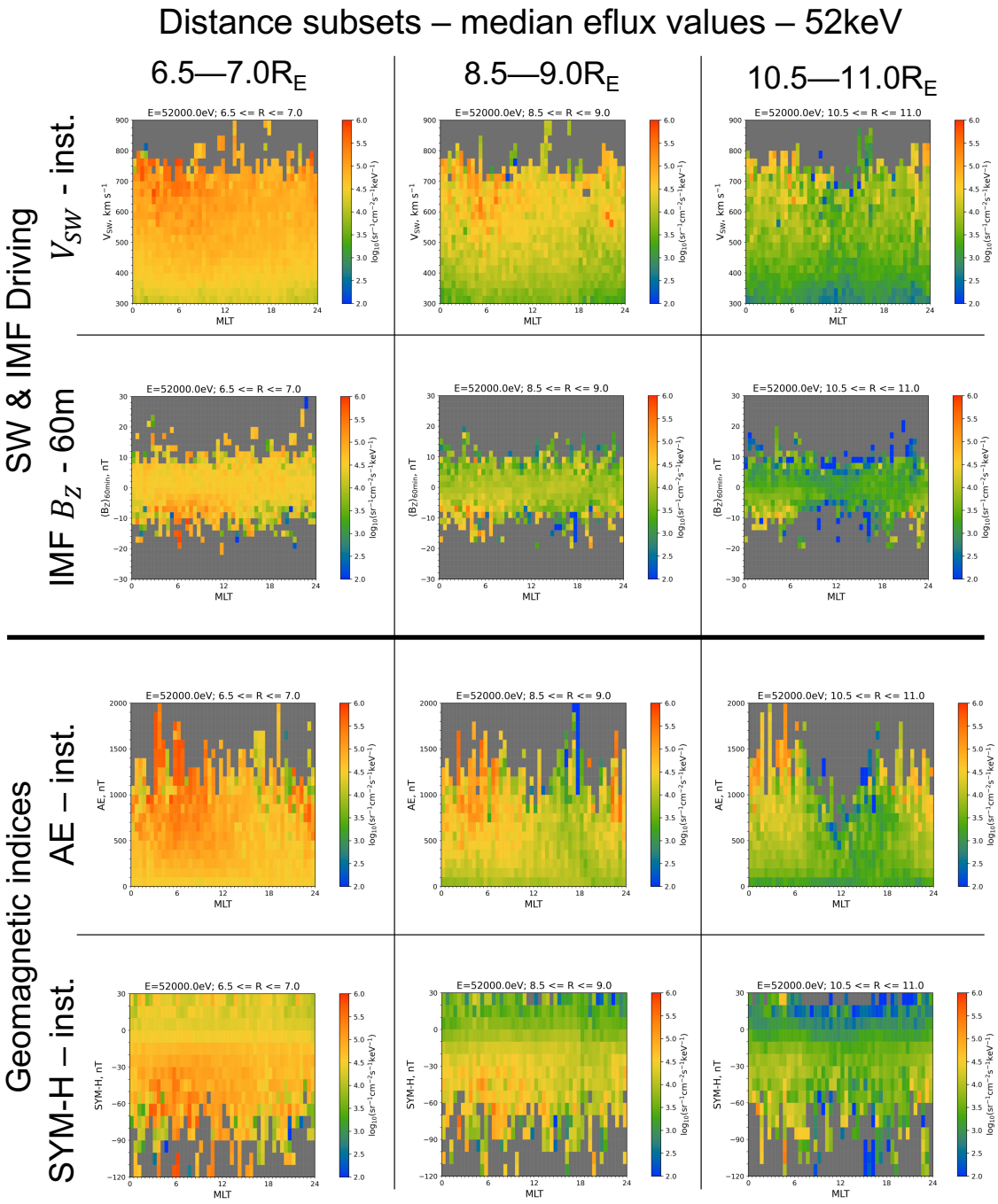

Figure 3.16: The median electron flux for 52 keV at three distance ranges for solar wind and IMF driving levels and during different geomagnetic activity levels.

field (E_{kl} >2 $\mathrm{mV \cdot m^{-1}}$). However, *where* in near-Earth space the flux increase is occurring varies across the four different energies.

3.4.1 Sub-thermal (0.3 keV) Flux Responses

For 0.3 keV electrons (Figures 3.3 and 3.13), the response to solar wind driving depends on the type of driving parameter. When 600 $\mathrm{km \cdot s^{-1}} \leq V_{\mathrm{SW}} <$ 700 $\mathrm{km \cdot s^{-1}}$, the median flux of 0.3 keV electrons is increased but mainly only between 4–6 $\mathrm{R_E}$ and between ∼19–00–08 MLT. In our $\beta > 1$ region, the median 0.3 keV fluxes show a decrease during strong V_{SW}. For the E_{kl}, IMF B_Z, and P_{dyn} parameters, there is a much stronger response of 0.3 keV electrons to stronger driving than for V_{SW}.

In Figures 3.3 and 3.13 it is clear that the flux follows a MLT dependence, where we see lower flux levels between 12–18 MLT during weak and slight solar wind driving and during low and slightly elevated geomagnetic activity. For strong solar wind driving and high geomagnetic activity, the median flux of 0.3 keV electrons intensifies at 12–18 MLT at radial distances >10 $\mathrm{R_E}$. The 60-minute averaged IMF B_Z has some effect on the median flux of 0.3 keV electrons; however, even with strongly sustained southward IMF, the flux of 0.3 keV electron between 12–18 MLT remains low—except at radial distances >9 $\mathrm{R_E}$, where it increases.

3.4.2 Thermal (2 keV) Flux Responses

The trend of increasing V_{SW} resulting in a decrease of plasma sheet electron flux continues for the 2 keV electrons (see Figure 3.4). We again see an increase in 4–6 $\mathrm{R_E}$ electron flux during strong V_{SW} for MLT centered around midnight. Like with the 0.3 keV electrons, the 2 keV electrons continue to show markedly higher median flux levels at >4 $\mathrm{R_E}$ and ∼18–00–09 MLT during strong driving of E_{kl}, IMF B_Z, and P_{dyn} parameters.

The 2 keV median flux levels, similar to the 0.3 keV electrons, show a substantial response to strongly sustained, 60-minute averaged IMF B_Z. However, the increase in flux is more spatially limited. For 2 keV electrons, the increase in flux from IMF B_Z is seen at ∼17–00–09 MLT.

A feature not seen for other energies is the dayside changes in 2 keV median flux with strong solar wind driving and with high geomagnetic activity. There is a substantial decrease in median 2 keV electron flux in the 12–18 MLT sector, especially at 6–9 $\mathrm{R_E}$ compared to weak driving and low activity.

3.4.3 Near-superthermal (12 keV) Flux Responses

Moving into the near-superthermal range of plasma sheet electrons (Figure 3.5), we see that V_{SW} is a strong driver of plasma sheet 12 keV electron flux. From ∼22–00–08 MLT and >8 $\mathrm{R_E}$, the median 12 keV electron flux increases by 1–2 orders of magnitude during strong V_{SW} compared to weak V_{SW}. This is true also for the median 12 keV electron flux with E_{kl}, IMF B_Z, and P_{dyn} drivers.

A consistent feature in Figures 3.5 and 3.15 is that the median flux of 12 keV electrons increases by about an order of magnitude at MLT 00–12 when the AE index increases from <100 nT to >100 nT and when SYM-H decreases from ~ 10 nT to -10 nT. Evidently, there only needs to be a small amount of geomagnetic activity to have significantly elevated ∼12 keV electron flux from 4 $\mathrm{R_E}$ to at least 12 $\mathrm{R_E}$ (the largest radial distance covered in our THEMIS survey).

3.4.4 Superthermal (52 keV) Flux Responses

Contrasting from the lower energies, the median flux of 52 keV electrons shows no MLT dependence (Figure 3.6). There is a consistent band of higher flux between 4–6 $\mathrm{R_E}$ at all MLT and during all solar wind and IMF driving conditions. Clearly, there is an increase in the overall flux as the driving increases from weak to strong, but the region between 4–6 $\mathrm{R_E}$ continues to show a higher median flux than at other radial distances. One exception to this is for strong solar wind driving ($600\mathrm{km \cdot s^{-1}} \leq V_{SW} < 700\mathrm{km \cdot s^{-1}}$) where the distance range of peak flux shifts outward to 5–7 $\mathrm{R_E}$. We interpret this ring of higher median flux as the lowest energy range of trapped electrons that constitute the outer radiation belt. The fact that faster V_{SW} results in a higher median superthermal electron flux in the radiation belt region is consistent with numerous studies examining the much higher energy, relativistic radiation belt electrons and their response to solar wind flow speed (e.g., Paulikas & Blake, 1979; Blake et al., 1997; G. D. Reeves et al., 2011; Denton & Borovsky, 2012; G. Reeves et al., 2013).

3.4.5 Conclusion

The main points of our findings are as follows:

1. With only slight solar wind flow speed driving (i.e., V_{SW} = 400–500 $\mathrm{km \cdot s^{-1}}$), there is a substantial increase in the near-superthermal to superthermal (12–52 keV) electron flux within the near-Earth plasma sheet. The average superthermal flux increases with increasing flow speed.

2. The flux of electrons greater than ∼50 keV also increases with increasing V_{SW}; however, not within the plasma sheet, but rather within the outer radiation belt region between 4–7 $\mathrm{R_E}$.

3. With only a small amount of geomagnetic activity (i.e., AE = 100–300 nT), on average there are substantially elevated levels of 12 keV electron flux in the near-Earth plasma sheet at 22–00–06 MLT.

4. There is an MLT dependence of electron flux for lower electron energies ($\leq$12 keV). The MLT dependence vanishes for electrons whose energy is sufficient ($>$50 keV) to complete a drift path around the Earth and become part of the stably trapped population.

3.4.6 Future Steps

There are some steps that we can take to support our findings and seek new findings. These include performing similar analyses but with using more driving parameters and using solar wind-magnetosphere coupling functions as driving parameters. Instead of using only the median flux values, we could take the values of different percentiles, for example, the 25th, 75th, and 90th percentiles of the distribution of flux values for each energy and subset. This would provide more information about the overall average distribution of electrons at different energies and for different driving parameter ranges. We could also determine other characteristics of the distribution, such as the local histogram's skew, kurtosis, or kappa distribution fit parameters, as a function of location and driving parameter. These parameters would reveal changes in the shape of the local distribution, revealing additional physical processes (such as localized acceleration and loss).

We have shown the median flux during subsets by driving parameter and by geomagnetic activity. We can additionally subset our THEMIS electron flux survey by different phases of the solar cycle. We expect to find relationships between these different phases of low-to-high solar activity with low-to-high levels of near-Earth electron flux. We could also conduct a superposed epoch analysis relative to solar wind or geomagnetic index reference markers, sub-setting the data based on its timing relative to the reference feature.

CHAPTER 4

Severe Environments for Spacecraft Surface Charging

The contents of this chapter are published by Ganushkina et al. (2021). This dissertation's author contributed to the manuscript by creating the figures, calculating the data for the tables, drafting the methodology, and assisting with revising of the full document.

4.1 Introduction

In spite of recent engineering and technological advancements since previous analyses of spacecraft anomalies (e.g., Vampola, 1994; H. C. Koons et al., 1999), modern satellites are still subject to environmental effects (e.g., Green et al., 2017). Spacecraft charging causes the most spacecraft anomalies related to the radiation environment (e.g., Lam et al., 2012; Loto'aniu et al., 2015), and it is surface charging in particular that has caused more serious ones (e.g., H. C. Koons et al., 1999; Choi et al., 2011; Matéo-Vélez et al., 2018).

Surface charging is due to low energy plasma and photoelectric currents (for details, see the reviews by e.g., Garrett (1981); Whipple (1981); Mikaelian (2009)). The spacecraft surface potential is a function of the net current to/from the spacecraft surface. The net current consists of currents from (1) photoelectrons from the surface induced by solar photons, (2) electrons and ions of surrounding plasma impinging on the surface, and (3) charged particles emitted from the satellite (e.g., from electron emission induced by primary electrons, from active ion emission). In a balance, a net current is equal to zero. A spacecraft submerged into plasma will assume a floating potential different from the plasma itself. The net current between the surfaces and the plasma will tend to become zero, therefore, the satellite's surface materials will be charged oppositely to the surrounding plasma. The shadowed areas are charged negative. The sunlit areas are charged positive unless some negative barrier of potential (also given by absolute spacecraft potential) imposed by other satellite's surfaces prevent photoelectron to reach the plasma. Even in this case,

however, sunlit surfaces remain less negative than other surfaces. For the conducting surfaces, the potential of the surface is uniform for reaching the equilibrium for zero net current. For insulating materials, this equilibrium can be only on several points on the surface. Surface materials can discharge both into space and/or to structure ground. The resulting electrostatic discharge (ESD), with conducted currents and/or radiated waves, can couple into electronic circuits and subsystems, causing damage. Spacecraft charging is a function of the space environment characteristics, including sunlight/eclipse, solar activity, geomagnetic activity, electron and ion flux magnitude and spectrum.

The electron temperature is considered the most reliable space environment parameter to predict spacecraft charging based on observational (Rubin et al., 1980; Lai & Della-Rose, 2001; Lai & Tautz, 2006) and theoretical (Lai et al., 1983; Hastings & Garrett, 1996) evidence. The spacecraft potential and electron temperature curves show an intercept at a finite temperature. When temperature is below this critical value, spacecraft charging does not occur, it starts only with temperature above it.

Olsen (1983) demonstrated the existence of a threshold energy of 10 keV (kiloelectronVolt) of particle fluxes for the SCATHA (Spacecraft Charging At High Altitudes) spacecraft to charge when a large portion of the ambient electron flux exceeds this energy. A later study by Thomsen et al. (2013) for LANL (Los Alamos National Laboratory) MPA (Magnetospheric Plasma Analyzer) data showed that surface charging will occur when a critical threshold of electron fluxes with energies of 8 keV has been satisfied. Sarno-Smith et al. (2016) analyzed the relationships between 30 eV to 50 keV electron fluxes and spacecraft potential using Van Allen Probes HOPE (Helium Oxygen Proton Electron) and EFW (Electric Field and Waves) data. They found the electron energy flux threshold for 3 keV electrons for intense charging more likely to occur, however, they stated that it is not always the case. In addition, the electron pressure, not the average electron temperature was shown to have stronger connection to spacecraft charging; but, again, this correlation was not always present. In the studies mentioned above, the spacecraft potential was obtained from observations of the "ion line" (e.g., Thomsen et al., 2013) which represents a sharp low-energy cutoff due to the acceleration of ambient ions through the spacecraft potential.

Correlation between spacecraft anomalies and substorm activity was observed in the 1970s on the ATS (Applications Technology Satellite)-5 and -6 and the first two Defense Satellite Communication System-Phase II (DSCS-II) geosynchronous communication satellites using magnetometer data from ground stations near the satellite magnetic footprint (Rosen et al., 1972; Fredricks & Scarf, 1973). DeForest (1972) directly demonstrated that the surface of the ATS-5 spacecraft was charged to large negative potentials (up to -9 kV (kiloVolt) under eclipse conditions), when the spacecraft was in the local morning sector, by $\sim$ 1–10 keV electrons injected from the plasma sheet during substorm-associated events. Farthing et al. (1982) analyzed the ground magnetograms from

Anchorage station in Alaska and found that the substorm activity occurred very closely in time with the anomalies detected at GOES (Geostationary Operational Environmental Satellite) 4 and 5 in the postmidnight sector. Extended analysis of data from ATS-6, GEOS (Geodetic Earth Orbiting Satellite)-2 and SCATHA resulted in the design guidelines (Purvis et al., 1984) for mitigation of the differential charging hazard. Spence et al. (1993) investigated about 100 anomalies that occurred at several high-inclination, high-altitude satellites by comparing their distribution to the known surface charging distributions (i.e. observed an SCATHA spacecraft) and related them to 10–15 keV energetic particle injections from the Earth's magnetotail during substorms.

The satellite anomalies caused by substorm injection depend on local time indicating that they were caused by geomagnetic activity but not by operational or design problems. Numerous studies (e.g., H. C. Koons & Gorney, 1991; Spence et al., 1993; Lanzerotti et al., 1998; Fennell et al., 2001; Gubby & Evans, 2002; Iucci et al., 2006; O'Brien, 2009; Allen, 2010; Choi et al., 2011; Mazur et al., 2012) showed that surface discharges peak at around midnight to dawn in local time with very few occurring on the dayside. That is, the anomalies are the most frequent in the sector of substorm electron injections. For example, Fennell et al. (2001) have analyzed the occurrences of anomalies on HEO (Highly Elliptical Orbit) satellites (Spence et al., 1993) and found that the spatial distribution of the HEO anomalies mapped to the equatorial plane is close to the pattern of substorm-injected electrons. On the contrary, the effects of internal charging should be most prominent on the dayside or should show no local time dependence at all (Mazur & O'Brien, 2012).

At the same time, it is not possible to state that all substorms and, especially, intense ones, will definitely lead to satellite anomalies and that they will be due to surface charging. Small, isolated substorms can be related to the significant changes in the radiation environment which could lead to the surface charging related anomalies (e.g., Grafodatskiy et al., 1987; Matéo-Vélez et al., 2016). Matéo-Vélez et al. (2018) have examined the particle data from the LANL spacecraft and extracted times when the particle environment can be extreme and can result in surface charging conditions. It was shown (see Figure 8 in Matéo-Vélez et al. (2018)) that severe conditions can occur during geomagnetic storms or isolated substorms but the occurrence even of a moderate storm is not necessary. All the identified times (400 of them) with severe particle environments were attributed with the values of Dst (Disturbance storm time) and AE (Auroral Electrojet) indices. Storms were identified by corresponding Dst variations seen as the initial, main and recovery phases but not by the strength of them. Isolated moderate substorms were defined by the AE index from 300 nT to 800 nT, isolated intense substorms–by AE index higher than 800 nT, and small substorms with AE $<$300 nT. Many of the identified events in Matéo-Vélez et al. (2018) were detected during small to moderate substorm activity, and no direct dependence was found on substorm strength. Most events in the Matéo-Vélez et al. (2018) study were observed in the 21–06 MLT (Magnetic Local

Time) sector with very few in the <20 MLT or >07 MLT sectors, which is consistent with previous studies (e.g., Mullen et al., 1986).

Among multiple characteristics of geomagnetic activity, the *Kp* (Planetarische Kennziffer) index has been considered as the main geomagnetic index in the studies relating satellite anomalies with geomagnetic activity in early studies. Rubin and Garrett (1979) discovered the relation of ATS-5 and ATS-6 potential with *Kp*. Farthing et al. (1982) presented the correlation of the anomalies at GOES 4 and 5 spacecraft with the *Kp*. The positive correlation between the SCATHA satellite surface potential monitors (SSPMs) data and the *Kp* index was demonstrated by Mullen et al. (1986) and H. C. Koons and Gorney (1991). Later, Spence et al. (1993) analyzed about 100 anomalies detected at several high-inclination, high-altitude satellites and found that the anomaly occurrence is strongly related to the *Kp* index value. Choi et al. (2011) selected 95 anomalies that occurred at geostationary satellites from 1997 to 2009 and showed the anomaly occurrence rate increased with increase of the *Kp* index. Thomsen et al. (2013) found "an enhanced surface charging probability" at LANL satellites during higher *Kp* values. At the same time, the anomalies included the effects from both surface and internal discharges, which have similar dependence on the *Kp* index (H. C. Koons & Gorney, 1991).

However, no agreement was reached on a linear dependence between the anomalies which might be due to surface charging and the *Kp* value. While O'Brien (2009) stated that anomalies due to surface charging are most probable at *Kp* of 46, Denton and Borovsky (2012) found >500 V spacecraft potentials occurring at relatively low *Kp* values of 2 or 3. O'Brien (2009) used the data of surface charge monitors (Ozkul et al., 2001; H. Koons et al., 2006) on geosynchronous satellites. Denton and Borovsky (2012) derived spacecraft potentials from the LANL particle data.

W. Q. Lohmeyer and Cahoy (2013) analyzed 26 solid-state power amplifier (SSPA) anomalies detected at eight Inmarsat geostationary communications satellites during 1996-2012 and found that 80% of anomalies occurred with *Kp* <3. Mazur et al. (2012) have analyzed statistics on surface charging signatures from a charging plate analyzer (CPA) observed on the Intelsat satellites (H. Koons et al., 2006) at GEO during 1997–2001. Charging potentials from CPA were more straightforward indication of surface charging than obtaining a more complex charging signature from ion spectrograms (as was done in Thomsen et al. (2013)). Mazur et al. (2012) noticed that surface charging occurred during both quiet and active time intervals as seen in *Kp* index. Moreover, they found the influence from the RussellMcPherron effect (Russell & McPherron, 1973) with semiannual variations in the charging signatures, such as, together with *Kp*, the surface charging was more likely to happen during the spring and fall equinoxes (similar to the Matéo-Vélez et al. (2018) study).

Bodeau (2015) questioned the usage of the *Kp* index as an indicator for severe environments to cause surface charging and to induce anomalies due to it. A series of solar array string failures

occurred on three high-power communication satellites (Hoeber et al., 1998) were compared with the *Kp* index and no dependence was found. The conclusion was that "a high *Kp* does not insure significant charging levels, and conversely, significant charging can occur during modest to severe *Kp* index values." Bodeau (2015) examined ground magnetograms and X-ray emissions measured by the Polar spacecraft from the atmosphere in the auroral region near the magnetic footprint of the communication satellites and found that severe substorm activity was detected right before nearly every moment of circuit failure.

Ferguson et al. (2015), while admitting that *Kp* dependence for surface charging seems to be logical, since *Kp* is an indicator of a disturbed magnetosphere, did not find any correlation trend between the LANL negative spacecraft potential and the large *Kp* values from 7 to 9 (see their Figure 38). They presented the electron flux above a minimum energy E_{min} as a charging index for geosynchronous spacecraft in sunlight with E_{min} of 9–15 keV and the threshold for flux above E_{min} to be near 4×10^8 $\mathrm{e^-/cm^2/s}$. The proposed observational charging index was later found to be consistent with the theory in the Huang et al. (2017) study.

While the *Kp* index has been extensively used in attempts to find correlations with surface charging anomalies, other characteristics, such as, the AE (Auroral Electrojet) and Dst (Disturbance storm time) indices and solar wind and IMF (Interplanetary Magnetic Field) parameters, were not. Wrenn and Smith (1996) estimated the probability of surface ESD effects on the MARECS-A satellite launched in 1981 at GEO as dependent on *Kp* and AE indices. They found that the probability to observe the effects from surface ESD increases for *Kp* from 3 to 5 and AE from 200 to 800 nT but decreases for higher magnitudes of *Kp* and AE. This behavior was attributed to the magnetic field at GEO being drastically distorted. W. Lohmeyer and Baker (2012) attempted to relate the Inmarsat anomalies with the Dst index and the solar wind speed and found that at the times of the anomalies, the Dst index did not drop below -40 nT and the solar wind speed varied in the range between 300 and 500 $\mathrm{km \cdot s^{-1}}$ exceeding 600 $\mathrm{km \cdot s^{-1}}$ at only two times (see their Figure 14). The importance of the solar wind speed increase for spacecraft potential was reported in earlier studies (DeForest, 1972; Hastings & Garrett, 1996). Denton and Borovsky (2012) investigated spacecraft potentials at LANL during strong and weak High Speed Streams (HSS). They defined strong events when the solar wind speed is higher than 500 $\mathrm{km \cdot s^{-1}}$ during 5 days but weak events are characterized by the solar wind speed below 400 $\mathrm{km \cdot s^{-1}}$ during 3 days. Denton and Borovsky (2012) found a strong correlation between the average negative spacecraft potential and the solar wind speed. Moreover, the level of the corresponding surface charging was found to be significantly larger for the strong HSSs than for the weak HSSs.

In the present paper, we analyze a database of 400 events developed by Matéo-Vélez et al. (2018) (presented in Section 4.2) which contains the dates and times of the worst-case severe environments for surface charging as observed by LANL satellites during the years of 1990–2005.

The main focus is to find possible relations between the activity parameters and worst-case severe environments for surface charging. Each input in the database was attributed with the corresponding values of geomagnetic activity indices and solar wind and IMF parameters. The dependencies of worst-case severe environments for surface charging and near-simultaneous geomagnetic activity are contained in Section 4.3. It shows peaks in the number of events with corresponding parameter magnitude and range, the highest risk to detect a worst-case severe environment event at the corresponding value of the parameter, and presence of a risk-parameter dependence. Section 4.4 demonstrates the results of a superimposed epoch analysis with the parameter changes in time before the event, relative timing of parameter maximum change and the event detection time moment, and parameter changes after the event. The obtained dependencies are discussed, and the conclusions are drawn in Section 4.5.

4.2 Severe Environment Events from LANL Data

We use the database of 400 total events developed by Matéo-Vélez et al. (2018) that contains the dates and times of the worst-case severe environments for surface charging as observed by LANL satellites during the years of 1990–2005. Matéo-Vélez et al. (2018) have analyzed the particle fluxes from the MPA with energies from 100 eV to 40 keV (Bame et al., 1993), the Synchronous Orbit Particle Analyzer (SOPA) with energies between 50 keV and 1.3 MeV (Belian et al., 1992) and the Energetic Spectra for Particles (ESP) with energies from 1 to several MeV (Meier et al., 1996). Matéo-Vélez et al. (2018) have formulated four different criteria to define severe environments potentially leading to surface charging. 100 worst case events were identified in each criterion with 400 events in total. For a given criterion, each event is among the top 100, 15-minute averaged worst-case severe environments for surface charging defined by that criterion. These four groups of events comprise the main dataset of our study. They also form the basis of on-ground tests of materials under multi-energetic electron beams (Matéo-Vélez et al., 2019).

Among the four criteria, one criterion is based on the measured spacecraft potential and three criteria are based on integral electron fluxes. The spacecraft potential criterion deals with the average spectra related to large negative potentials over long periods of time. It was called PG5k, since the longest events with a Potential Greater than 5 kV (in absolute) were considered. The criterion defines 100 longest events with Potential Grater than 5 kV (in absolute). It should be stressed that the top 100 events are selected on the basis of duration of the potential drop rather than the potential drop peak value. This means that the events with stronger charging but having shorter duration are dismissed by this criterion. On the other hand, the threshold values of -5 kV used for the event definition obviously represents extreme charging.

Eclipse or sunlit conditions play a very important role in PG5k criterion. Photoemission is gen-

erally the most important charging current, which is able to counterbalance a large fraction of the negative current imposed by electron fluxes during substorms, depending on the incidence angle of photons on the satellite's surfaces. In the present study, 87 out of the 100 PG5k worst-cases are in eclipse. Therefore, it can be considered that PG5k worst-case environments are representative of the most severe charging events occurring during eclipse. The dependence of these events on plasma and geomagnetic conditions is very interesting issue because they are less subject to the uncertainties linked to the sunlight incidence on satellite surfaces.

For criteria based on fluxes, the electron fluxes have been averaged over 15 minutes, since it is necessary for severe conditions to be present for a few minutes for differential charging to occur at geosynchronous orbit. Matéo-Vélez et al. (2018) used 15 minutes as an approximate duration to bring significant differential charging (hundreds of volts) on dielectrics of about 25 to 100 μm thickness in a GEO-like environment.

One criterion concerns high fluxes at low energies together with a Low Flux at High Energy (LFHE). It is a combination of both high fluxes below 50 keV and low fluxes above 200 keV which is related to surface charging. Another criterion concerns the Highest Fluxes at All Energies (HFAE). It combines high fluxes both below 50 keV and above 200 keV, since they are related to charge deposited both at the surface and in the bulk of covering insulators. The last criterion is about the highest Fluxes of electrons at Energies above 10 keV (FE10k). The most severe electron spectrum was selected each month on each spacecraft to avoid duplication if the same events were detected by several spacecraft. The list of most severe satellite-month spectra was then classified within top 100 events, one for each criterion, resulting in 400 events in total. A potential below -300 V was reached for 80 FE10k worst-case events out of 100, 60 for HFAE and 40 for LFHE. It should be stressed here that the worst-case environments criteria were defined to address both absolute negative potentials and large differential potential at the same time. This is generally speaking a difficult task because LANL data can be used to compute absolute potential but not differential. Therefore, Matéo-Vélez et al. (2016) proposed different ways to define a worst-case depending on the relative importance of low and high energy electron fluxes. The best correlation with absolute charging was obtained with PG5k, of course, by definition, and with FE10k. However, LFHE and HFAE should not be dismissed because, first, a large fraction of them was associated with potential below -100 V, and, second, they can theoretically generate high levels of differential charging levels due to specific interaction of electrons with insulators. This is why all these 4 criteria are relevant for the present study with the goal to assess risks of surface charging leading possibly to electrostatic discharges and, in the end, to spacecraft anomalies.

Each event in all 400 events was attributed with the corresponding values of *Kp*, AE, AL (Auroral Lower), and SYM-H (symmetric disturbance magnetic field in H-component) indices and solar wind and IMF parameters, namely, IMF B_Z, solar wind speed, proton number den-

sity, and derived electric field E_y and $< VB_s >$. For solar wind and IMF data, OMNIWeb (http://omniweb.gsfc.nasa.gov/) was used, so, E_y was obtained directly from there and $< VB_s >$ was computed using solar wind speed and B_s, defined as $B_s = |B_Z|$, if B_Z is negative and $B_s = 0$ otherwise. Geomagnetic indices were obtained from the World Data Center for Geomagnetism, Kyoto (http://wdc.kugi.kyoto-u.ac.jp/wdc/Sec3.html). The dependencies on solar wind and IMF parameters and geomagnetic indices of the events in each criterion were then studied.

4.3 Worst-Case Severe Environments for Surface Charging and Current Geomagnetic Activity

4.3.1 Dependence on Geomagnetic Indices

4.3.1.1 *Kp* Index

We start with dependencies on geomagnetic indices. The four top panels in Figure 4.1a present the histograms of top 100 events with worst-case severe environments for surface charging as dependent on the *Kp* index observed during these events. These severe environment events in 15-minute intervals were identified by Matéo-Vélez et al. (2018) following the criteria PG5k (top panel, purple), LFHE (second panel, green), HFAE (third panel, red), and FE10k (forth panel, blue). The *Kp* index occurrence rate (orange line) for the entire period of 1990–2005 (irrespective of the environment condition) is shown in the bottom panel. The *Kp* binning was done so that the [0,1) bin includes *Kp* values of 0, $0+$, and $1-$, the [1, 2) bin includes *Kp*=1, $1+$, and $2-$, and so on, and the [8, 9] bin includes *Kp*=8, $8+$, $9-$, and 9.

Several features can be noticed in the plotted histograms:

(1) The histograms showing the number of severe environment events in all four criteria do not coincide with the 16 years occurrence rate of the *Kp* index (orange line in the bottom panel). The highest occurrence rate for the observed *Kp* is from 1 to 3. If they would have coincided, for each *Kp* value, the probability of the presence of a severe environment would be the same, independent of *Kp*. Since this is not the case, the *Kp* value can be considered as an indicator for an event to happen.

(2) The PG5k histogram, which corresponds to the spacecraft potential criterion, has its peak at *Kp* = 3–4 (39 events), whereas all the histograms for criteria based on electron fluxes show maximum values at *Kp* = 4–5 (25–30 events), except for HFAE criterion which has a wider peak at *Kp* = 3–5.

(3) There are more PG5k events at smaller *Kp* (6 events at *Kp* = 1–2 and 20 events at *Kp* = 2–3) as compared to flux based events with negligible number at *Kp* = 1–2 and 5–11 events at

Table 4.1: Total numbers of 15 minute averages of the LANL observations in 20 to 08 MLT sector for different years from all LANL spacecraft used in Matéo-Vélez et al. (2018).

Year	1990	1991	1992	1993	1994	1995	1996	1997
# observations	13786	26044	34745	32117	26044	33284	42311	43627
Year	1998	1999	2000	2001	2002	2003	2004	2005
# observations	44925	53001	43439	39115	65062	69113	64823	53185

Kp = 2–3). (4) More events with flux based criteria occurred at higher *Kp* (> 5) than those of spacecraft potential based criterion: there were ≤ 6 PG5k events in each *Kp* bin for *Kp* > 5, whereas 18 LFHE and 20 FE10k events were detected at *Kp* = 5–7 and 19 HFAE events at *Kp* = 5–6. For large *Kp* > 7, only the FE10k criterion showed 16 (*Kp* = 7–8) and 8 (*Kp* = 8–9) events. Obviously, the *Kp*-dependent histograms for severe environment events do not reveal fully the risk to encounter the severe environment for given *Kp*: statistical decrease of the occurrence rate of higher *Kp* values (see bottom panel in Figure 4.1a) should be taken into account. In other words, the decrease in histograms for high *Kp* values during severe environment events may just reflect the lower probability of high *Kp* occurrence but not a lower risk of severe environment.

To address this issue, we developed a specific normalization procedure. The idea is to normalize the number of severe environment events for each *Kp* bin by the total number of LANL observations corresponding to this *Kp* bin. The only data analyzed in the present paper are the times and locations of 400 worst-case events, not the full, original LANL dataset (it was not freely available). What was available is the total numbers of 15 minute averages of the LANL observations in 20 to 08 MLT sector for different years used in Matéo-Vélez et al. (2018) given in Table 4.1. These numbers include all observations from all operating LANL spacecraft. The choice of 20 to 08 MLT sector is due to the finding that all of the worst-case severe environments were detected at local times from 20 to 08 MLT (see Figure 6b of Matéo-Vélez et al. (2018)). Thus, we calculate the chance to encounter the severe environment in the top 100 only for this MLT sector. The total number of LANL observations in a given *Kp* bin can be estimated by multiplying these numbers for the normalized *Kp* occurrence for given bin and year. In more details, the normalization algorithm can be explained as follows.

For a particular year, the number of events with detected top 100 worst-case severe environments for one particular *Kp* bin for all operating LANL spacecraft is $N_{eventsLANL}$. Let the total number of LANL 15 minute observations in 20–08 MLT sector be N_{LANL} (Table 4.1). To estimate the number of available LANL 15 minute observations for the particular *Kp* bin, the total number N_{LANL} must be multiplied by the occurrence rate $N_{Kp}norm$ (Figure 4.1a, bottom panel) of the *Kp* index for this bin for this year. $N_{Kp}norm$ is computed as $N_{Kp}/N_{Kp}all$, where N_{Kp} is the number of *Kp* records in a given *Kp* bin (at a given *Kp* value) for this year (irrespective of what LANL ob-

serves, just using the *Kp* index distribution), and $N_{Kp}all$ is the total number of *Kp* records (number of 3 hour intervals in a year).

Now, for a given year, the normalized occurrence rate for an event in the list of top 100 severe environment events in a given *Kp* bin can be estimated as the number of severe events for a given *Kp* bin divided by the estimate for the number of all LANL observations for a given *Kp* bin:

$$Normalized\ occurrence\ rate = \frac{N_{eventsLANL}}{N_{Kp}norm \cdot N_{LANL}} \cdot 100\%. \tag{4.1}$$

To get the average risk (normalized occurrence rate), we sum over all years:

$$< Normalized\ occurrence\ rate >= \frac{\sum_{i=1990}^{2005} N_{eventsLANL_i}}{\sum_{i=1990}^{2005} N_{Kp}norm_i \cdot N_{LANL_i}} \cdot 100\%. \tag{4.2}$$

It should noted that this method of normalization does not perfectly suits to PG5k criterion events because almost all these events occurred in eclipse. This means that being in eclipse is a necessary condition to have such an event. Therefore, PG5k events should be normalized by the total time the spacecraft spends in eclipse for a given *Kp* bin. Since the eclipse conditions for GEO occur at around the equinoxes and the geomagnetic activity has semiannual variation (Russel-McPherron effect) (Russell & McPherron, 1973), it is impossible to do such normalization without the orbital information. For this reason, we estimate the risk to have PG5k event using the same method as for other criteria and keeping in mind this specific feature of PG5k events (duration of charging but not peak value). It should be emphasized that we define the risk as a chance to have one of 100 top events (but not to exceed certain threshold). For this reason, the PG5k risk values can be compared to the ones of other criteria.

The normalized severe environment occurrence rate is shown by black dots in the four top panels of Figure 4.1a. It is important to note that the normalized occurrence rate described above is different from that of shown in the bottom panel of Figure 4.1a. The black dots can be considered as an indicator of a risk to detect a top 100 worst-case severe environment event in a 15 min window for a given *Kp* bin.

The uncertainties for each normalized severe environment occurrence rate (black dot) are shown with vertical bars in Figure 4.1a-c. The uncertainties were calculated using the counting error as $\delta_Q = \sqrt{N_Q}$, where N_Q is the number of observations in the sample Q. When computing the uncertainties for the normalized occurrence rate given by Equation 4.2, we assume that the uncertainties from quantities in the denominator are negligible compared to those from $N_{eventsLANL}$. So, uncertainty δ of the risk for severe environment occurrence is:

$$\delta = \frac{\sqrt{\sum_{i=1990}^{2005} N_{eventsLANL_i}}}{\sum_{i=1990}^{2005} N_{Kp} norm_i \cdot N_{LANL_i}} \cdot 100\%. \tag{4.3}$$

As it can be noticed in Figure 4.1a-c, the uncertainties for *Kp* bins with less than 2 events (for *Kp* from 1 to 2 for LFHE and HFAE criteria, for *Kp* from 7 to 8 for PG5k and HFAE criteria and for *Kp* from 8 to 9 for HFAE criterion) have their lower limit as zero. Variations in both upper and lower limits in the uncertainty bars are important for determining a trend in the dependence of risks on the value of *Kp*. The risks which have their lower limit in the uncertainty bar equal to zero are considered much less significant and excluded when analyzing the dependencies.

The risk is different for each criterion (note that risk values for PG5k are not 100% directly comparable to other criteria). For PG5k, the highest risk (for all *Kp* bins with more than 1 events) to detect the severe environment is no more than $0.04\% \pm 0.008\%$, for LFHE, it is $0.2\% \pm 0.05\%$, for HFAE—$0.08\% \pm 0.02\%$, and for FE10k—$0.5\% \pm 0.2\%$. These numbers can look very small and give the impression that there is not whatsoever dependence of severe environment occurrence on any of *Kp* index value. It should be stressed particularly that while analyzing these numbers, it is important to keep in mind the definition of those selected 100 events in each criteria: only the top 100 15 minute-averaged worst-case severe environments. It is expected that the chance of getting the particular event out of only 100 selected at a certain time and spacecraft location for a particular *Kp* bin during 16 years cannot be high. The calculated uncertainties are much larger for higher *Kp* values when the number of events is very small. Overall, the smaller the number of events, the larger the uncertainty.

The analysis of risks shows the following:

(1) We see the order of magnitude difference in risks with the largest for FE10k criterion and smallest for PG5k criterion (keeping in mind eclipse events in PG5k criterion, see above).

(2) The only criterion which indicates an increase of observing severe environment with *Kp* increase is FE10k, highest fluxes of electrons at energies above 10 keV. All other criteria show the initial increase with *Kp* up to *Kp* = 4–5 and somewhat saturation at higher *Kp*. The trends in the uncertainties are in agreement with those of the risks. There are not so many events with $Kp > 6$–7 during all 16 years as the bottom panel shows. At the same time, the number of FE10k events for $Kp > 6$ is not small, therefore, worst-case severe environments can occur often when *Kp* is high, which is not true for other criteria.

The conducted analysis demonstrates that the magnetosphere needs to be in an active state ($Kp > 2$) for an event to happen but it is not necessarily true that a higher *Kp* value means that more events will be detected.

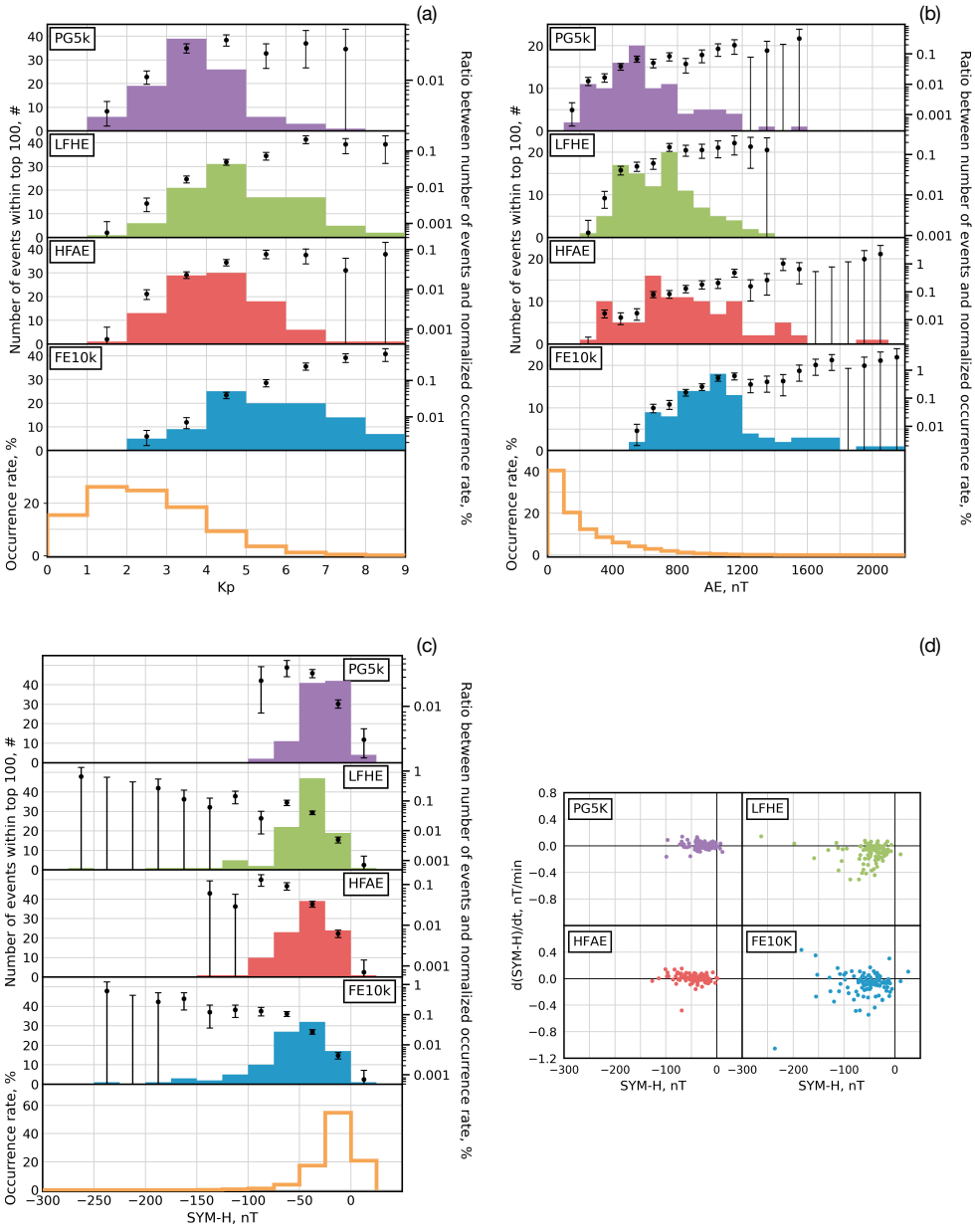

Figure 4.1: Number of events with top 100 15 minute-averaged worst-case severe environments for surface charging to occur for the criteria PG5k (top panel, purple), LFHE (second panel, green), HFAE (third panel, red), and FE10k (forth panel, blue) as dependent on the (a) *Kp* index, (b) AE index, and (c) SYM-H index. The occurrence rate (orange line) of the observed index for 1990-2005 is shown in the bottom panels. Black dots demonstrate the normalized severe environment occurrence rate with uncertainties shown as bars. (d) presents the d(SYM-H)/dt(SYM-H) versus SYM-H for all events for four criteria: Negative d(SYM-H)/dt values indicate the main phase of a storm (see the paper text for details).

4.3.1.2 AE Index

Figure 4.1b demonstrates the relationships between the events with top 100 15 minute-averaged worst-case severe environments for surface charging and the AE index in a similar form as in Figure 4.1a for the *Kp* index. The values used to plot each histogram (first four panels) are the median AE index observed during $\pm$ 5 min from the start of the worst-case severe environment event. The bottom histogram (orange line) presents the AE occurrence rate computed for the entire period of 1990–2005 irrespective of the environment conditions. The values for black dots and uncertainties for them were computed similarly to those of the *Kp* index.

The uncertainties for the AE bins with no LANL events between the AE bins where events are present (for example, in Figure 4.1b, for AE from 1200 nT to 1300 nT and from 1400 nT to 1500 nT for PG5k criterion) are computed assuming that the LANL events count is zero with a counting error of one for that bin, and the risk uncertainty is calculated using a counting error of one, instead of zero. For these bins, we show the risk at zero with its estimated upper limit uncertainty bar, lower limit being zero. The computed uncertainties for such bins are not significant for analyzing the trends in the parameter dependencies.

Analyzing the plotted histograms, it can be noticed that:

(1) Similarly to the *Kp* index, the histograms showing the number of severe environment events in all four criteria do not coincide with the 16 years occurrence rate of the AE index (orange line in the bottom panel). The maximum occurrence rate of 40% occurs at AE = 0–100 nT with 20% at AE = 100–200 nT, which corresponds to an absence of substorm activity or rather small substorms, hence, the AE index can be considered as an indicator for an event to happen.

(2) The PG5k spacecraft potential criterion histogram peaks with 20 events at AE of 500-600 nT where about 10 events occurred in each bin with AE from 200 to 800 nT. For higher AE values of 800–1200 nT, the number of events is low, not more than 5 in each AE bin and almost no events for AE$>$ 1200 nT. A rather different pattern can be seen on the flux-related FE10k criterion histogram, which has a peak of 18 events at AE of 1000–1100 nT with about 10 or more events in each AE bin for AE of 600 to 1200 nT. In contrast to the spacecraft potential criterion, there are events for AE$>$1200 nT (though, less than 5 in each AE bin but 20 in total). LFHE (20 events) and HFAE (15 events) criteria peaks are in the middle, being at 700–800 nT and 600–700 nT of AE, respectively. LFHE events of meaningful numbers occur when AE is between 300 and 1200 nT and for HFAE events this AE interval is 300–1600 nT—almost the same. Thus, similarly to Figure 4.1a, the FE10k environment is more likely to occur during increased magnetospheric activity compared to the other criteria.

(3) The normalized occurrence rate for severe environment events shown as black dots show that the highest risk to detect the severe environment is about one order of magnitude higher for three criteria, PG5k, HFAE and FE10k, when the AE index is elevated as compared to the *Kp* index. The

highest percentage of 2.3% $\pm$ 1.3% is again for flux-related FE10k criterion. At the same time, for HFAE criterion, it is 1.0% $\pm$ 0.5% and for PG5k—0.2% $\pm$ 0.1%. These are maximum values, but even if we look at the AE intervals with a meaningful number of events, the average percentages are still higher than for the *Kp* index. Again, regardless of the small percentages, the maximum chance of getting the particular event out of only 100 selected at a certain time and spacecraft location for a particular AE bin during 16 years is one order of magnitude higher than for the *Kp* index.

(4) We cannot state that there is a linear increase of the highest risk to detect the severe environment with the increase of the AE index (taking all the risks with non-zero lower limit for corresponding uncertainty). Black dots for all criteria show a decrease with the decrease of the observed events for higher AE values, but largest substorm activity (as indicated by the large AE index values) results in the highest probability for a severe environment to develop. Substorm activity (represented by AE) is a more important factor than a general disturbed state of the magnetosphere (represented by *Kp*) for severe environments for surface charging to occur.

4.3.1.3 SYM-H Index

Figure 4.1c demonstrates the dependencies of the events with top 100 15 minute-averaged worst-case severe environments for surface charging on the SYM-H index in a similar form as in Figure 4.1a for the *Kp* index and in Figure 4.1b for the AE index. The values for SYM-H at the first four panels are the median values of SYM-H from $\pm$ 10 min from the start of the worst-case severe environment event. The bottom histogram (orange line) shows the SYM-H occurrence rate similarly to Figure 4.1a for *Kp*. The black dots and uncertainties for them were computed in the same way as in Figure 4.1a for *Kp* index. The main features are the followings.

(1) The histograms showing the number of severe environment events in three criteria based on electron fluxes do not coincide with the 16 years occurrence rate of the SYM-H index (orange line in the bottom panel). The maximum occurrence rate of 55% occurs at SYM-H between 0 and -25 nT which is not during storm times and only 20% at positive SYM-H = 0–25 nT and at SYM-H from -25 to -50 nT which can indicate small storm activity. LFHE (45 events), HFAE (40 events), and FE10k (32 events) histograms have their peaks at SYM-H from -25 to -50 nT, but there are 28 events in FE10k criterion at SYM-H from -50 to -75 nT. In contrast to other criteria, all events in spacecraft potential criterion PG5k were detected for SYM-H > -100 nT (40 events were seen in each SYM-H interval of 0 to -25 nT and -25 to -50 nT).

(2) As for *Kp* and AE indices, more events in FE10k criterion were detected for higher magnitudes of SYM-H as compared to other criteria, which indicates that these events occur during larger storms as compared to other criteria: about 45 out of the 100 FE10k events occur at SYM-H < -50 nT, 25 events for LFHE and about 35 for HFAE.

(3) The severe environment normalized occurrence rate in each bin (black dots) show increase for all the criteria up to SYM-H in the -50 to -75 nT range (-50 to -100 nT for HFAE) and then a drop for PG5k and LFHE criteria and with consequent increase for LFHE events. Again, we do not analyze the SYMH bins where only 1 event was detected which show an increase in risks for large negative SYM-H with zero lower limit for uncertainties. For the FE10k criterion, the dots reach a saturation for SYM-H from -50 to -150 nT and then increase. Since there are very few events at large negative SYM-H, we cannot conclude that more events will occur at strong storm times.

(4) The severe environment risk percentages are small: only 0.04% $\pm$ 0.01% for PG5k, 0.14% $\pm$ 0.06% for LFHE, 0.13% $\pm$ 0.04% for HFAE and 0.3% $\pm$ 0.2% for FE10k. These percentages are very similar and highest for LFHE and FE10k criteria as those of the *Kp* index dependencies. Out of three indices, the AE index is the best indicator of a severe environment for surface charging to occur.

Figure 4.1d presents the time derivative of the SYM-H index versus the SYM-H index during the top 100 severe environment events (each point corresponds to one event). Four panels correspond to events selected using different criteria. The values for SYM-H are the median values of SYM-H from $\pm$ 10 min from the start of the worst-case severe environment event. To calculate the SYM-H index derivative, we transformed the SYM-H time-series to the frequency space using the fast Fourier transform (FFT). The FFT was computed for a $\sim$34 h interval centered on the event time. Harmonics with a period $<$6 hours (frequencies greater than $50.0 \cdot 10^{-6}$ Hz) were zeroed, and a derivative was computed after inverse transformation. It is, therefore, a derivative of a smooth signal, where all short-scale variations (substorm-related) were filtered out. Negative large d(SYM-H)/dt values when the SYM-H index is strongly negative indicate that main phase of a storm was in progress during worst-case severe environment events. Positive d(SYM-H)/dt values at negative SYM-H correspond to the storm recovery phase.

As can be seen, the spacecraft potential based PG5k events are all concentrated within SYM-H > -100 nT with most points at 0 to -50 nT and corresponding d(SYM-H)/dt values are $\pm$0.15 nT/min which corresponds to rather small increases and decreases in SYM-H during the events but not to any significant storms. Strong storm activity does not result in severe environments for surface charging with PG5k criterion. Similar features are noticeable for HFAE criterion: although covering larger SYM-H interval from 0 to -125 nT, d(SYM-H)/dt was $\pm$ 0.2 nT/min and only one event with -0.45 nT/min at about -75 nT of SYM-H which can correspond to a main storm phase. There are more events with positive d(SYM-H)/dt which can be an indicator that HFAE events occur during small storm recovery. As can be seen in Figure 4.1c, PG5k and HFAE criteria have the lowest risk for detecting severe environments for any SYM-H index range.

For LFHE criterion, the majority of events is still situated at SYM-H from 0 to -75 nT but

there are 9 events at SYM-H of -75 to -150 nT, most of the events have negative d(SYM-H)/dt with several reaching of about -0.4 to -0.5 nT/min which points to their occurrence during a storm main phase. It needs to be stressed here that the largest negative d(SYM-H)/dt values are still at SYM-H of -100 nT or more. FE10k criterion events are more distributed over SYM-H and d(SYM-H)/dt with many points concentrated at 0 to -75 nT of SYM-H but about the same number of them are with negative d(SYM-H)/dt values of -0.4 to -0.6 nT/min or more for SYM-H from 0 to -150 nT. One outlier is at -245 nT of SYM-H and with about -1 nT/min which corresponds to a strong storm. At the same time, about one third of all events are with positive d(SYM-H)/dt values but only 10 of them are during SYM-H < -100 nT which indicates that FE10k events mainly occur during small and moderate storm recovery. Thus, most of the LFHE events can occur during the main phase of small to moderate (up to -150 nT) storms. This is true for the FE10k events, although FE10k events can also be detected during small to moderate storm recovery phase.

4.3.2 Dependence on IMF and Solar Wind Parameters

4.3.2.1 IMF B_Z

Figure 4.2a presents, in a similar way as Figures 4.1a-c, the histograms of the top 100 events with worst-case severe environments for surface charging as dependent on the IMF B_Z observed during these events. The values of IMF B_Z at the first four panels are the averaged values of IMF B_Z during one hour before the worst-case severe environment event. The bottom panel shows the histogram of the occurrence rate (orange line) of the observed IMF B_Z for the entire period of 1990–2005 computed as the percentage ratio between the number of times when IMF B_Z fell into each bin (one bin is 2 nT) normalized by the total number of IMF B_Z observations during 1990-2005. The values for black dots and uncertainties for them were computed similarly as described for the *Kp* index (see Figure 4.1a description). IMF B_Z dependencies of the events of severe environments for surface charging show that:

(1) The occurrence rate (orange line) of the observed IMF B_Z has a symmetric shape in respect to IMF B_Z = 0 nT, with a maximum number at IMF B_Z = $\pm$ 2 nT. None of the histograms of each criterion has a similar peak location. This argues for the probability of detecting severe environments being dependent on IMF B_Z, so IMF B_Z can be considered as an factor influencing the occurrence of events. The histogram of the spacecraft potential based criterion PG5k shows a distinct, wider peak at IMF B_Z from 0 to -4 nT with 67 events for this IMF B_Z interval and <10 events for IMF $B_Z < -4$ nT. The HFAE histogram also exhibits a pronounced peak with 36 events at -4 nT $<$ IMF $B_Z < -2$ nT. Histograms for LFHE and FE10k show more distributed shapes, with a wider peak of 40 events at IMF B_Z from -2 nT to -6 nT and with 25 events at IMF B_Z from -4 nT to -6 nT, respectively.

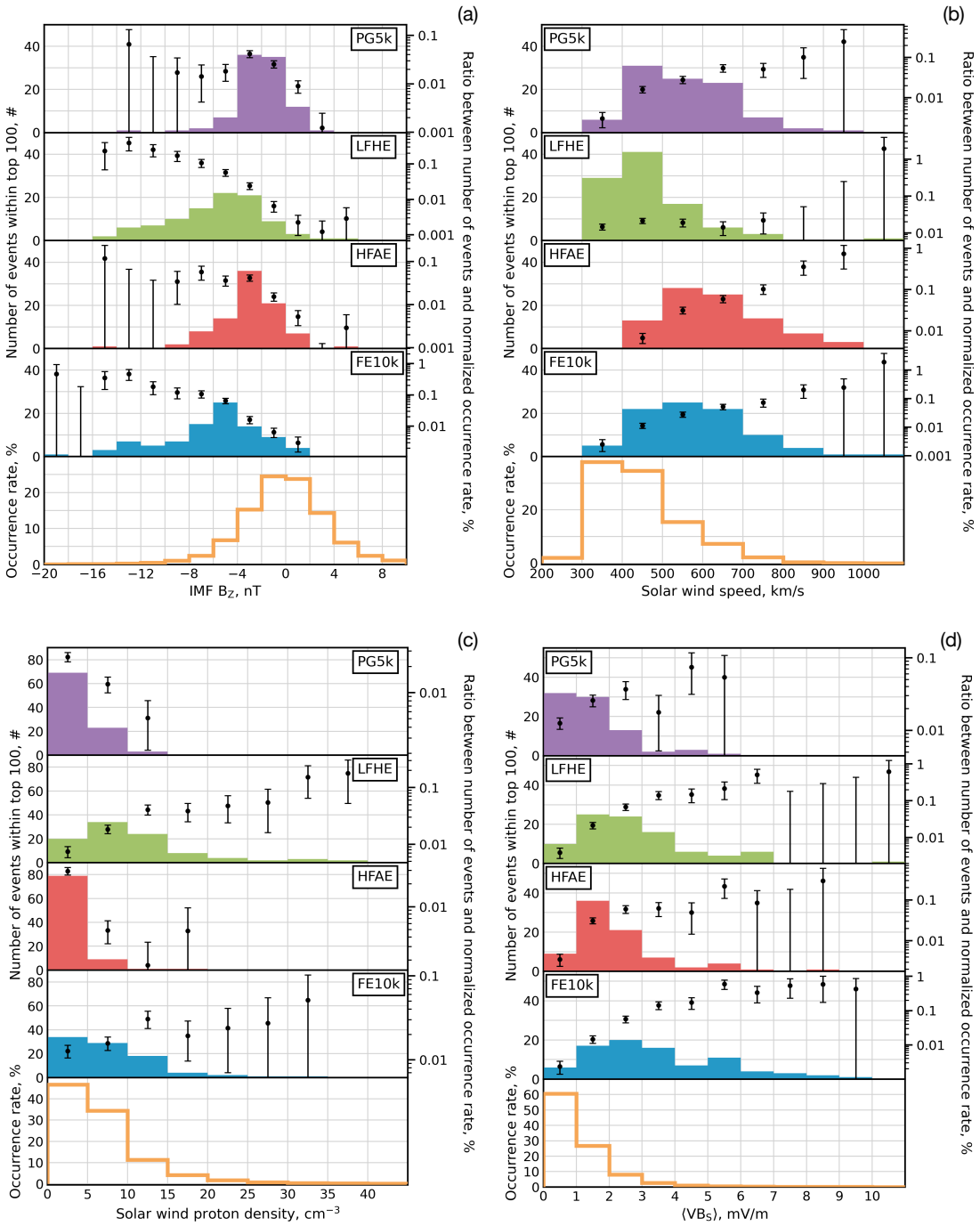

Figure 4.2: Similar to Figure 4.1, the number of events with top 100 15-minute-averaged worst-case severe environments for surface charging to occur for four criteria as dependent on the (a) IMF B_Z, (b) solar wind speed, (c) number density, and (d) $< VB_s >$ with the occurrence rate (bottom panel, orange) of the observed IMF and solar wind parameters for 1990–2005.

(2) In addition to the peaks, the majority of the events for all criteria have occurred when the preceding hourly averaged IMF B_Z was negative. At the same time, there are about 25 events (out of 400) which occurred when the average IMF B_Z was positive. These events are present for each criteria with the largest number for PG5k, then HFAE, FE10k, and with the smallest number for LFHE. Since we used averaged values of IMF B_Z during one hour before each event to plot the histograms, IMF B_Z should have been predominantly positive during that hour before the event but not necessarily all positive.

(3) More events with LFHE and FE10k criteria have occurred at IMF $B_Z < -6$ nT than for PG5k and HFAE criteria and they occur at -16 nT $<$ IMF $B_Z < -8$ nT when the number of PG5k and HFAE events were negligible.

(4) The risk to have severe environments represented by black dots with uncertainties increases with IMF B_Z becoming more negative for the LFHE and FE10k criteria but then it goes down in one IMF B_Z bin of -14 to -16 nT. For PG5k and HFAE criteria, there is no similar dependence: risk for PG5k criterion drops but for HFAE criterion it reaches some saturation at IMF $B_Z < -4$ nT. The ratio percentages are small, though, ranging from $0.04\% \pm 0.007\%$ to $0.46\% \pm 0.18\%$ and this is similar to those for *Kp* and SYM-H indices.

4.3.2.2 Solar Wind Speed

Similarly to Figure 4.2a, Figure 4.2b presents the dependencies of worst-case severe environments on the solar wind speed V_{SW}. The noticeable features are:

(1) The occurrence rate (orange line) of the observed V_{SW} has its maximum at V_{SW} = 300–500 $\mathrm{km \cdot s^{-1}}$ with higher rate at V_{SW} = 300–400 $\mathrm{km \cdot s^{-1}}$. None of the histograms of each criterion has the exact same peak location, except the histogram for LFHE criterion peaks with 40 events at V_{SW} = 400–500 $\mathrm{km \cdot s^{-1}}$ and with 29 events at V_{SW} = 300–400 $\mathrm{km \cdot s^{-1}}$. Other two criteria based on fluxes, HFAE and FE10k, do not exhibit any defined peaks in a specific V_{SW} interval with about 20 of events in each 100 $\mathrm{km \cdot s^{-1}}$ bin distributed over V_{SW} = 400–700 $\mathrm{km \cdot s^{-1}}$ for FE10k and 27 to 28 events each at V_{SW} = 500–700 $\mathrm{km \cdot s^{-1}}$ and 12 events each at V_{SW} = 400–500 and 700–800 $\mathrm{km \cdot s^{-1}}$. The histogram of the spacecraft potential based criterion PG5k also shows a wider peak covering V_{SW} = 400–700 $\mathrm{km \cdot s^{-1}}$ with 30 to 23 events. V_{SW} can be considered as an factor influencing the occurrence of events.

(2) For higher V_{SW} = 700–900 $\mathrm{km \cdot s^{-1}}$, there are more events corresponding to HFAE and FE10k criteria than with PG5k and LFHE.

(3) The risk to have severe environments represented by black dots with uncertainties increases with V_{SW} increase for PG5k, HFAE and FE10k criteria, reaching $0.1\% \pm 0.07\%$, $0.7\% \pm 0.4\%$ and $0.2\% \pm 0.1\%$, respectively. These percentages are about order of magnitude higher than those for IMF B_Z. The only criterion which exhibits an order of magnitude lower risk, as compared to

IMF B_Z is the LFHE one with a maximum value of 0.02% $\pm$ 0.003%. The risk for this criterion does not increase gradually with V_{SW} but dips into lower magnitude at V_{SW} = 600–700 $\mathrm{km \cdot s^{-1}}$ increasing again in the next V_{SW} interval.

In addition to the AE index, V_{SW} can be considered an indicator of a severe environment for surface charging to occur.

4.3.2.3 Solar Wind Proton Density

Figure 4.2c shows the histograms demonstrating the dependencies of worst-case severe environments on the solar wind number density N_{SW}. It can be seen that:

(1) Peaks of severe environment events for PG5k and HFAE criteria coincide with the maximum occurrence rate (orange line) of the observed N_{SW} at N_{SW} = 0–5 $\mathrm{cm^{-3}}$. The occurrence rate decreases for larger values of the observed N_{SW}, so does the number of PG5k and HFAE events, with almost no events detected at $N_{SW} > 10$ $\mathrm{cm^{-3}}$. The probability for a PG5k and HFAE event to happen does not depend on N_{SW}. The risk to have severe environments shown by black dots is about 0.03% $\pm$ 0.003% and decreases with the N_{SW} increase.

(2) Events with LFHE criterion show more distributed peak with 35 of them at N_{SW} = 5–10 $\mathrm{cm^{-3}}$ and with 20 each for N_{SW} = 0–5 and 10–15 $\mathrm{cm^{-3}}$. 5–8 events were detected at larger N_{SW}, even at N_{SW} = 30–40 $\mathrm{cm^{-3}}$. The risk to have severe environment for this criterion shown by black dots exhibits some gradual increase to only 0.05% at N_{SW} = 25–30 $\mathrm{cm^{-3}}$ with rise to 0.18% $\pm$ 0.13% at N_{SW} = 35–40 $\mathrm{cm^{-3}}$. The percentage is about 2 times smaller than that for IMF B_Z but an order of magnitude larger than that for V_{SW} for the same criterion.

(3) About 35 events for the FE10k criterion were detected at N_{SW} = 0–5 $\mathrm{cm^{-3}}$ but in the following N_{SW} intervals, the number of events did not drop sharply as for the PG5k and HFAE criteria (with 19 events at N_{SW} = 10–15 $\mathrm{cm^{-3}}$ and non-zero number of events up to N_{SW} = 30–35 $\mathrm{cm^{-3}}$). The risk to have severe environment for this criterion increases with N_{SW} increase with maximum percentage of 0.03% $\pm$ 0.007% which is about one of order magnitude smaller than that for IMF B_Z and V_{SW} for the same criterion.

Based on the analysis above, N_{SW} is not a good indicator of a severe environment for surface charging to occur.

4.3.2.4 $< VB_s >$

Figure 4.2d presents the dependencies of worst-case severe environments on $< VB_s >$, where V is the solar wind speed and B_s is equal to zero, when IMF $B_Z > 0$ and $B_s =$ IMF B_Z, when IMF $B_Z \leq 0$. The $< VB_s >$ values in $\mathrm{mV \cdot m^{-1}}$ in the first four panels are one hour averages before the start of each event. The $< VB_s >$ values in the bottom panel are calculated using a

running one hour averages over the years of 1990–2005. Note that the first bin of $< VB_s >$ (0–1 $\mathrm{mV \cdot m^{-1}}$) includes all zero values of B_s and all positive values of B_Z. Examining Figure 4.2d, it can be noticed that:

(1) The three criteria based on fluxes, LFHE, HFAE, and FE10k have their peaks at $< VB_s > > 1\ \mathrm{mV \cdot m^{-1}}$. That means that the preceding hourly averaged IMF B_Z was southward. LFHE criterion peaked with about 25 events in 1–3 $\mathrm{mV \cdot m^{-1}}$ bins, the HFAE criterion has a maximum of 35 events at $< VB_s >$ of 1–2 $\mathrm{mV \cdot m^{-1}}$, and FE10k shows a more distributed peak with 18–20 events in each bin from 1 to 4 $\mathrm{mV \cdot m^{-1}}$. For all three criteria, there are 10 or less events in the 0–1 $\mathrm{mV \cdot m^{-1}}$ bin. In contrast, PG5k criterion has about 30 events that occur in each of 0–1 and 1–2 $\mathrm{mV \cdot m^{-1}}$ bins. The occurrence rate (orange line) is highest at 0–1 $\mathrm{mV \cdot m^{-1}}$.

(2) A severe environment defined by the PG5k criterion has the lowest risk (black dots) to occur, $0.07\% \pm 0.04\%$, among all four criteria. A large number of events in the 0–1 $\mathrm{mV \cdot m^{-1}}$ bin coinciding with highest occurrence rate over 1990–2005 years and no obvious dependence of the risk on the magnitude of $< VB_s >$ can be also seen.

(3) Events with LFHE criterion were detected over a wide range of $< VB_s >$ values, up to 7 $\mathrm{mV \cdot m^{-1}}$, with one outlier event in the 10–11 $\mathrm{mV \cdot m^{-1}}$ bin. The risk for such an environment to occur is $0.5\% \pm 0.2\%$ and it increases with increasing of $< VB_s >$.

(4) HFAE and FE10k criteria events also occur at higher $< VB_s >$ magnitudes, up to 7 $\mathrm{mV \cdot m^{-1}}$ (with one event in 8–9 $\mathrm{mV \cdot m^{-1}}$ bin) and up to 10 $\mathrm{mV \cdot m^{-1}}$, respectively. The risk for the HFAE criterion severe environment to happen is $0.02\% \pm 0.1\%$ with no clear dependence on the $< VB_s >$ magnitude. For the FE10k criterion, the percentage is higher, $0.6\% \pm 0.18\%$, with no dependence on the $< VB_s >$ magnitude, either. Since $< VB_s >$ is computed based on IMF B_Z and V_{SW} values, the risks are higher than those for solar wind number density and comparable with those shown in Figures 4.2a and b.

4.3.3 Risks for Severe Environments for Surface Charging Dependent on Criteria Definitions

As was shown in the sections above, the peaks in the number of severe environment events and the risks for these events to happen depend on how they are defined in four criteria. Tables 4.2 and 4.3 summarize the obtained results of the above analysis of Figures 4.1 and 4.2.

Table 4.2 demonstrates for each criterion at what bin of the observed parameter the maximum number of the severe environment events was reached, together with the range in brackets of the parameter values at which the events were detected. The first row in the Table 4.2 also contains the observed ranges for each parameter during the 1990-2005 period (orange curves in the bottom panels in Figures 4.1 and 4.2).

Table 4.2: Peaks in number of events with corresponding parameter magnitude and range.

Criterion/ Parameter (range)	*Kp*, 0–9	AE, 0– 2200 nT	SYM-H, 50 – -300 nT	IMF B_Z, -20 – -10 nT	V_{SW}, 200 – 1100 $\mathrm{km \cdot s^{-1}}$	N_{SW}, 0 – 45 $\mathrm{cm^{-3}}$	$< VB_s >$, 0- 11 $\mathrm{mV \cdot m^{-1}}$
PG5k	3–4 (1–8)	500–600 (100–1600)	0 – -50 (25 – -100)	0 – -4 (4 – -14)	400–700 (300–1000)	0–5 (0–15)	0–2 (0–5)
LFHE	4–5 (1–9)	700–800 (200-1400)	-25 – -50 (25 – -275)	-2 – -6 (6 – -16)	400–500 (300–800)	5–10 (0–35)	2–3 (0–6)
HFAE	3–5 (1–9)	600–700 (200–2100)	-25 – -50 (25 – -150)	-2 – -4 (2 – -10)	500–700 (400–1000)	0–5 (0–20)	1–2 (0–7)
FE10k	4–5(7) (2–9)	1000–1100 (500–2200)	-25 – -75 (25 – -250)	-4 – -6 (2 – -20)	400–700 (300–900)	0–5 (0–35)	1–4 (0–10)

Table 4.3: Highest risk with corresponding uncertainty to detect a worst-case severe environment event at the corresponding value of the parameter and presence of a risk-parameter dependence.

Criterion/ Risk $\pm$ δ, % param. (D)	*Kp*	AE, nT	SYM-H, nT	IMF B_Z, nT	V_{SW}, $\mathrm{km \cdot s^{-1}}$	N_{SW}, $\mathrm{cm^{-3}}$	$< VB_s >$, $\mathrm{mV \cdot m^{-1}}$
PG5k	0.04 $\pm$ 0.008 4-5 (N)	0.2 $\pm$ 0.1 1100 (N)	0.04 $\pm$ 0.01 -75 (N)	0.04 $\pm$ 0.007 -4 (N)	0.1 $\pm$ 0.07 800 (Y)	0.026 $\pm$ 0.003 0 (N)	0.07 $\pm$ 0.04 4 (N)
LFHE	0.2 $\pm$ 0.05 6-7 (N)	0.2 $\pm$ 0.1 1100 (N)	0.14 $\pm$ 0.06 -150 (N)	0.4 $\pm$ 0.16 -14 (Y)	0.02 $\pm$ 0.003 700 (N)	0.18 $\pm$ 0.13 35 (Y)	0.5 $\pm$ 0.2 6 (Y)
HFAE	0.08 $\pm$ 0.02 5-6 (N)	1.0 $\pm$ 0.5 1400 (N)	0.13 $\pm$ 0.04 -100 (Y)	0.06 $\pm$ 0.02 -8 (N)	0.7 $\pm$ 0.4 900 (Y)	0.03 $\pm$ 0.003 0 (N)	0.2 $\pm$ 0.1 5 (N)
FE10k	0.5 $\pm$ 0.2 8-9 (Y)	2.3 $\pm$ 1.3 1700 (N)	0.3 $\pm$ 0.2 -175 (N)	0.46 $\pm$ 0.18 -14 (Y)	0.2 $\pm$ 0.1 800 (Y)	0.03 $\pm$ 0.007 10 (Y)	0.6 $\pm$ 0.18 8 (Y)

Table 4.3 shows, for each criterion, the maximum risk in percentage to detect a worst-case severe environment event with the corresponding value of the parameter at this risk together with yes (Y) or no (N) for the dependence of the risk on the parameter.

Let us determine, which parameter(s) can be considered as an indicator that a worst-case severe environment event would occur for each criterion. The PG5k is the only criterion which depends on the spacecraft potential, so it is supposed to be most relevant to surface charging events. It needs to be reminded that the majority of these events are in eclipse, so, they are with only the effect of plasma condition on spacecraft potential. This can lead to a very risky situation when the spacecraft is in eclipse and, for example, the values of V_{SW} are high.

For PG5k criterion:

(1) worst-case severe environments occur under slightly disturbed conditions (*Kp* = 3–4, moderate substorm activity of 500–600 nT, no storm activity, no significant IMF B_Z, N_{SW}, VB_s) but with V_{SW} elevated to 700 $\mathrm{km \cdot s^{-1}}$ (Table 4.2);

(2) two parameters, AE and V_{SW}, can serve as indicators of the increased risk (maximum of $0.2\% \pm 0.1\%$ at AE of 1100 nT and $0.1\% \pm 0.07\%$ at V_{SW} of 800 $\mathrm{km \cdot s^{-1}}$) for a worst-case severe environment event to occur and the risk for these events depends on the value of the parameters (Table 4.3).

The three other criteria are based on the fluxes and, therefore, are not directly related to the spacecraft potential. For the LFHE criterion:

(1) worst-case severe environments occur under moderately disturbed conditions (*Kp* = 4–5, moderate substorm activity of 700–800 nT, main phase of small storms, negative IMF B_Z of -6 nT, no significant increase in V_{SW}) but elevated N_{SW} of 5–10 $\mathrm{cm^{-3}}$ and $< VB_s >$ of 2–3 $\mathrm{mV \cdot m^{-1}}$ (Table 4.2);

(2) the highest risks are associated with IMF B_Z ($0.4\% \pm 0.16\%$ at -14 nT) and, as an effect, $< VB_s >$ ($0.5\% \pm 0.2\%$ at 6 $\mathrm{mV \cdot m^{-1}}$) and the risks exhibit dependencies on the values of these two parameters (Table 4.3). The question mark for the IMF B_Z dependence stresses that the last dot in Figure 4.2a, second panel, does not fit into the dependence. The third parameter, N_{SW}, though not with high risk percentage, influences the risk so that it increases with N_{SW} increase.

For the HFAE criterion:

(1) worst-case severe environments occur under moderately disturbed conditions (*Kp* = 3–5, moderate substorm activity of 600–700 nT, recovery phase of small storms, negative IMF B_Z of -4 nT, no significant N_{SW} and $< VB_s >$) but with V_{SW} elevated to 700 $\mathrm{km \cdot s^{-1}}$ (Table 4.2);

(2) similarly to the PG5k criterion, two parameters, AE and V_{SW}, are related to the highest risks

for a worst-case severe environment event to occur (1.0% $\pm$ 0.5% at 1400 nT and 0.7% $\pm$ 0.4% at 900 $\mathrm{km \cdot s^{-1}}$), but only the risk associated with V_{SW} depends on its value. The third highest risk of 0.2% $\pm$ 0.1% is for $< VB_s >$ which follows from the high risk for V_{SW}.

For the FE10k criterion:

(1) worst-case severe environments occur under slightly more intensely disturbed conditions (*Kp* = 4–5(7), intense substorm activity of 1000–1100 nT, main and recovery phases of small to moderate storms, negative IMF B_Z of -6 nT, no significant N_{SW}) but with V_{SW} elevated to 700 $\mathrm{km \cdot s^{-1}}$ and, as follows, VB_s of 2–3 $\mathrm{mV \cdot m^{-1}}$ (Table 4.2);

(2) all parameters (except of V_{SW} and N_{SW}) have higher risks, as compared with the other three criteria, and for all of them (except of AE and SYM-H) the associated risks show the dependencies of parameters' values.

Thus, to summarize:

(i) the range of geomagnetic conditions for maximum number of worst-case severe environments for surface charging to occur including all four criteria:

(a) moderately disturbed with *Kp* from 3 to 5;

(b) moderate to intense substorm activity with AE from 500 to 1000 nT;

(c) storm activity from none to main and recovery phases of small to moderate storms;

(d) slightly negative IMF B_Z up to -6 nT;

(e) V_{SW} from 400 and elevated to 700 $\mathrm{km \cdot s^{-1}}$;

(f) low N_{SW} with 5–10 $\mathrm{cm^{-3}}$ only for one criteria of LFHE;

(g) as follows from IMF B_Z and V_{SW}, $< VB_s > < 4\ \mathrm{mV \cdot m^{-1}}$.

(ii) geomagnetic indices and IMF and solar wind parameters and their relations to the maximum risks for worst-case severe environments for surface charging to occur including all four criteria:

(a) *Kp* index is not associated with highest risk for worst-case severe environments to occur, the only criterion is FE10k for which the risk and the *Kp* value are related;

(b) AE index determines the highest/close to highest risk, except for the LFHE criterion, but the risk is not dependent on the AE magnitude;

(c) no high risk is related to the SYM-H index and there is no dependence on its value for the risk;

(d) elevated risks with not 100% clear dependencies exist for IMF B_Z;

(e) V_{SW} directly indicates the highest risk for worst-case severe environments to happen and this risk depends on the V_{SW} value, except for the LFHE criteria;

(f) no high risk is associated with the N_{SW} but the risk depends on N_{SW} magnitude for the LFHE and FE10k criteria;

(g) the risks for $< VB_s >$ are determined by the risks for IMF B_Z and V_{SW}.

AE and V_{SW} are the most important parameters which can define the occurrence of worst-case

severe environments for surface charging.

4.4 Worst-Case Severe Environments for Surface Charging with Superimposed Epoch Analysis

In addition to studying the dependencies of severe environments for surface charging on current activity defined by geomagnetic indices (Figure 4.1) and one hour averaged IMF and solar wind parameters (Figure 4.2), we conducted the superimposed epoch analysis for all the detected events with four criteria. The observed index or IMF or solar wind parameter during an event was plotted a certain number of hours before and after the time of an event and all of the plots were combined setting the time of the events as zero for all of them. Such analysis helps to identify the general behaviour of the observed index or IMF or solar wind parameter before and after all events belonging to a specific criterion.

4.4.1 Geomagnetic Indices

Figure 4.3 demonstrates the results of the superimposed epoch analysis conducted for the variations of (a) *Kp*, (b) AE, (c) AL, and (d) SYM-H indices at around the detected top 100 15-minute-averaged worst-case severe environments for surface charging. As in previous Figures 4.1 and 4.2, top panel is for PG5k (purple), second panel is for LFHE (green), third panel is for HFAE (red), and bottom panel is for FE10k (blue) criteria. Each panel presents the median value for the corresponding index (thick line, bold squares for *Kp*) with the shaded area (bars for *Kp*) of the interquartile range (25th–75th percentile). In Figure 4.3a, for each event, the observed *Kp* values are plotted for every 3 hours for the interval of 24 hours before and 12 hours after an event for the four criteria. The *Kp* index does not change much before and after events in the PG5k and HFAE criteria. At the same time, the *Kp* values before and after events were not low: around 3 for a PG5k event and 4 for a HFAE event (as shown by median). Two other criteria, both flux related, show the increase in *Kp* index before and decrease after the event with the peak at the time of the event. For LFHE events, the *Kp* index starts to increase from low values of 2 to 3 about 9 hours before the event reaching about 4.5 at the time of the event with subsequent gradual decrease to 3 twelve hours after the event. The *Kp* index was somewhat elevated being between 3 and 4 during 24 to 6 hours before the event in the FE10k criterion, reached about 5.3 and decreased to 4 in 12 hours after the event. These variations are not big; nevertheless, the pattern of *Kp* changes as seen in the superimposed epoch analysis confirm that the magnetosphere needs to be in an active state (*Kp* >2) for an event to occur.

Figure 4.3b shows the observed 1 min AE values plotted 9 hours before and 6 hours after the event for four criteria. For all criteria, the AE index was elevated as compared to times before and after an event. For the spacecraft potential criterion PG5k, the AE was about 300–400 nT during 8 hours and then increased up to 600 nT during 1 hour before the event with gradual decrease back to about 300 nT (looking at median values). The AE index during LFHE events gradually increased from 200 nT 9 hours before the event reaching maximum values of 600 nT 1 hour before the event and starting to decrease right at the time of the event, also going gradually back to 300 nT 6 hours after the event.

The AE index during HFAE and FE10k criteria events shows the most sharp peaks. The AE index for HFAE events reached its peak of 800 nT during 1 hour before the event being about 400 nT during 8 preceding hours and returned to this value of 400 nT in 2 hours after the event. The AE index for FE10k events started to increase from 400 nT magnitudes 5 hours before the event with the peak value of 1000 nT at the time of the event and decreased in 3 hours to 500 nT.

The AE index (T. N. Davis & Sugiura, 1966) was developed to reflect the strength of ionospheric currents flowing in the auroral oval during substorms. The AE index is the difference between the AU (auroral upper) index, which measures the strength of the eastward electrojet flowing from mid-afternoon toward midnight, and the AL (auroral lower) index which measures the strength of the westward electrojet that flows from dawn to past midnight. The AL component of AE is especially useful for substorm studies, since it is sensitive to the ionospheric currents that flow through the auroral bulge during the expansion phase (Akasofu et al., 1965). Therefore, in addition to the AE index, we show also the variations of the AL index in the present study. Figure 4.3c shows the observed 1 min AL values, similarly to Figure 4.3b. For the AE index, the events in all four criteria occur when the AL index has its peaks (minima in this case). The most sharp and deep minima in AL are seen again for HFAE and FE10k criteria events, -600 nT and -750 nT in median, respectively. The behavior of AL is very similar as to AE before and after the events. The most gradual decrease before the event and recovery after the event is again evident for LFHE events: the minimum of -450 nT is reached 1 hour before the event and the recovery starts right at the event. The AL index during PG5k events exhibits a pattern very similar to the one for the AE index.

In Figure 4.3d, 1 min SYM-H values are plotted 24 hours (1 day) before and 72 hours (3 days) after the event for four criteria. The behavior of the SYM-H index is similar to that of the *Kp* index in such a way that no significant changes exist in the SYM-H index as seen in the median lines during PG5k and HFAE events but SYM-H variations are present for LFHE and FE10k criteria events (see Figure 4.3a for comparison). During PG5k events, the median SYM-H index is about -20 nT 1 day before and 3 days after the event with slight decrease to -25 nT at the time of the event. The median SYM-H during HFAE events does not show any dips before or after the event

but SYM-H is -40 nT 1 day before the event and as can be seen in the interquartile range, SYM-H can reach -60 nT and stay like that 1 days before the event gradually increasing to -40 nT after. The only criterion for an event to happen when SYM-H is minimal and the whole pattern of the SYM-H corresponds to a storm time one is the LFHE criteria. SYM-H being about -15 nT in median 1 day before the event, starts to decrease sharply 4 hours before the event. LFHE events occur during rather moderate SYM-H values, no lower than -60 nT in minimum. In 3 days, the SYM-H index recovers back to -20 nT. During FE10k events, the SYM-H index also decreases before the event but more gradually than during LFHE events. The event occurs right before the SYM-H minimum, not at the minimum. The minimum SYM-H value can be as low as -90 nT within 8 hours after the event according to the interquartile range. It should be noted that out of all indices, only AE and AL demonstrate clear variation for a PG5k event (PG5k is the only criterion connected to spacecraft potential).

4.4.2 IMF and Solar Wind Parameters

Similarly to Figure 4.3, Figure 4.4 demonstrates the results of the superimposed epoch analysis conducted for the variations of (a) IMF B_Z, (b) solar wind speed V_{SW}, (c) number density N_{SW}, and (d) E_y electric field at around the detected top 100 15 minute-averaged worst-case severe environments for surface charging. In the superposed epoch analysis, we use E_y instead of $< VB_s >$, since the latter one is proportional to the integral (over 1 hour prior to the epoch zero) of the former with zeroed values corresponding to positive IMF B_Z measurements. Thick lines represent the median values at each 5 min time step and shaded area defines the interquartile range (25th–75th percentile).

In Figure 4.4a, for each event, the observed 5 minute IMF B_Z values are plotted for the interval of 24 hours before and 8 hours after an event for four criteria. As can be seen, the most pronounced changes in the IMF B_Z behavior before and after the event are for LFHE and FE10k criteria events, while changes are not so big for PG5k and HFAE events. During all events, IMF B_Z exhibits a minimum but the occurrence of this minimum does not coincide with the time of the event, being always before the event. The delay is 1–2 h which is around a typical substorm growth phase timescale.

For the LFHE criterion, the IMF B_Z stays at about 0 nT in median from 24 to 8 hours before the event, then starts to decrease, reaching its minimum of about -6 nT 1.5 hours before the event. IMF B_Z recovers to zero by the 5th hour after the event but then drops to -2 nT. During the recovery, the range of interquartiles is wider than before the event, being -2 to 2 nT from the median. IMF B_Z during the FE10k criterion events show very similar time-dependence: it decreased slowly to -2 nT from 12 to 4 hours before the event and then dropped faster to -6 nT

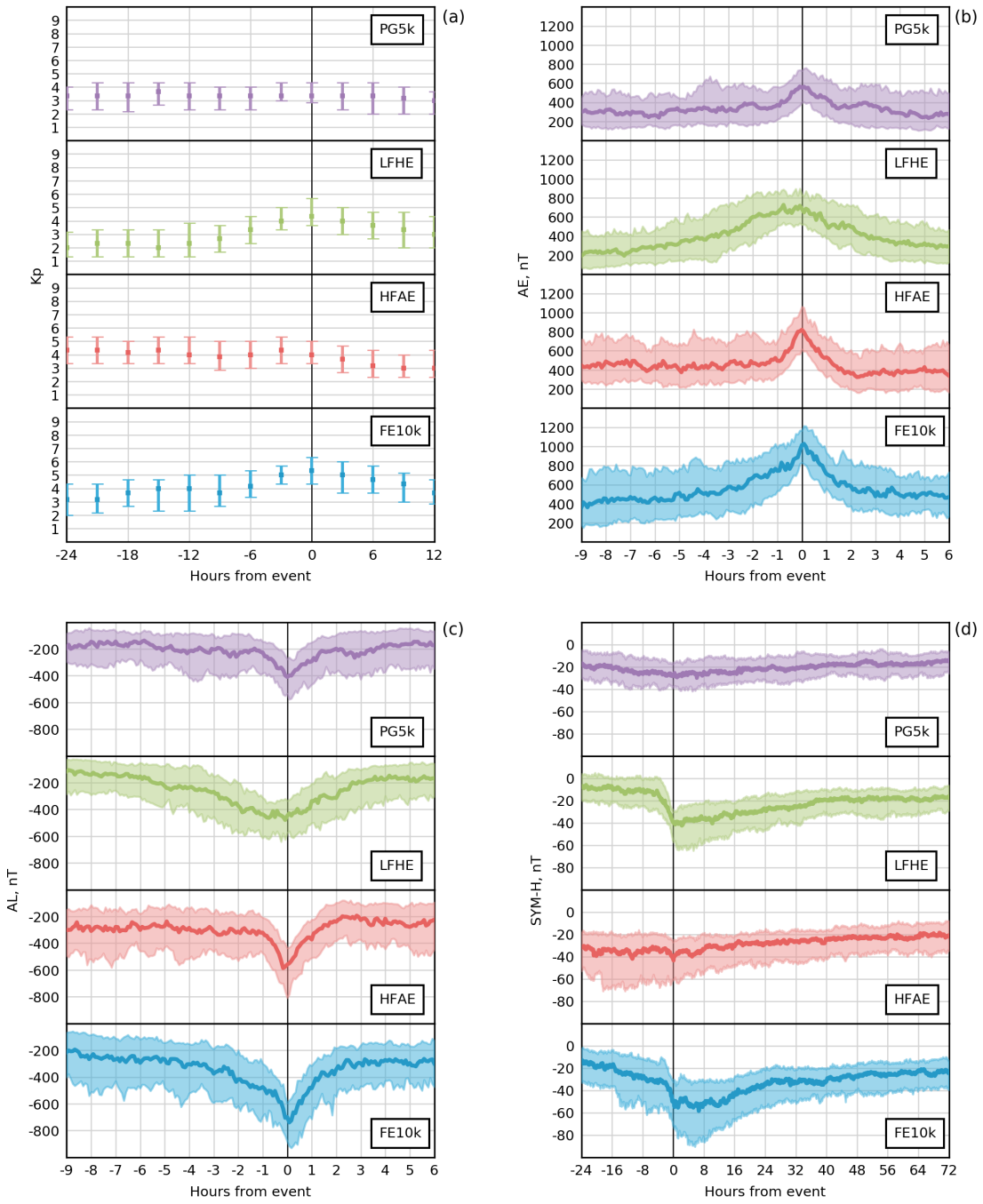

Figure 4.3: Superimposed epoch analysis for the variations of (a) *Kp*, (b) AE, (c) AL, and (d) SYM-H indices at around the detected top 100 15-minute-averaged worst-case severe environments for surface charging. Thick lines represent the median index value at each 1 min time step (bold squares for median *Kp* value at each 3-hour time step) and shaded area (bars for *Kp* index) defines the interquartile range (25th–75th percentile).

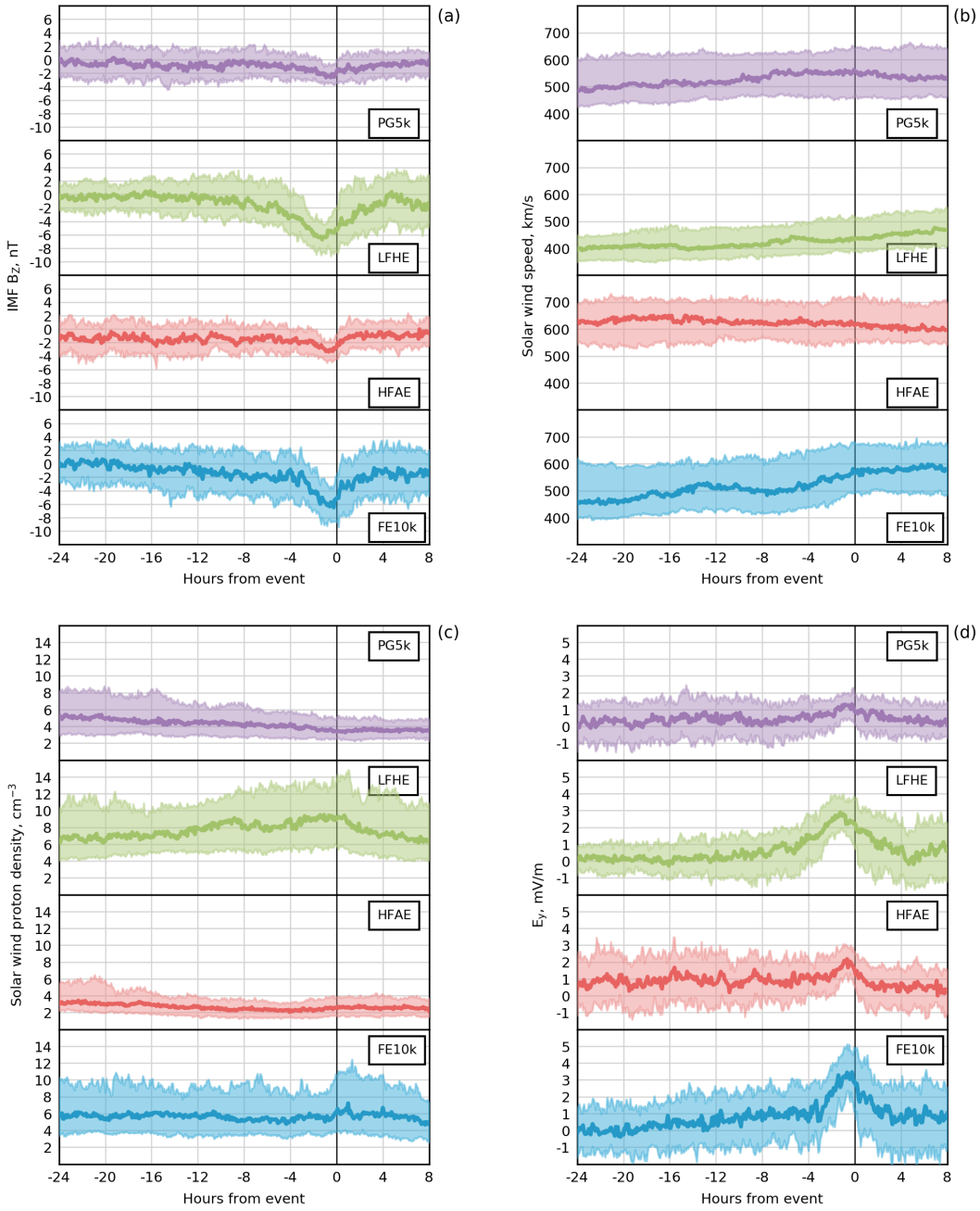

Figure 4.4: Similarly to Figure 4.3, superimposed epoch analysis for the variations of (a) IMF B_Z, (b) solar wind velocity, (c) number density, and (d) E_y electric field at around the detected top 100 15-minute-averaged worst-case severe environments for surface charging. Thick lines represent the median values at each 1 min time step and shaded area defines the interquartile range (25th–75th percentile).

at about 1 hour before the event. It comes back to about -1 nT 4 hours after the event. During PG5k and HFAE events, IMF B_Z decreases before and increases after the event but the change is not larger than 1 nT.

Figure 4.4b presents the observed 5 minute V_{SW} values plotted for the interval of 24 hours before and 8 hours after an event for the four criteria. No sharp variations in V_{SW} can be seen before and after the events in all four criteria, but V_{SW} is noticeably higher than the average solar wind velocity ($\sim$400 $\mathrm{km \cdot s^{-1}}$) for all but LFHE criteria. For events in the PG5k criterion, V_{SW} is at about 500 $\mathrm{km \cdot s^{-1}}$ from 24 to 8 hours before the event and then increases to 550 $\mathrm{km \cdot s^{-1}}$ and stays at that value. For events in the LFHE criterion, again from 24 to 8 hours before the event, V_{SW} is at 400 $\mathrm{km \cdot s^{-1}}$ and then gradually increases to 470 $\mathrm{km \cdot s^{-1}}$ by the 8th hour after the event. V_{SW} magnitudes are the highest for HFAE events, being 600–650 $\mathrm{km \cdot s^{-1}}$ throughout all the time interval. FE10k criterion events correspond to the largest, though smoothest changes in V_{SW} before and after the event: from 460 to 600 $\mathrm{km \cdot s^{-1}}$.

Similarly to Figures 4.4a and 4.4b, Figure 4.4c shows the observed 5 minute N_{SW} values for the four criteria. As in case of V_{SW}, PG5k and HFAE events are not associated with changes in N_{SW}: N_{SW} is about 4–5 $\mathrm{cm^{-3}}$ for PG5k and about 3 $\mathrm{cm^{-3}}$ for HFAE criteria as seen in the median values. The interquartile range in N_{SW} is wider for the PG5k criterion 24 hours before the event (3–8 $\mathrm{cm^{-3}}$) and then narrows down to ± 1 from the median value at the event and 8 hours after. For LFHE events, N_{SW} is elevated to 7 $\mathrm{cm^{-3}}$ during 24 to 14 hours before the event, then starts to increase gradually, reaches 9 $\mathrm{cm^{-3}}$ at the event, and decreases to 6 $\mathrm{cm^{-3}}$ 8 hours after the event. The interquartile range is wider than for PG5k and HFAE events being 6–14 $\mathrm{cm^{-3}}$ at the event. In any case, there are no sharp variations in N_{SW}. During FE10k events, N_{SW} changes are also small, N_{SW} stays at 6 $\mathrm{cm^{-3}}$ from 24 hours right up to 1 hour before the event, then increases slightly and comes back to the initial value.

Variations of the derived E_y presented in Figure 4.4d reflect very much of the variations in IMF B_Z seen in Figure 4.4a. For all criteria, E_y has a peak right at about 1 hour before the event. The smallest peak is observed during PG5k events, the sharpest—during FE10k events. Monotonic increase of E_y from 0 to 1 $\mathrm{mV \cdot m^{-1}}$ until 3 hours before the event, then increase to about 3.5 $\mathrm{mV \cdot m^{-1}}$ in 2 hours and subsequent decrease back to initial magnitudes are typical characteristics of FE10k events. The interquartile range is 2–5 $\mathrm{mV \cdot m^{-1}}$. During LFHE events, E_y stays at around 0 until about 8 hours before the event, then starts to increase more gradually than during FE10k events and reaches a peak median value of 3 $\mathrm{mV \cdot m^{-1}}$. The E_y goes back to 0 values after the peak until 5 hours after the event and then increases up to 1 $\mathrm{mV \cdot m^{-1}}$. HFAE events correspond to a smaller peak in E_y: E_y oscillates around 1 $\mathrm{mV \cdot m^{-1}}$ until about 2 hours before the event and then increases by only 1 $\mathrm{mV \cdot m^{-1}}$ recovering in 3 hours back to initial magnitudes. During PG5k events, the changes in E_y are very small: the E_y values lie between 0 and 1 $\mathrm{mV \cdot m^{-1}}$

Table 4.4: Parameter changes with time before the event/relative timing of parameter maximum change and the even/and after the event

Criterion/ Parameter	ΔKp	ΔAE, nT	ΔAL, nT	ΔSYM-H, nT	ΔIMF B_Z, nT	ΔV_{SW}, $\mathrm{km \cdot s^{-1}}$	ΔN_{SW}, $\mathrm{cm^{-3}}$	$\Delta < VB_s >$, $\mathrm{mV \cdot m^{-1}}$
PG5k	No	300 in 1h/ max at/ 4h	200 in 1.5h/ max at/ 1.5h	No	No (2 1h before)	No	No	1 in 8h/ max 1h before/4h
LFHE	2 in 9h/ max at/ 12h	600 in 8h/ max 1h before/ 6h	230 in 6h/ max 0.5h before/3h	30 in 4h/ max at/ 36h	6 in 8h/ max 1h before/5h	50 grad. inc.	3 grad. inc./ decr.	3 in 8h/ max 1.5h before/4h
HFAE	No	400 in 1h/ max at/ 2h	300 in 1h/ max 20 min before/2h	No	No (2 1h before)	No	No	1 in 2h/ max 1h before/2h
FE10k	2 in 6h/ max at/ 12h	600 in 5h/ max at/ 3h	450 in 5h/ max at/ 2h	50 in 24h/ max 4h after/>40h	6 in 4h/ max 1h before/4h	100 grad. incr.	No	3 in 4h/ max 1h before/4h

and increase only up to 1.5 $\mathrm{mV \cdot m^{-1}}$ 1 hour before the event.

4.4.3 Time History for Severe Environments for Surface Charging Dependent on Criteria Definitions

Similarly to the results presented in previous sections, the time history of the parameters before, at and after the events of severe environments for surface charging differs for different criteria definitions. Table 4.4 summarized the noticeable parameter changes over time before the event (for example, there is a 300 nT change in AE during 1 hour before the event), the time when the maximal change (maximum or minimum) in the parameter occur relative to the time of the event (for example, the AE peaks at the time of the event), and how many hours it takes for the parameter to recover to its initial magnitude (for example, it take about 4 hours for AE to recover) for the four criteria. All numbers refer to the median values seen in Figures 4.3 and 4.4.

For the PG5k criterion based on the spacecraft potential, no changes are seen in the *Kp* and SYM-H indices, solar wind velocity and number density. IMF B_Z exhibits a small, rather questionable change of 2 nT during 1 hour before the event and, as a consequence, E_y shows 1 $\mathrm{mV \cdot m^{-1}}$ change in 8 hours before the event. The only noticeable change is in AE (and AL) with 300 nT in 1 hour before the event (200 nT in 1.5 hours for AL), and the peak in AE (and minimum drop in AL) occurred at the time of the event with fast recovery.

For the flux based LFHE criterion, all parameters change but on a longer time period, more than in 1 hour before the event as seen in the PG5k criterion. The *Kp* index increases from 2 to 4 in 9 hours before the event, reaching its maximum at the time of the event and slowly recovering in 12 hours. AE (600 nT in 8 hours) and AL (230 nT in 6 hours) show gradual changes with no distinct

peaks. The maximal change occurs 0.5–1 hour before the event. Even more gradual changes are seen for V_{SW} (only 50 $\mathrm{km \cdot s^{-1}}$ change) and N_{SW}. Sharp changes are present in SYM-H (30 nT in 4 hours with maximum at the event with long recovery) but they are not large. IMF B_Z drops from 0 to -6 nT in 8 hours reaching minimum of -6 nT 1 hour before the event and so E_y has a peak 1.5 hours before the event with 3 $\mathrm{mV \cdot m^{-1}}$ change from 0 in 8 hours.

Behaviour of the parameters during HFAE events is rather similar to the PG5k criterion. No changes can be seen for *Kp* and SYM-H indices, solar wind velocity and number density with small changes in IMF B_Z and VB_s. Again, the only parameters with significant changes are AE and AL. They exhibit sharp changes of 300–400 nT in 1 hour before the event with maximum change at the time of the event (20 minutes shift for AL) with fast recovery of 2 hours.

Events with the last criterion, FE10k, are associated with significant changes in all parameters, except for V_{SW} and N_{SW}. *Kp* changes by 2 in 6 hours, AE increases by 600 nT in 5 hours, AE drops by 450 nT in 5 hours and they all have their maximal change at the time of the event. SYM-H shows a rather gradual decrease of 50 nT in 24 hours with maximal drop 4 hours after the event and long recovery. IMF B_Z and E_y change by 6 nT and 3 $\mathrm{mV \cdot m^{-1}}$, respectively, in 4 hours reaching maximal change 1 hour before the event.

Thus, based on the significance and timing of changes in the parameters before and at the events of severe environments for surface charging for different criteria definitions, we can summarize as follows:

(a) No changes are seen in V_{SW} and N_{SW} for all four criteria;

(b) A substorm-type pattern of the superimposed epoch AE (AL) dependencies for all criteria: 300–600 nT changes in AE (AL) are associated with the events for all four criteria with maximum change coinciding with the time of the event (gradual changes with maximum 1 hour before the event for LFHE events);

(c) A storm-type pattern of the superimposed epoch SYM-H dependencies for LFHE and FE10k criteria, not for PG5k and HFAE criteria: 30 nT sharp drop at the event for LFHE and gradual 50 nT drop 4 hours after the event for FE10k;

(d) The *Kp* index starts to increase 6–9 hours before the event with the change of about 2 reaching maximum at the time of the event for 2 (LFHE and FE10k) out of 4 criteria;

(e) Southward turning in IMF B_Z: for LFHE and FE10k events, IMF B_Z starts to decrease from being 0 and reaches maximum drop of 6 nT in 4–8 hours at 1 hour before the event occurring. Small changes of no more than 2 nT with maximum at 1 hour before the event are seen for PG5k and HFAE events. Corresponding changes are evident in E_y.

AE and IMF B_Z are the parameters with the most definite changes before and at the time of the events of worst-case severe environments for surface charging.

4.5 Discussion and Conclusions

The occurrences of 400 worst-case severe environments for surface charging observed by LANL satellites during the years of 1990–2005 were analyzed based on the definitions of four criteria for the worst-case severe environments developed by Matéo-Vélez et al. (2018) and the activity parameters with their time history, such as *Kp*, AE, AL, and SYM-H indices and IMF B_Z, solar wind speed, proton number density, and derived electric field E_y and $< VB_s >$. In addition to the occurrences (or numbers of events as histograms in Figures 4.1 and 4.2) of worst case severe environments, the normalized severe environment occurrence rate was introduced (shown as black dots with uncertainties in Figures 4.1 and 4.2). These normalized occurrence rates are the indicators of a risk to detect a top 100 worst-case severe environment event in a 15 min window for a given parameter bin.

For the *Kp* index to be considered as the main indicator of the probability for a satellite anomaly to be detected, no *Kp*-dependent high risk for worst-case severe environments for surface charging was found. During all events, the magnetosphere was moderately disturbed with *Kp* ranging from 3 to 5. This is in agreement with the previous studies by, for example, Choi et al. (2011); Thomsen et al. (2013); Matéo-Vélez et al. (2018, 2019), (more citations can be found in the Introduction section) where it was stated that rather moderate *Kp* values were observed during the charging events. Charging events do not necessarily require high values of *Kp*.

The AE index was found to be a very special indicator of the highest risk for severe environments for surface charging to happen. Before and after the events in all criteria, the AE (AL) index shows a substorm-type pattern with max/min at the time of the event. This is in agreement with many previous studies relating the observed spacecraft anomalies with the presence of substorm activity. For example, Saiz et al. (2018) found that during the loss of Telstar 401 on 11 January 1997, the *Kp* index reached only 4, but a substorm occurred about 45 min before the anomaly (similarly to LFHE criteria). Iucci et al. (2005, 2006) have developed and analyzed the database of anomalies from Russian Kosmos satellites which occurred during 1971–1997. Based on the dependence on the local time and AE index, they concluded that local-time dependent anomalies were due to 10–15 keV electrons injected into the magnetosphere as a result of auroral substorms. Loto'aniu et al. (2015) analyzed the space weather conditions at and around the time of the widely-studied anomaly (Allen, 2010) at geosynchronous Galaxy 15 spacecraft at local midnight and concluded that the attributed onboard electrostatic discharge was due to the interactions of the spacecraft with substorm-injected energetic particles leading to spacecraft charging. At the same time, our analysis shows that the risk for severe environments for surface charging does not depend on the AE magnitude. The presence of substorm activity can tell us that the environment can be severe for surface charging to occur, but the surface charging will not depend on whether a substorm was

moderate or intense.

Storm-type patterns of the SYM-H behavior during the events with LFHE and FE10k criteria based on low energy fluxes were obtained, but no high risk and no dependence on the strength of a storm were found related to the SYM-H index. Not many studies have attempted to relate the Dst index with the observed anomalies. One of them by W. Lohmeyer and Baker (2012) correlated Inmarsat anomalies with only a -25 nT drop in the Dst index. Most of the events in the present study which had relations to the SYM-H index occurred during main and recovery phases of small to moderate storms with SYM-H above -100 nT. At the same time, many events occurred without any relation to any storm. Thus, there is no need for a storm of any strength to happen in order for a surface charging event to be detected.

If the detection of a severe environment for surface charging requires ongoing substorm activity, then AE (AL) index, but not *Kp* or SYM-H (Dst), is naturally best suited to characterize this environment. Related to that, it is also quite expected that superimposed epoch IMF B_Z revealed the southward turning pattern 1 hour before the events. The IMF B_Z itself cannot serve as an indicator of a risk to have a severe environment. Sillanpää et al. (2017) conducted the analysis of GOES 13 MAGED data for 5 years (2011-2015) and developed an empirical model for the 40–150 keV electron fluxes at geostationary orbit. They found that 1.5 h delayed IMF B_Z and V_{SW} are the driving parameters for the best correlation between the modeled and observed electron fluxes. Ganushkina et al. (2019) further confirmed this. Indeed, according to our present study, V_{SW} is related to the highest risk worst-case severe environments and this risk depends on the V_{SW} magnitude. The difference is that the time history of V_{SW} before and after the events in all four criteria for worst-case severe environments does not contain any significant variations. The event of worst-case severe environment is not related to V_{SW} sharp changes but it occurs when V_{SW} is elevated to 500–700 $\mathrm{km \cdot s^{-1}}$ for prolonged periods.

Saiz et al. (2018) reported that in the case of Telstar 401 anomaly, the most important parameters were large (>10 nT) fluctuations of IMF B_y and high solar wind dynamic pressure (reaching 50 nPa). We included N_{SW} in the list of the studied parameters and found no risk associated with it and no changes in the time history of it.

Our last parameter is $< VB_s >$, which has been used in modelling of low energy electron fluxes. For example, Denton et al. (2016) introduced the empirical model of the electron fluxes and ion fluxes at geosynchronous orbit as a function of local time, energy, and $< VB_s >$. Stepanov et al. (2021) used THEMIS (The Time History of Events and Macroscale Interactions during Substorms) dataset to investigated a relative importance of the various external driving parameters for the superthermal electron flux variations. The authors ranked solar wind reconnection electric field Ekl ($\mathrm{Ekl} = VB_{yz}\sin^2(\theta/2)$) as the second (in its importance, after V_{SW}) parameter controlling 10 keV electron flux. Obviously, $< VB_s >$ defines the risks for worst-case severe environments

according to those of IMF B_Z and V_{SW}.

Among four criteria for surface charging related, severe environments developed by Matéo-Vélez et al. (2018), LFHE and FE10k criteria based on the enhancements of low energy particle fluxes show definitely clearer dependencies on the solar wind and IMF parameters and geomagnetic activity indices and distinct variations in the superimposed epoch patterns. LFHE is regarded as high fluxes of electrons with energies < 50 keV and low fluxes for electrons with energies > 200 keV. FE10k is related to the highest fluxes of electrons at energies above 10 keV. Low energy electrons vary significantly with the geomagnetic conditions (e.g., Ganushkina et al., 2013; Sillanpää et al., 2017; Ganushkina et al., 2019). Therefore, there is no surprise that the occurrence of severe environment events classified as those two criteria exhibits more pronounced dependencies on the solar wind and IMF parameters and geomagnetic activity indices. At the same time, the similar dependencies are less obvious for the PG5k criterion based on spacecraft potential stressing again the absence of straightforward relations between the geomagnetic conditions and surface charging.

On the other hand, PG5k criterion is based on the duration of charging even though below extreme value (in contrast to other criteria which are based on peak values). It can be speculated that this specific feature could lead to the some kind of saturation seen in some figures (e.g. Figure 4.1a, b). If it is the case, the beginning of saturation corresponds to -5 kV charging. In addition, since almost all top 100 PG5k events occurred in eclipse and LANL spacecraft spend relatively little time in eclipse, the events with extreme geomagnetical activity can be represented poorly in the dataset. This could possibly make the dependence on activity less clear. It should be noted that absolute charging is different from differential charging. High absolute charging levels make charging risks higher but only if they are associated with high differential voltages. Too few spacecraft are equipped with sensors to allow assessing both at the same time. In the present study, we have looked at long duration charging events that could possibly lead also to high differential charging (PG5k) and on electron spectra that can produce both absolute and differential charging on the basis of particle-matter interactions.

In reality, there were many more events with severe environments detected by LANL satellites during 1990–2005 (Matéo-Vélez et al., 2018). One of the logical steps in continuation of the presented study would be an analysis using all data with a parameter above a given threshold. Such a threshold could be a potential below -100 V, or a flux of >10 kev electrons above 10^7 $\mathrm{cm}^{-2}\ \mathrm{sec}^{-1}\ \mathrm{sr}^{-1}\ \mathrm{keV}^{-1}$, etc. This analysis can verify the obtained conclusions.

Another useful study will be to perform similar as in the present study analysis by separating events outside and inside eclipse to get the events in PG5k criterion in eclipse and the events in PGXk criterion outside eclipse with X being a potential to be determined. For the Van Allen Probes data analysis, Matéo-Vélez et al. (2019) have used -100 V for potential X. Criteria based on satellite potential could distinguish events with a potential exceeding a given potential (as e.g.

-100 V). In addition, sorting out events inside and outside eclipse would help to separate better the effect of photoemission from ambient plasma and geomagnetic conditions.

Keeping in mind the points discussed above, the conclusions are the followings:

1. Moderate to intense substorm activity with the AE index ranging from about 500 to 1000 nT is present when severe environments are detected and time history of AE (AL) before and after events in all criteria exhibits a substorm-type pattern with max/min at the time of the event. The AE index determines the highest risk for severe environments for surface charging to happen, but this risk does not depend on the AE magnitude.

2. V_{SW} points directly to the highest risk dependent on the V_{SW} value to worst-case severe environments to happen. At the same time, no significant changes were seen in the time history of V_{SW} before and after the events in all four criteria, although V_{SW} values are elevated to 700 $\mathrm{km \cdot s^{-1}}$ for HFAE criterion.

3. Although no high risks for severe environments to occur related to the SYM-H index were found, a storm-type pattern of the superimposed epoch SYM-H for LFHE and FE10k low energy fluxes criteria was obtained, but the events were associated with main and recovery phases of small to moderate storms.

4. Worst-case severe environments for surface charging according to all four criteria occur when the *Kp* index shows moderate disturbance (3 to 5) but a high risk for them is not associated with the *Kp* index; changes in *Kp* index as increase in 6–9 hours exist only before events defined by LFHE and FE10k criteria which are based on high fluxes of low energy electrons.

5. IMF B_Z was found to be small and negative during the events in all criteria with superimposed epoch analysis revealing the southward turning pattern in IMF B_Z for LFHE and FE10k events with maximum drop of -6 nT one hour before the event occurring and smaller changes for PG5k and HFAE events. There is no clear dependence of risk to have a severe environment on IMF B_Z.

6. As expected, the risks and time history for VB_s are determined by the risks and time history for IMF B_Z and V_{SW}.

7. N_{SW} was <5 $\mathrm{cm^{-3}}$ for all criteria except for LFHE when it was 2 times higher. No high risk was found to be associated with the N_{SW} but there exists a dependence on the N_{SW} magnitude for LFHE and FE10k criteria. No changes were seen in the time history of N_{SW}.

The conducted analysis demonstrated that events detected following two criteria, LFHE and FE10k, based on the enhancements of low energy particle fluxes are evidently different from other two (PG5k and HFAE) with larger magnitudes of the parameters and distinct patterns in the time history of them. It is necessary to stress that flux criteria are more easily generalized to non-LANL spacecraft whilst PG5k is uniquely determined by spacecraft materials, designs, and geometries.

CHAPTER 5

Electron Flux Changes During Substorms

5.1 Introduction

The increase in flux of superthermal (E ~1–100 keV) electrons at geosynchronous orbit (GEO) during substorms has long been observed by GEO spacecraft (e.g., Parks & Winckler, 1968; Nagai, 1982; Birn et al., 1998; Nagai et al., 2019). These injections, or enhancements of electron flux at superthermal energies, are generally regarded as resulting from a dipolarization front that propagates Earthward following magnetic reconnection in the tail plasma sheet (e.g., Hoshino et al., 2001; Thomsen et al., 2001; Imada et al., 2007; Fu et al., 2013; Pan et al., 2014; Ergun et al., 2018).

The energization of electrons around the substorm dipolarization front in the near-Earth ($-7\mathrm{R_E} > X_{\mathrm{GSM}} > -30\mathrm{R_E}$) plasma sheet is due to both betatron and Fermi acceleration (Asano et al., 2010; Fu et al., 2011; Birn et al., 2013, 2014; Gabrielse et al., 2016; Malykhin et al., 2018). However, near-Earth plasma sheet electron flux increases during substorm dipolarizations are sometimes very strong or other times nonexistent (e.g., Runov et al., 2011). Moreover, sometimes there is a decrease in flux (e.g., Hwang et al., 2011). From investigating three case studies, Runov et al. (2013) proposed that the spacecraft observing location relative to the center of the dipolarization front could be responsible for whether an increase, decrease, or no change in flux was measured. The Runov et al. (2013) study found an increase in superthermal electron flux near the center of a dipolarization front but decreased flux on the dusk side of the front. A statistical study considering not three, but more than 400 dipolarizations, showed a much higher likelihood for superthermal electron flux increase (2–3 times more likely for increase versus decrease) regardless of location relative to the center of a dipolarization front (Y. Wang et al., 2015). Note that the Y. Wang et al. (2015) study did not differentiate between substorm and non-substorm dipolarization fronts.

To date, for substorm dipolarizations only, there has not been a statistical study examining the magnitudes of electron flux increases (or decreases) in the plasma sheet, nor a statistical study between the magnitude of electron flux related to the strength of a substorm dipolarization. The

strength of a substorm dipolarization is tied to the strength of the substorm current wedge (e.g., Hesse & Birn, 1991). The substorm current wedge connects to the auroral electrojet current (e.g., Baumjohann, 2002; Kepko et al., 2014). Since the SME index primarily responds to the auroral electrojet current, it can be considered as a proxy for the strength of a substorm dipolarization.

In this chapter, we better characterize the energization of superthermal plasma sheet electrons during substorms. We consider both the radial distance and local time of plasma sheet observations, as well as the azimuthal distance from the location of peak auroral electrojet current. In Section 5.2, we describe our approach to this investigation. We present our findings in Section 5.3. The significance of our results are discussed in Section 5.4, and we provide a summary in Section 5.5.

5.2 Methodology

We selected 45 substorms during the 2008 and 2009 THEMIS tail seasons when the THEMIS probes were in near-conjunction in the plasma sheet, aligned near local midnight. Substorm onset times were identified using the SuperMAG isolated substorm listing developed by Ohtani and Gjerloev (2020). For this study, we use electron flux data (described below) at twenty energies between 1.3–65.6 keV. In this Chapter, we highlight results from only three of these energies—2 keV, 12 keV, and 52 keV. These energies correspond to the thermal population (2 keV), the near-superthermal population (12 keV), and the superthermal population (52 keV) of electrons in the near-Earth plasma sheet; and, they are representative as important contributors to inner magnetosphere dynamics (e.g., Ganushkina et al., 2014).

5.2.1 Data

Electron flux data are from the THEMIS Electrostatic Analyzer (ESA) (McFadden et al., 2008) and Solid State Telescope (SST) (Angelopoulos et al., 2008) instruments and their combined data distribution called GMOM (ground moments). We used the pterf (ESA full, SST reduced) data product from the GMOM data set and down-sampled to one-minute time resolution by taking the average over each minute. We used the plasma moments of temperature and density and the magnetic field data from the Flux Gate Magnetometer (Auster et al., 2008) to calculate the local plasma β. As shown in Equation 5.1, we assume the plasma is isotropic and quasi-neutral in calculating plasma β, where we have used the permeability of free space, μ_0, Boltzmann's constant, k_B, and the local magnetic field strength, B. The ion and electron isotropic temperatures are T_i and T_e, respectively and the plasma number density is N.

$$\beta = \frac{P_k}{P_B} = \frac{2\mu_0 k_B N(T_i + T_e)}{B^2} \tag{5.1}$$

We used the SME index from the SuperMAG magnetometer network (Gjerloev, 2012) to determine the strength of each substorm. For each of 45 identified substorms, we represented the strength of the substorm by taking the maximum SME value between 0 to $+3$ hours of substorm onset itme. The maxima of the SME index for the 45 substorms ranged from 204 nT to 1263 nT, with a median value of 432 nT. Within the SuperMAG dataset are the locations of the individual magnetometer stations that were used in the determination of the SME index at each time step. We used the MLT of the ground magnetometer station that was used during the same time step as the peak SME value as an approximate azimuthal location of where the substorm current wedge was strongest.

5.2.2 Calculating Flux Changes

We quantified the change in electron flux for energies between 1.3–65.5 keV by considering the pre- and post-onset flux levels. In Figures 5.1 and 5.2, we show two examples of survey plots that we generated for the THEMIS observations of plasma sheet electron flux during substorms. The top panel shows the time series of one-minute-averaged electron flux in twenty energy channels from 1.3–65.5keV. The bottom panel shows the corresponding time series of the SMU and SML indices (blue and red curves, respectively), as well as the calculated plasma β (green curve). In both panels, the time series data are -2 to $+3$ hours relative to the substorm onset time—indicated by a black dash-dot vertical line—of the Ohtani and Gjerloev (2020) isolated substorm onset list.

For each THEMIS probe and for each substorm, we generated survey plots of the form of Figures 5.1 and 5.2. If there were no missing data and plasma β remained greater than unity both before and subsequent to substorm onset, we considered it a valid observation; otherwise, invalid. The $\beta > 1$ requirement makes it more likely that the spacecraft was observing plasma sheet electrons, and not in the magnetotail lobes (Baumjohann et al., 1989; Ruan et al., 2005). Note that due to plasma sheet thinning during substorms (e.g., E. W. Hones, 1980; Hill & Reiff, 1980; E. W. Hones et al., 1984; Baumjohann et al., 1992; Petrukovich et al., 2007; Artemyev et al., 2016), the spacecraft may have temporarily been in the magnetotail lobe; however, if after plasma sheet expansion, the spacecraft was once again in the plasma sheet, we still considered this a valid observation. In total we identified 101 valid observations from a potential list of 260.

For the valid observations, we manually chose a time, $t_{\rm bef}$, before substorm onset when $\beta > 1$. Typically, $t_{\rm bef}$ was chosen to be approximately 30 minutes prior to onset, however it varied subjectively based on when the best time represented the pre-onset plasma sheet. We then chose a time, $t_{\rm aft}$, after substorm onset when the spacecraft had returned (the probe did not leave in all

events) to the plasma $\beta > 1$ state (as in the two examples in Figures 5.1 and 5.2). Typically, the $t_{\rm aft}$ times were chosen (again subjectively) as the time when the electron flux in a majority of energy channels had reached a local maximum. The $t_{\rm bef}$ and $t_{\rm aft}$ times chosen for our two examples are labeled with vertical dotted lines in Figures 5.1 and 5.2. For the 101 observations, and for each of the twenty energy channels, we calculated ΔJ, the change in flux from before to after substorm onset. We define, for each energy channel, ΔJ as $\log_{10}(J_{\rm aft}) - \log_{10}(J_{\rm bef})$, where $J_{\rm aft}$ and $J_{\rm bef}$ are the flux at $t_{\rm aft}$ and $t_{\rm bef}$, respectively.

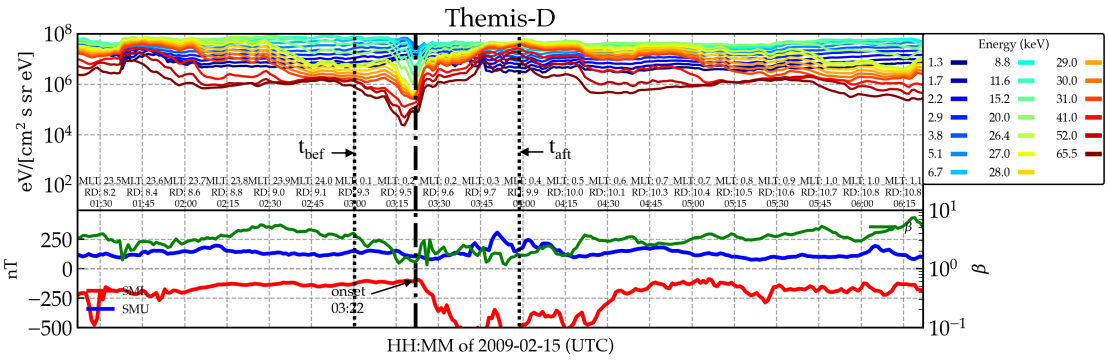

Figure 5.1: Example of electron flux increase in the plasma sheet after a substorm onset, relative to the pre-onset flux. Top panel: time series of electron flux at 20 different energy channels. Observation time and spacecraft location are labeled at bottom of top panel. Bottom panel: corresponding SML and SMU indices (scale on left vertical axis) and local plasma β (scale on right vertical axis). Times chosen for $t_{\rm bef}$ and $t_{\rm aft}$ are labeled with vertical dotted lines. Substorm onset time labeled with vertical dash-dot line.

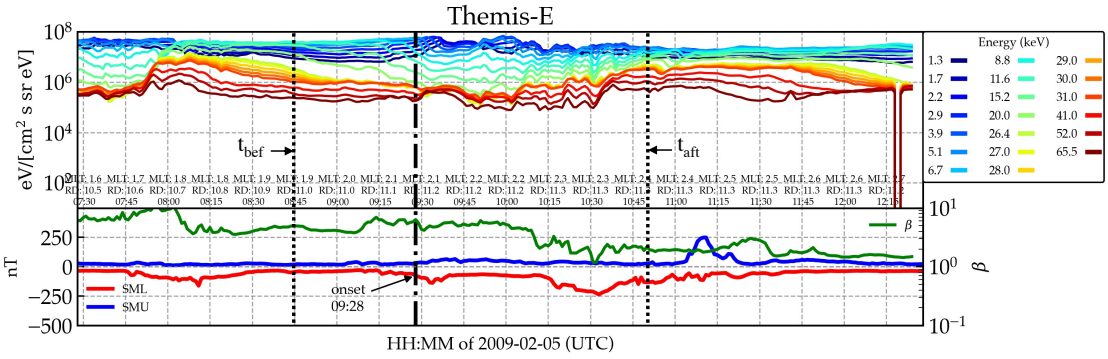

Figure 5.2: Example of electron flux that does not increase in the plasma sheet during a substorm event. Format same as Figure 5.1.

5.3 Results

We organized the magnitude of the change in flux, ΔJ, by the observing location and substorm strength. We ascertained whether there any relationships existed between substorm related electron flux enhancements and location of spacecraft or strength of the substorm. As described in Section 5.2.1, we quantified the substorm strength by using the maximum SME value, $\mathrm{SME_{max}}$, within two hours post substorm onset. The location parameters include the MLT (relative to midnight) and radial distance, $\mathrm{R_{dist}}$, of the observing spacecraft. $\mathrm{R_{dist}}$ is defined as the distance in the GSM xy-plane from the center of the Earth ($\mathrm{R_{dist}} = \sqrt{X_{\mathrm{GSM}}^2 + Y_{\mathrm{GSM}}^2}$). We also use the magnetic local time distance, ΔMLT, which is the distance (in hours of local time) between the observing spacecraft and the SuperMAG ground station that observed $\mathrm{SME_{max}}$.

Shown in Figures 5.3–5.5 are pair-pair plots of the various parameters considered as potentially contributing to ΔJ. Each of the Figures 5.3–5.5 has the same format. The 5x5 grid of panels are symmetric about the upper left to lower right diagonal. The diagonal itself shows frequency histograms of each of the five parameters. We show the histograms to illustrate the frequency distribution of each parameter. The absolute heights of the bars are not relevant; only the bar heights relative to their neighbors are needed to see the frequency distributions. The values of the parameters that each bar represents are labeled at the bottom of the respective columns. The top row (and left-most column), which are labeled as "2keV", "12keV", and "52keV" depending on the figure, shows ΔJ as a function of $\mathrm{SME_{max}}$, MLT, $\mathrm{R_{dist}}$, and ΔMLT. The lower-right 4x4 grid of panels shows the pairwise scatter of the same four parameters. The color of points in the 4x4 grid represents the ΔJ values.

Figure 5.3 shows all of the 2 keV electron flux changes and their relationships to the other parameters via the various scatterplots. The upper left panel shows the frequency histogram of ΔJ for the 2 keV energy channel and we see that the vast majority of observed flux changes are negative. In contrast, the upper left panel of Figure 5.4 shows that the vast majority of observed 12 keV electron flux changes are positive. Furthermore, the 52 keV electron flux changes are distributed even more strongly positive (Figure 5.5).

In general, it is difficult to notice any trends of ΔJ in the panels of Figures 5.3, 5.4, and 5.5. It seems that there is a correlation between MLT (relative to midnight) and ΔMLT. However, no noticeable relationships exist between MLT, ΔMLT, and ΔJ, which is what we are interested in. Most of the observations occurred between 10–12 $\mathrm{R_E}$ since this was the apogee range for three of the five THEMIS probes; and, this is noticeable in the 'rdist' histogram and the 'rdist' x 'mlt' panels. Despite the lack of appearance of any correlations between ΔJ and the parameters of $\mathrm{SME_{max}}$, MLT, $\mathrm{R_{dist}}$, and ΔMLT, in Section 5.3.1 we attempt to quantify any relationships that may exist.

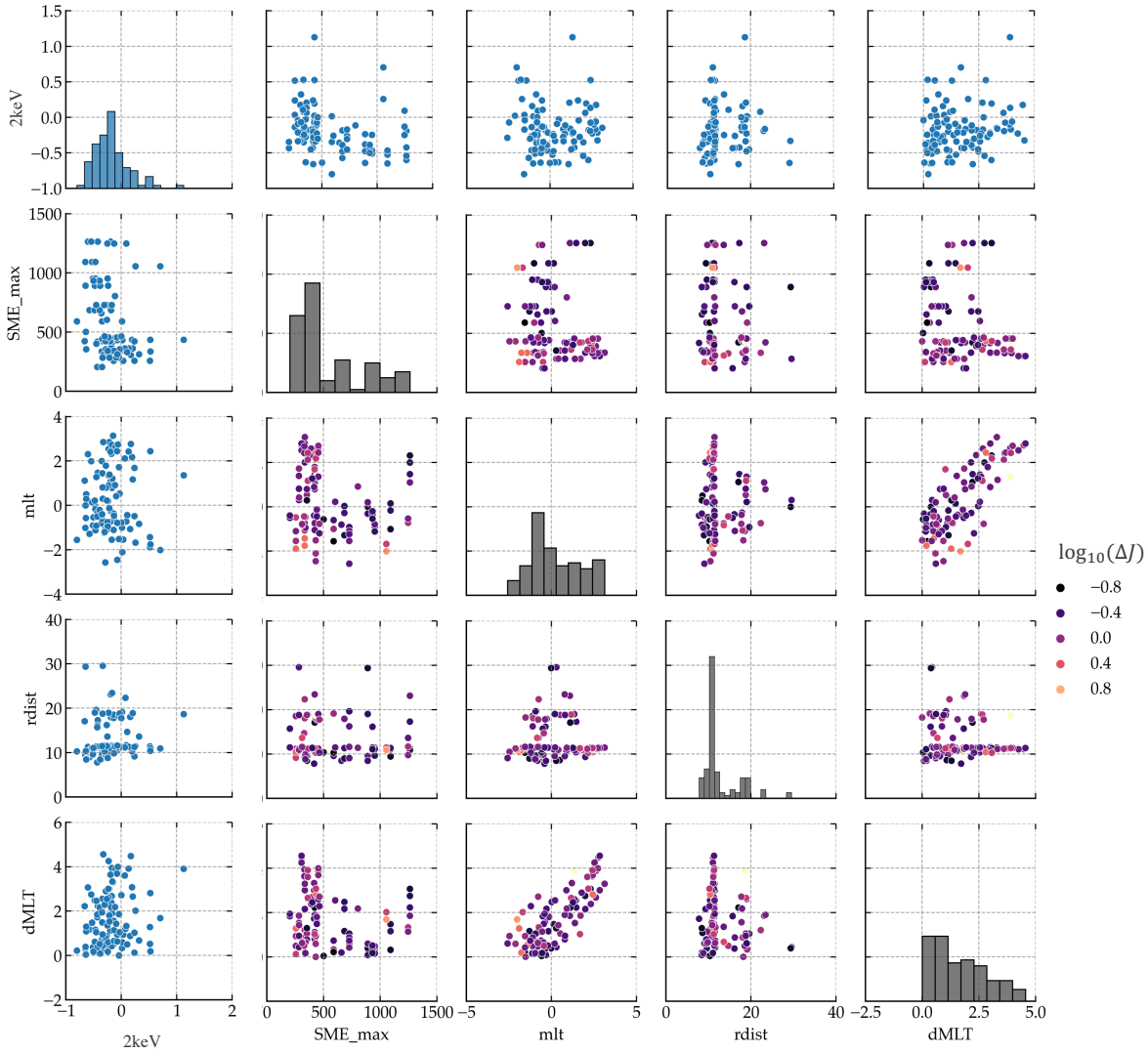

Figure 5.3: Pairwise plot of parameters potentially influencing the magnitude of 2 keV electron flux changes in the plasma sheet during substorm. The upper left to lower right diagonal shows the frequency histogram of each parameter. Shown off-diagonal are the scatter of each parameter with the others. The left-most column and top row show the change in flux dependent on each parameter. The panels with multi-colored dots show the change in flux as a function of two different parameters. The color represents the magnitude of the change in flux (in $\log_{10}$ values—so, zero means no change in 2 keV flux).

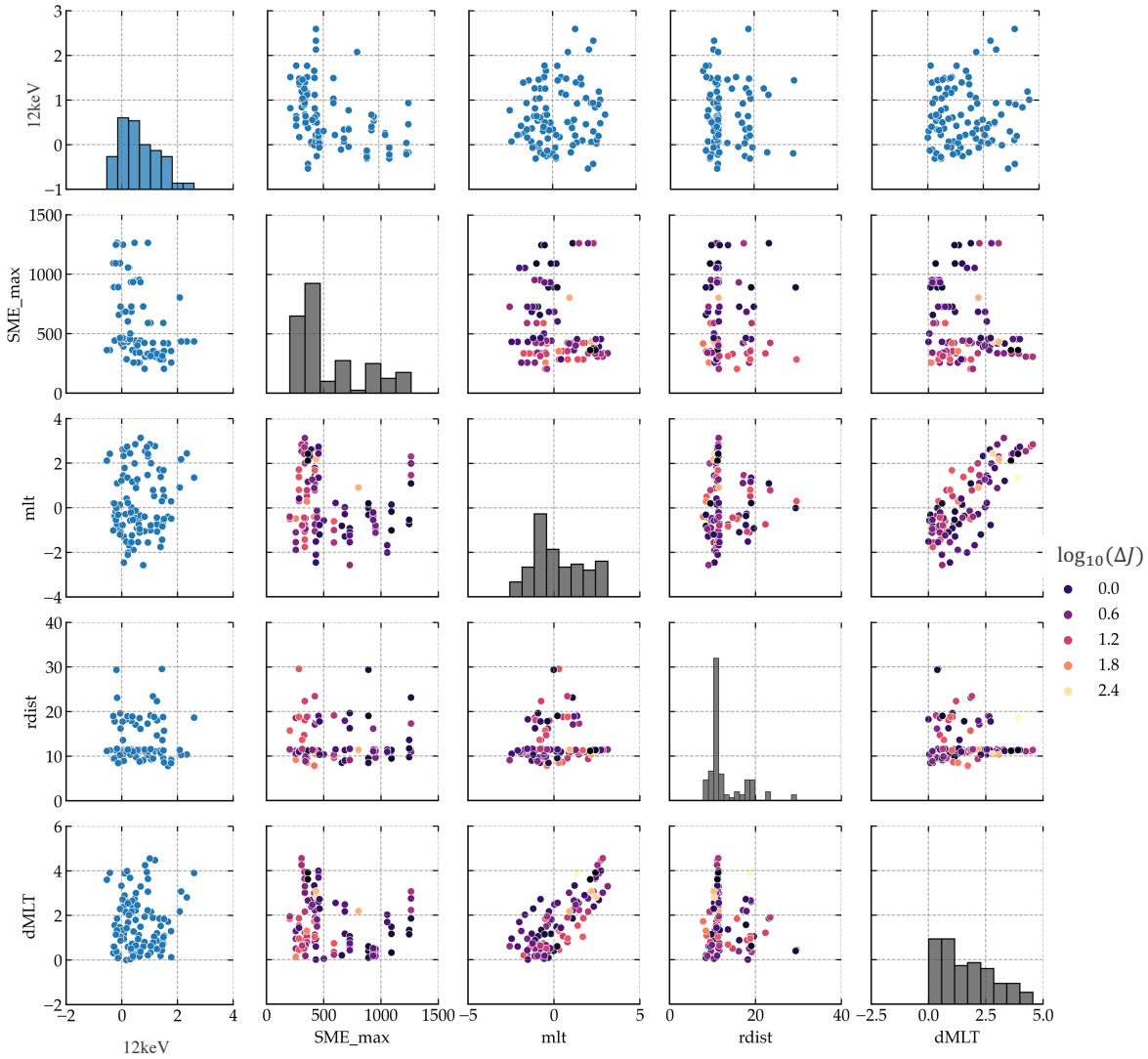

Figure 5.4: Same format as Figure 5.3 except now showing for 12 keV.

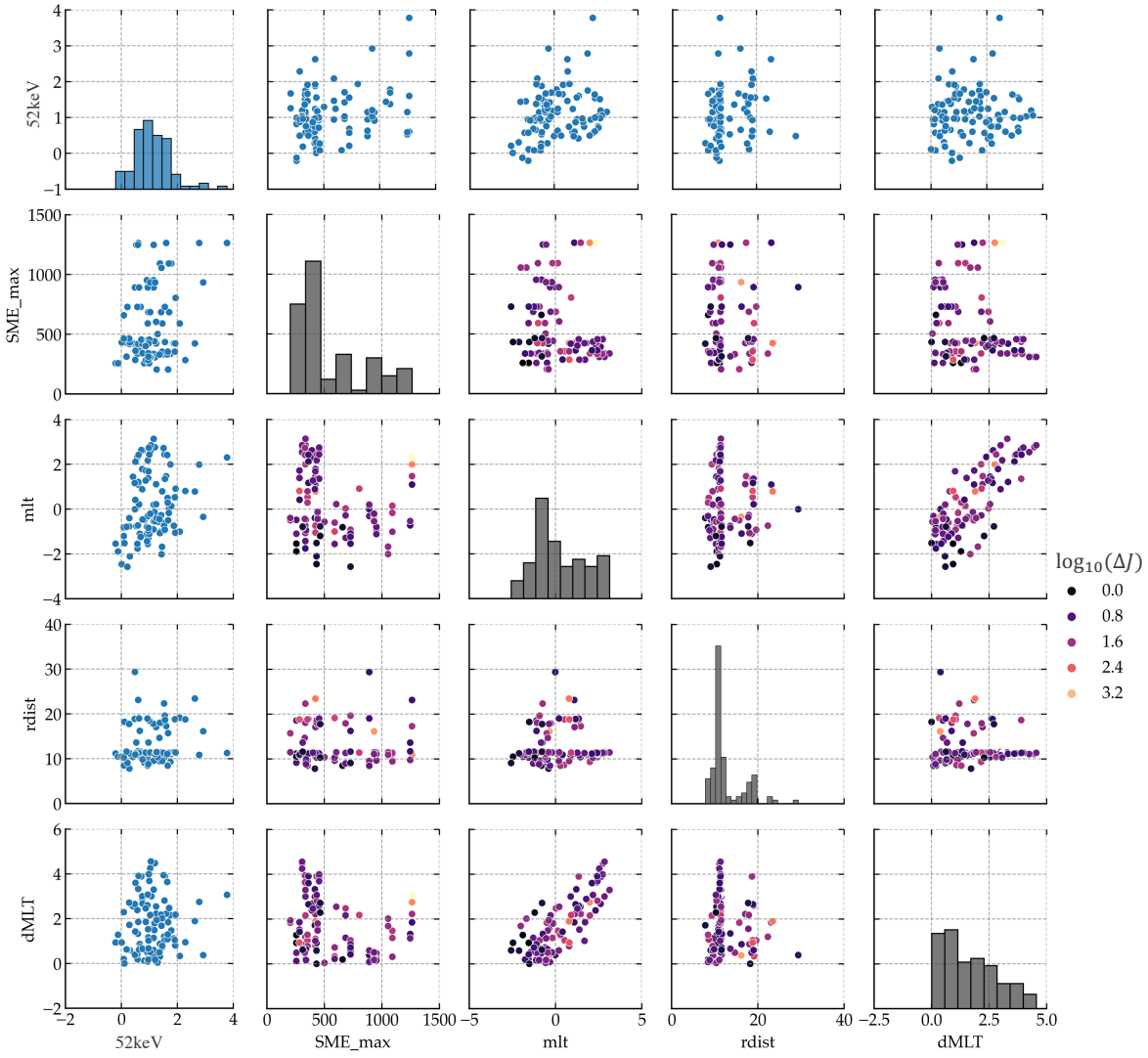

Figure 5.5: Same format as Figure 5.3 except now showing for 52 keV.

5.3.1 Bootstrap analysis

We wish to further investigate whether there are any trends between ΔJ and location or substorm strength. In Figures 5.7–5.10, we show the results of applying linear correlation fitting with bootstrap analysis. In each panel, the dashed line represents the linear regression between the ΔJ and one of the other parameters. Estimates of the parameters of the linear regression line, $\hat{\omega}_0$ and $\hat{\omega}_1$ in Equation 5.2 are found using the least squares (LS) method, shown in Equation 5.3 To estimate the uncertainty in $\hat{\omega}_0$ and $\hat{\omega}_1$, we performed a bootstrap analysis by taking 500 random samples with replacement of the original data. For each random sample, we calculated a linear regression, represented by the pink lines, using LS. We estimated the uncertainty of $\hat{\omega}_0$ and $\hat{\omega}_1$ as the standard deviation of the bootstrapped values, σ_{ω_0} and σ_{ω_1}. The equations for the linear regression of the original data and the uncertainty from the bootstrapped data are shown in the orange boxes as $y = (\hat{\omega}_1 \pm \sigma_{\omega_1})x + \hat{\omega}_0 \pm \sigma_{\omega_0}$.

$$y = \hat{\omega}_1 x + \hat{\omega}_0 \tag{5.2}$$

$$\hat{\omega}_1 = \frac{\sum_{i=1}^{n}(x_i - \bar{x})(y_i - \bar{y})}{\sum_{i=1}^{n}(x_i - \bar{x})^2} \tag{5.3}$$

$$\hat{\omega}_0 = \bar{y} - \hat{\omega}_1 \bar{x} \tag{5.4}$$

In Equation 5.3, x represents one of the four parameters—R_{dist}, SME_{max}, MLT, or ΔMLT—that is used as a potential predictor for ΔJ, which is represented by y. The variables $\bar{x}$ and $\bar{y}$ are the mean values of the x and y samples of size n, respectively.

The "R" value listed at the top of each panel in Figures 5.7–5.10 is the Pearson correlation coefficient for the original data (scatter of all points in each panel), and is calculated using the formula in Table A.1. The p-value listed at the top of each panel is from an hypothesis test where the null hypotheses, H_0, is that the linear regression slope, $\hat{\omega}_1$, is zero. The alternative hypothesis, H_1, is that $\hat{\omega}_1$ differs from zero (see Equation 5.5).

$$\begin{cases} H_0: & \hat{\omega}_1 = 0 \\ H_1: & \hat{\omega}_1 \neq 0. \end{cases} \tag{5.5}$$

In Figure 5.7, we use data from all 101 observations. The left column shows the correlations between 2 keV electron flux changes and the four different parameters of R_{dist}, SME_{max}, MLT, and ΔMLT. The middle and right columns are the same, except for 12 keV and 52 keV energies, respectively. The p-values for nearly all panels show that it is not appropriate to reject the null

hypothesis, H_0. That is, there is not enough evidence to say that $\hat{\omega}_1$ differs from zero. We also visually see this in the spread of the bootstrapped, pink lines surrounding the main, dashed line. The only exception to this is for the 12 keV flux change correlation with SME_{max}. The p-value for this panel is less than 10^{-3}, suggesting that our null hypothesis is not correct and implying that there is some correlation. Even though we have evidence of statistical significance, the R-value is only 0.40, which conveys weak correlation at best. For meaningful correlation, we would expect an R-value $>$0.5 and for strong correlation we would expect R$>$0.7.

In order to further deduce whether there are dependencies of ΔJ on radial distance, we subset the data into three distance ranges. Figure 5.8 shows the data for observations at radial distance $R_{dist} < 11$ R_E, with number of points equal to 32. Figure 5.9 shows the data for observations at radial distance $11 < R_{dist} < 12$ R_E, with number of points equal to 42. Figure 5.10 shows the data for observations at radial distance $R_{dist} > 12$ R_E, with number of points equal to 27. Similar to the subplots of Figure 5.7, the p-values for nearly all panels in Figure 5.8 are high enough to not reject H_0. The p-values for the hypothesis tests at 12 keV suggests that the correlation there is statistically significant; and, this correlation is negative, indicating that more intense substorms lead to smaller fluxes at 12 keV. This is also true for the $R_{dist} > 12$ R_E subset (in Figure 5.10). However, in the 11 $R_E < R_{dist} < 12$ R_E distance range subset (Figure 5.9), it is only the 52 keV flux changes that show statistically significant correlation with SME_{max}. Contrasting the 12 keV energy, the 52 keV correlation with SME_{max} is positive. Yet, only one R-value in all of these plots is above 0.5—none are above 0.7.

5.3.2 Heatmaps

We finally organize the change in plasma sheet electron flux during substorm by showing ΔJ of all available energy channels between 1–65 keV. In Figure 5.6, we show ΔJ for all observed substorms as a function of the R_{dist} value. Recall that we count each THEMIS probe as its own observation—most substorms had multiple observations. Each row of Figure 5.6 is an individual energy channel, and each column is an observation by a THEMIS probe. The columns are labeled with the R_{dist} value for that observation. The rows and columns of Figure 5.6 are ordered monotonically, but neither the rows nor the columns have equal spacing in values. The change in plasma sheet electron flux due to the substorm is indicated by color. Each of the eight colors in the top color scale represents one-half decade of magnitude, from -1 to $+3$ ΔJ. If it was the case that the change in flux depended on radial distance, then one would expect to see a peak in color at a particular radial distance. Instead, the pattern of ΔJ from low radial distance to high radial distance appears randomly organized for all energies. Notwithstanding, from low energy to high energy (from bottom to top of the heatmap) we do see a pattern where there is generally a decrease

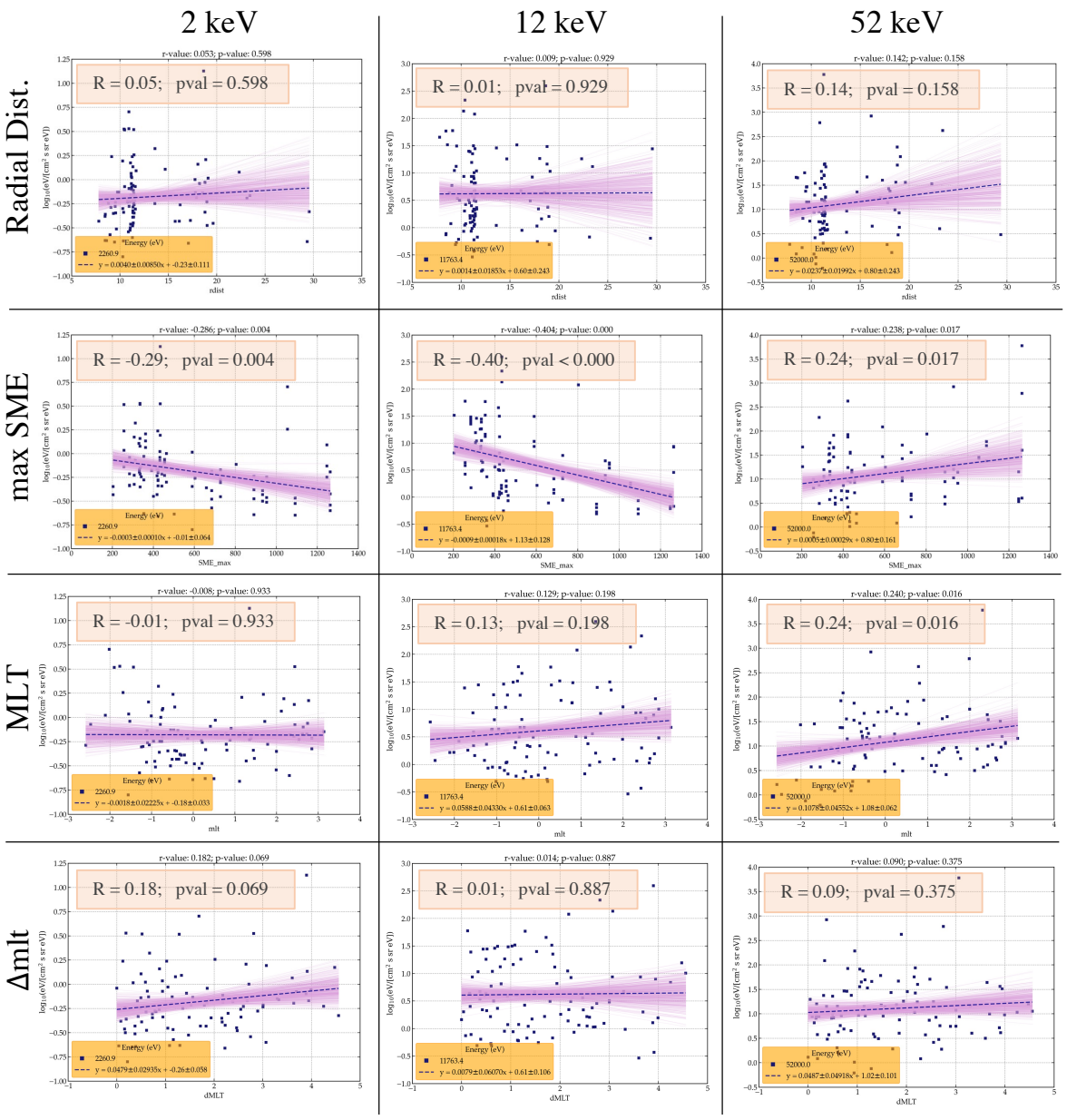

Figure 5.7: Scatter plots with linear regression lines for three energies and four different parameters. Linear regression using all data are shown as dashed lines. The multiple magenta lines represent linear regressions calculated after each of 500 bootstrap iterations. The uncertainties on the linear equation lines are the standard deviation of the 500 bootstrap samples.

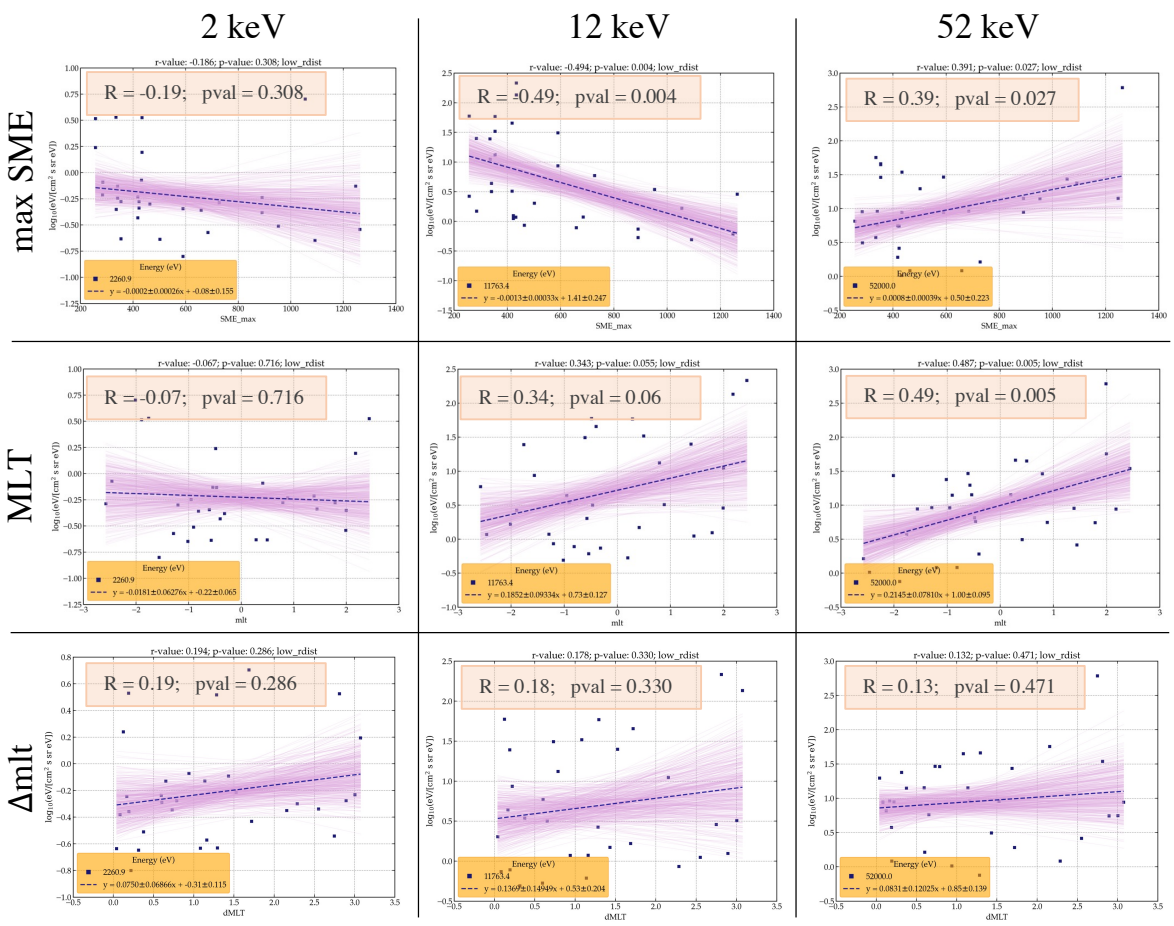

Figure 5.8: Same format as Figure 5.7 except using data subset for 8 R_E < r < 11 R_E.

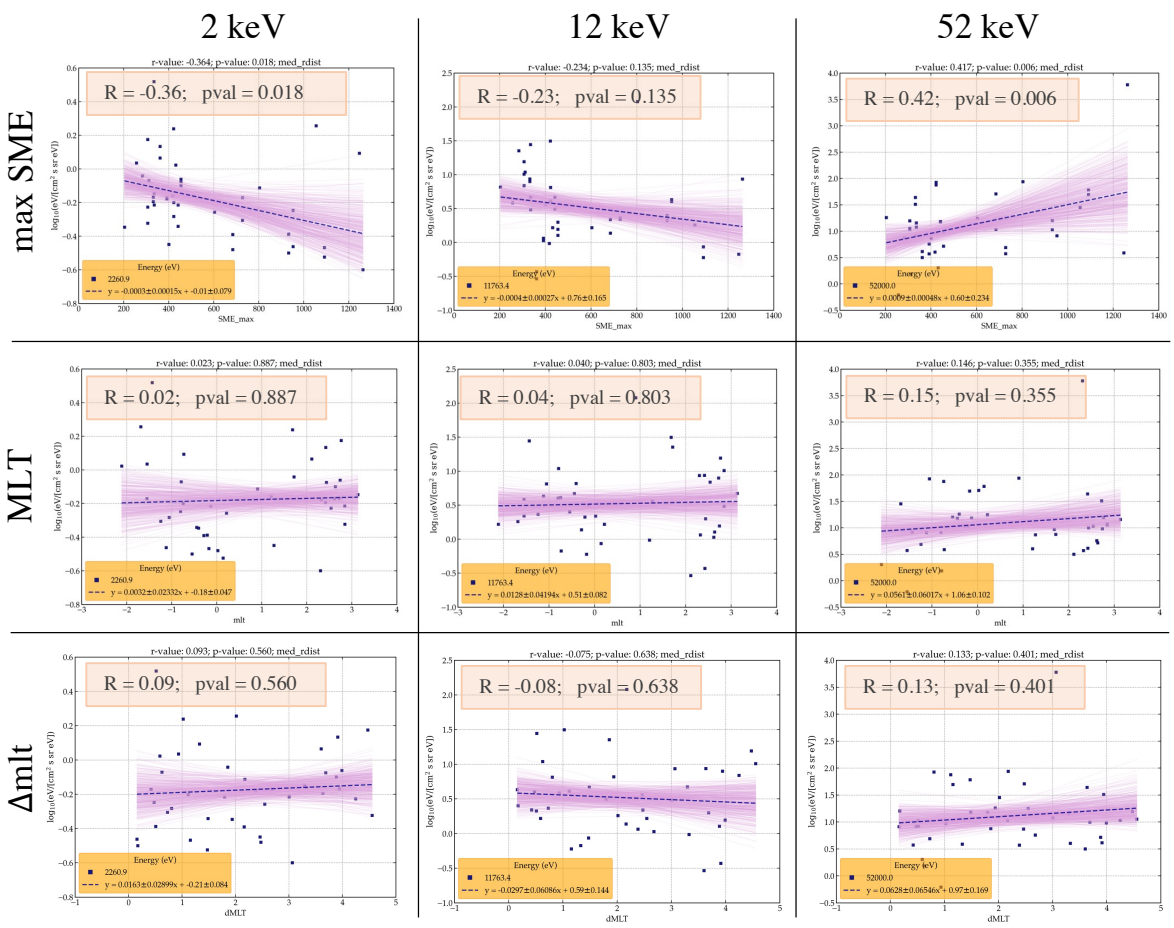

Figure 5.9: Same format as Figure 5.7 except using data subset for 11 R_E < r < 12 R_E.

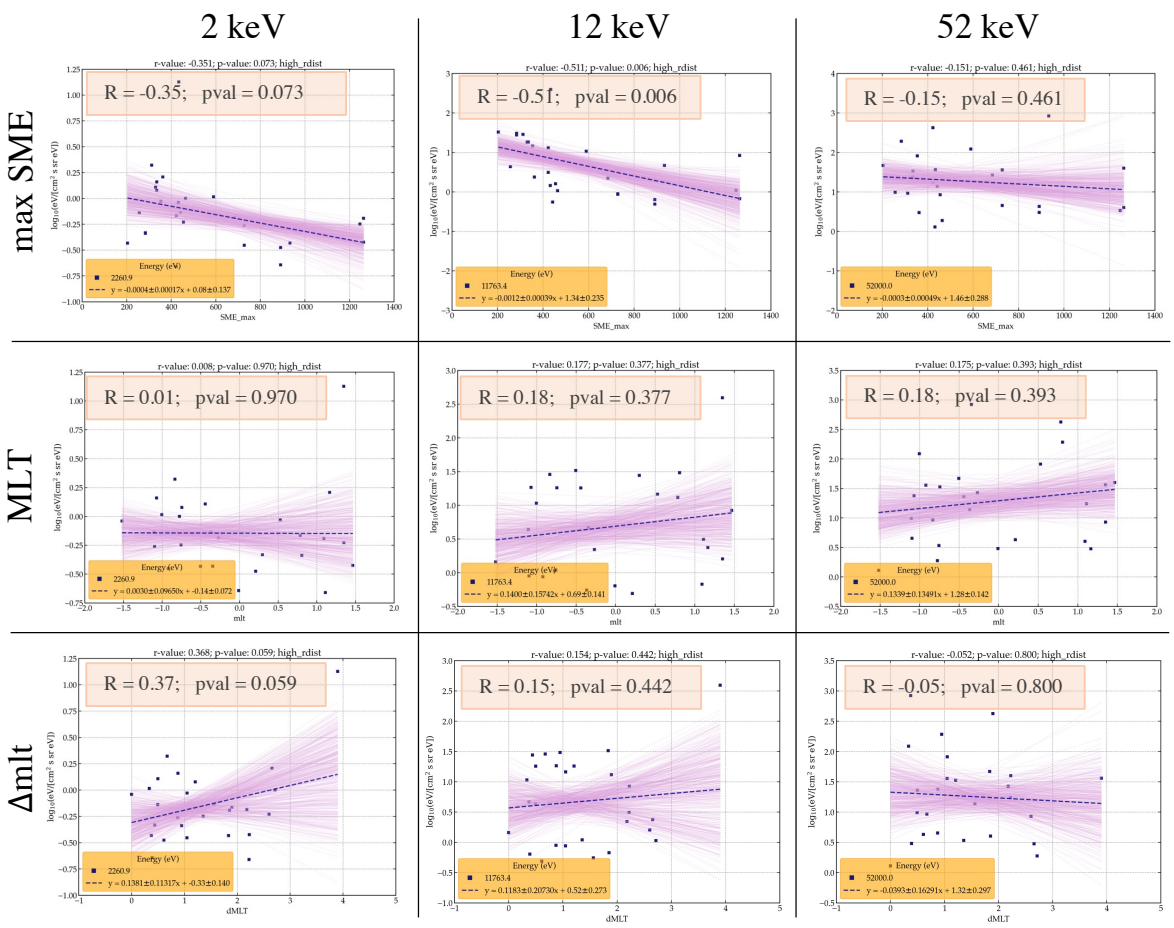

Figure 5.10: Same format as Figure 5.7 except using data subset for 12 R_E < r < 30 R_E.

in flux at 1–5 keV. We see increases in flux only at higher energies.

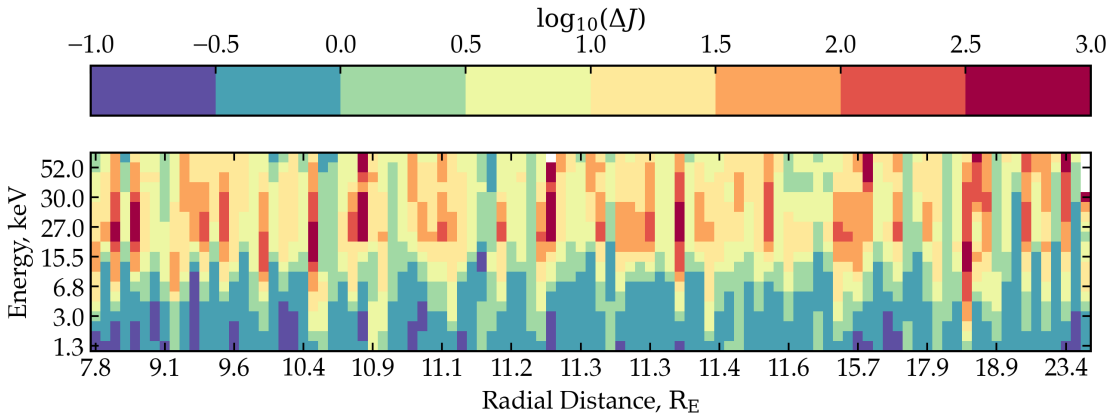

Figure 5.6: Electron flux changes as a function of radial distance for energies between 1–65 keV.

In Figure 5.11, we show ΔJ as a function of SME_{max}, subset by R_{dist}, and the format of each of the three panels is the same as in Figure 5.6. The top panel of Figure 5.11 includes only observations $<$11 R_E; the middle panel includes only observations that were between 11–12 R_E; and, the bottom panel includes only observations when the spacecraft were located at $>$12 R_E. Since there were multiple spacecraft observing the same substorm, some columns have the same SME_{max} value. Like the heatmap of Figure 5.6, the rows and columns of the three panels in Figure 5.11 are ordered monotonically, with unequal spacing of successive values. The change in flux across SME_{max} values does not show a consistent pattern, but rather appears as randomly organized. However, consistent with the heatmap of Figure 5.6, the heatmaps of Figure 5.11 show a general decrease in flux for energies 1–5 keV (and general increase in flux for higher energies), and these general trends are present regardless of SME_{max} value or radial distance.

5.4 Discussion

The analysis of Section 5.3 and Figures 5.3–5.11 shed further insight into the dependence of superthermal electron flux changes in the plasma sheet and their dependence on substorm strength and location. Despite using a limited amount of data—101 valid observations—we begin to statistically show that very few dependencies and patterns can be inferred. There is a slight dependence of ΔJ on substorm strength, as determined by the max value of the SME index post substorm onset. However, this dependence only seems to exist for energies $\gtrsim$12 keV and is more complicated when sub-setting for different radial distances. Since the SME index is primarily a measure of the auroral electrojet current (Nosé et al., 2012), and this current is connected to the plasma sheet

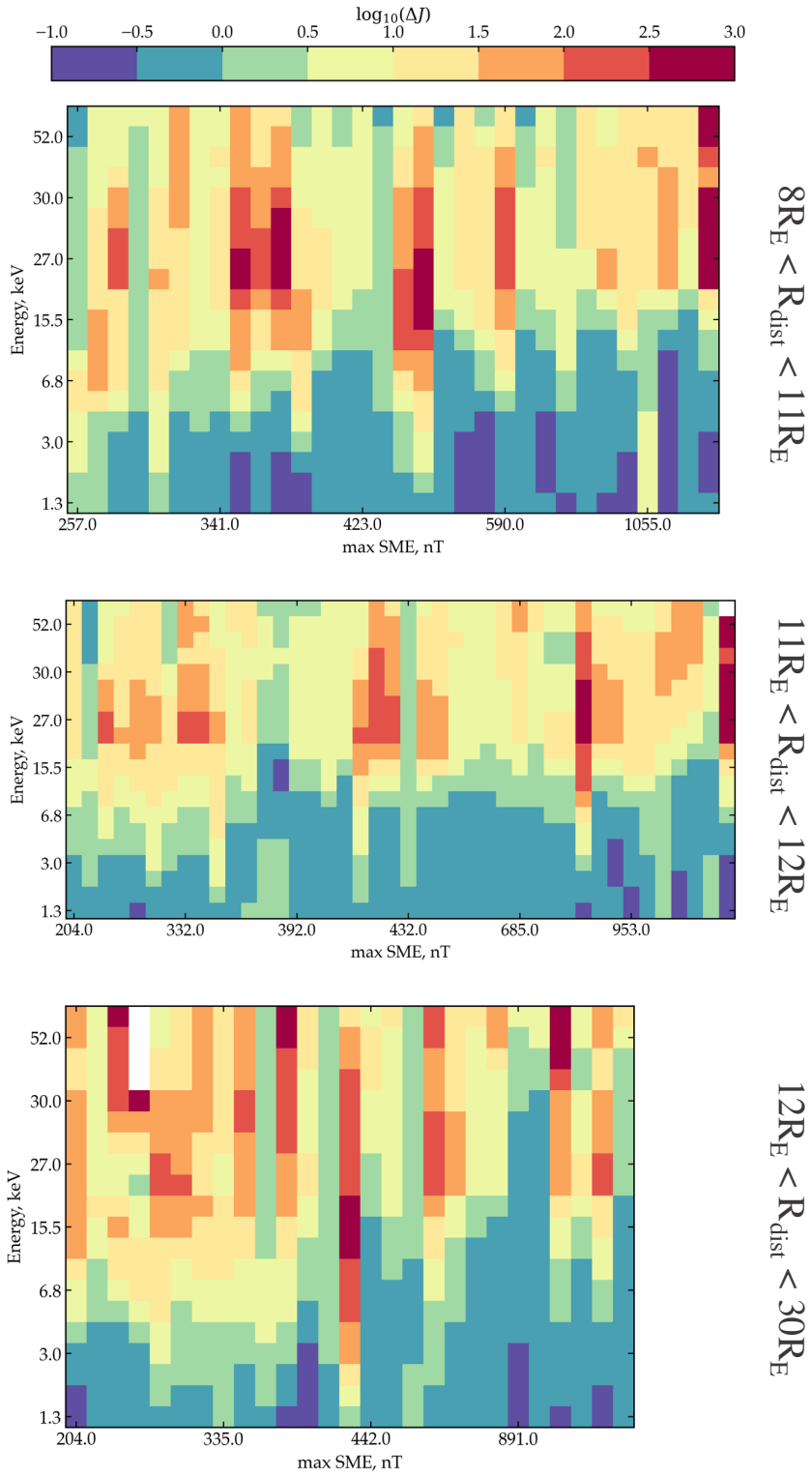

Figure 5.11: Electron flux changes as a function of SME_{max} for energies 1–65 keV for all observations. The top panel is observations with low radial distance, the middle panel has medium radial distance observations, and the bottom panel has large radial distance observations.

through the substorm current wedge and field-aligned currents (Baumjohann, 2002; Kepko et al., 2014), we would expect that larger SME values are indicative of higher plasma sheet magnetic field changes, ultimately leading to higher electron energization through betatron and Fermi acceleration (Asano et al., 2010; Birn et al., 2013). In our analysis, we see that for electron energy at $\sim$ 12 keV, the ΔJ is negatively correlated with the SME_{max} value. Only for superthermal plasma sheet energies, $\sim$ 50 keV, is there a positive correlation between ΔJ and SME_{max}. The transition from negative correlation to positive correlation occurs between 20–30 keV. The exact energy is indiscernible—the energies between 20–30 keV have zero slope when correlated with SME_{max}. We stress that the correlations between ΔJ and SME_{max} that we found are weak, and with a more robust study (i.e. including many more observations than our study) they may be found to be nonexistent.

Overall, we fail to find any discernible correlations between electron flux increases during substorms with the strength of substorm or location relative to substorm onset. Our study failed to find any correlations or dependencies between ΔJ and the sampling location at the time of substorm onset. The scatter between ΔJ and R_{dist}, MLT, or ΔMLT in Figures 5.3–5.5 do not show a clear pattern of ΔJ being dependent on any of these location parameters. Moreover, the bootstrap analyses shown in Figures 5.7–5.10 indicate that there is not enough statistical evidence to overrule the hypothesis that a linear regression slope is anything other than zero. This implies that the correlation in the subplots of Figures 5.7–5.10 is not statistically significant. Therefore, based on the results of this study, the change in flux of thermal to superthermal electrons in the near-Earth plasma sheet does not appear to depend on the location within the plasma sheet, nor on the azimuthal distance from the ground station of SME_{max}.

In order to substantiate the above findings, there are at least three steps that could be taken in future research directions. Firstly, data from more than two years of THEMIS tail seasons could be added to substantially increase the number of valid observations of plasma sheet electron flux changes during substorms. Even within the 2008 and 2009 tail seasons (used in this study), there are many more times when there were substorms and multiple THEMIS probes in the tail. What was limiting to increase the number of valid observations in this study, and what would be limiting by expanding beyond year 2009, is the necessity to automate some of the methodology used. In this study, we visually inspected 260 survey plots looking for valid observations and manually selected the pre- and post-onset times. In subsequent studies, one would need to develop an algorithm to perform these steps, which would both reduce the amount of time and reduce the amount of subjectivity and bias in the selection process. If much more data and valid observations were obtained in this way, then future analyses could potentially be performed using more advanced statistical techniques, such as k-means clustering, or employing decision trees in understanding the hierarchy of dependencies.

Secondly, the analysis and methodology used in this study could be extended to include radial distances as close as geosynchronous orbit using GEO satellites, such as the GOES series. What we have not accomplished in this study is following the evolution of the electron flux as it transports from greater to lesser radial distances during substorms. Adding data from GEO would allow for a more complete picture of the dependence of electron flux changes during substorms on substorm strength at different radial distances. In order to make a fair comparison between THEMIS data and GEO satellite data, however, one would need to know how THEMIS ESA and SST instruments are calibrated compared to the instruments on the other spacecraft. Therefore, this direction of research might first necessitate an inter-calibration study between the instruments of the multiple missions.

Thirdly, the location parameters that we used might not be the most appropriate for determining the spacecraft position relative to the substorm development. For example, the magnetic field in the near-Earth plasma sheet changes abruptly throughout the substorm process, and R_{dist} does not take this into account. A more useful parameter than R_{dist} would be the Z_{GSM} direction of the local magnetic field. This would provide a more physical indication of where the spacecraft is relative to the inner magnetosphere and relative to the substorm onset location.

5.5 Conclusion

We have analyzed 101 observations of the change in electron flux in the near-Earth plasma sheet during isolated substorms. We define the change in flux, ΔJ, as the $\log_{10}$ post-onset flux minus the $\log_{10}$ pre-onset flux. We looked for patterns of correlation between ΔJ and substorm strength as well as between ΔJ and several location parameters. We used the maximum SME index value, SME_{max}, post substorm onset to indicate the substorm strength. Our location parameters were the radial distance, R_{dist}, and the magnetic local time, MLT, of the observing spacecraft. We also used ΔMLT, defined as the azimuthal distance (in hours) between the observation and the SME ground station that observed SME_{max}. The summary of our results are as follows:

1. We found evidence of a weak correlation between substorm strength and the change in flux of near-superthermal to superthermal ($\gtrsim$12 keV) plasma sheet electrons.

2. The correlation between ΔJ of near-superthermal ($\sim$12 keV) electrons to substorm strength is negative. However, the correlation between ΔJ of superthermal ($\sim$52 keV) electrons is positive.

3. For changes of thermal electrons (1–10 keV), we find there is no correlation, nor dependence on the substorm strength. Most of the flux changes are negative for this energy range.

4. We did not find any correlations or patterns between ΔJ and observation location parameters of MLT, ΔMLT, and R_{dist}.